ENGINEERING GENETICALLY ENCODED FLUORESCENT BIOSENSORS TO STUDY THE ROLE OF MITOCHONDRIAL DYSFUNCTION AND INFLAMMATION IN PARKINSON'S DISEASE

by

Stevie Norcross

A Dissertation

Submitted to the Faculty of Purdue University

In Partial Fulfillment of the Requirements for the degree of

Doctor of Philosophy

Department of Chemistry

West Lafayette, Indiana

May 2019

THE PURDUE UNIVERSITY GRADUATE SCHOOL
STATEMENT OF COMMITTEE APPROVAL

Dr. Mathew Tantama
Department of Chemistry
Dr. Mary Wirth
Department of Chemistry
Dr. Angeline Lyon
Department of Chemistry
Dr. Chittaranjan Das
Department of Chemistry

Approved by:

Dr. Christine Hrycyna
Head of the Graduate Program

In loving memory of my little bro, Tyson John Ulibarri (1996 – 2014)

ACKNOWLEDGMENTS

I cannot describe how grateful I am for the mentors I have come across throughout my academic career. First and foremost, I would like to thank my advisor, Mathew. He guided me into the world of biochemistry, allowed me to explore my own research ideas and instilled confidence in me and my future as an independent researcher. I could not have asked for a better mentor for this five-year long journey. I am also grateful for my mentor from Westminster College, Dr. Tricia Shepherd. I was clueless when I entered undergrad and Tricia opened my mind to the idea of being a scientist. I cannot thank her enough for the numerous letters of recommendation that helped fund my undergraduate education and ultimately got me into graduate school. Thank you to Dr. Amanda Haes who mentored me through my first major research experience at the University of Iowa, and to Dr. Stephanie Padilla who was my most recent mentor at the Environmental Protection Agency (EPA). You have all been excellent role models – thank you for your guidance and kindness.

I am grateful for my lab mates who have made this process infinitely more enjoyable. In particular, Keelan Trull who has been alongside me as an original Tantamian. Thank you to Jason Conley, Megha Rajendran and others for your mentoring and friendship; to Sara Doan, my first undergrad who saw my project at some of the most challenging points; to Dr. Angeline Lyon and her lab for help with troubleshooting and purifying a difficult protein; and to my committee members, Dr. Mary Wirth, Garth Simpson, and Chittaranjan Das. I'd also like to acknowledge the National Science Foundation (NSF) for funding my graduate education through an NSF graduate research fellowship (DGE-1333468), the National Institutes of Health (NIH) for funding our peptide sensor project (R21 EY026425), and the EPA and the wonderful people I worked with during my internship.

Lastly, I am thankful for my family – my parents (mom, dad2 and dad), siblings, and grandma. My grandma supported me throughout undergrad and taught me the value of diligence and giving back to your community from a young age. I am especially grateful for my dad who raised me and instilled in me that while it may not be easy, you can do anything you set your mind to. He showed me what real hard work looks like and I cannot thank him enough for it.

TABLE OF CONTENTS

LIST OF TABLES

LIST OF FIGURES

ABSTRACT

Author: Norcross, Stevie. PhD
Institution: Purdue University
Degree Received: May 2019
Title: Engineering Genetically Encoded Fluorescent Biosensors to Study the Role of Mitochondrial Dysfunction and Inflammation in Parkinson's Disease
Committee Chair: Mathew Tantama

Parkinson's disease is a neurodegenerative disorder characterized by a loss of dopaminergic neurons, where mitochondrial dysfunction and neuroinflammation are implicated in this process. However, the exact mechanisms of mitochondrial dysfunction, oxidative stress and neuroinflammation leading to the onset and development of Parkinson's disease are not well understood. There is a lack of tools necessary to dissect these mechanisms, therefore we engineered genetically encoded fluorescent biosensors to monitor redox status and an inflammatory signal peptide with high spatiotemporal resolution. To measure intracellular redox dynamics, we developed red-shifted redox sensors and demonstrated their application in dual compartment imaging to study cross compartmental redox dynamics in live cells. To monitor extracellular inflammatory events, we developed a family of spectrally diverse genetically encoded fluorescent biosensors for the inflammatory mediator peptide, bradykinin. At the organismal level, we characterized the locomotor effects of mitochondrial toxicant-induced dopaminergic disruption in a zebrafish animal model and evaluated a behavioral assay as a method to screen for dopaminergic dysfunction. Pairing our intracellular redox sensors and our extracellular bradykinin sensors in a Parkinson's disease animal model, such as a zebrafish toxicant-induced model will prove useful for dissecting the role of mitochondrial dysfunction and inflammation in Parkinson's disease.

CHAPTER 1. INTRODUCTION

1.1 Mitochondrial Respiration, Dysfunction and Role in Parkinson's Disease

Mitochondria are organelles found in eukaryotic cells that act as the production site for much of the energy necessary for cellular function. This energy is produced in the form of adenosine triphosphate (ATP) through mitochondrial respiration, which includes the citric acid cycle and oxidative phosphorylation.[1,2] The citric acid cycle occurs in the mitochondrial matrix and involves the oxidation of acetyl-CoA derived from nutrient sources like carbohydrates and fats. Oxidative phosphorylation produces the majority of ATP and occurs at the mitochondrial inner membrane. There, a series of protein complexes (I, II, III and IV) and two soluble factors, coenzyme Q10 and cytochrome c, are known as the electron transport chain and transfer electrons from electron donors to electron acceptors like oxygen. These redox reactions produce protons that are pumped across the inner mitochondrial membrane to yield energy via a pH gradient and electric potential, and this energy powers the production of ATP by ATP synthase. Thus, mitochondria are crucial for cellular metabolism and survival.[2]

Mitochondria also play an important role in redox homeostasis and intracellular reactive oxygen species (ROS) signaling.[3] While ROS like superoxide and hydrogen peroxide are a normal by-product of mitochondrial respiration, mitochondrial dysfunction can result in high ROS levels that the cell is no longer able to effectively buffer. This excess ROS can damage important cellular components including DNA, proteins, and membranes, leading to further mitochondrial dysfunction and even cell death.[4] For example, ROS accumulation can lend to mitochondrial outer membrane permeabilization (MOMP), leading to release of intermembrane space proteins such as cytochrome c into the cytosol, and activation of the cell's apoptotic machinery.[5,6] Thus, it is not surprising that mitochondrial dysfunction and oxidative stress are implicated in various disorders, such as liver disease, optic neuropathy and neurodegenerative disorders, including Parkinson's disease (PD).[7–9] Our lab is particularly interested in studying the role of mitochondrial dysfunction and oxidative stress in PD.

Parkinson's disease is a movement disorder characterized by a loss of dopaminergic neurons in the substantia nigra pars compacta.[10,11] Mitochondrial dysfunction in PD was first hinted at in the late 1970's when a chemistry graduate student began synthesizing and self-

injecting the opioid drug, desmethylprodine.[12] Little did he know that his sloppy batches contained the impurity, 1-methyl-4-phenyl-1,2,3,6-tetrahydropyridine (MPTP), which caused onset of PD-like symptoms, including tremor and rigidity. Brain autopsy later revealed neuronal destruction in the substantia nigra.[12] A few years following this incident, doctors in California discovered four cases of patients showing rapid onset of parkinsonian symptoms after injecting a new "synthetic heroin," which was found to contain MPTP.[13,14] All patients responded to levodopa treatment similar to the prior case with the graduate student, which led them to conclude that MPTP induces parkinsonism.[12,13] It is now known that MPTP is converted to MPP+ in the brain, which is then selectively taken up by dopaminergic neurons, where it accumulates in mitochondria and inhibits complex I, resulting in ATP depletion, oxidative stress and cell death.[14,15] Similarly, the pesticide rotenone is a complex I inhibitor that results in dopaminergic cell loss and is used for neurotoxic-induced PD animal models.[16,17] Since these discoveries, there has been an explosion of research studying the connection between mitochondrial dysfunction and PD.[18,19]

In turn, several lines of evidence have implicated mitochondrial dysfunction and oxidative stress as key players in PD.[20] For example, several labs have reported reduced complex I and coenzyme Q10 activity in post-mortem brain tissue from PD patients.[21–24] Oxidative stress is further implicated since complex I is a major source of mitochondrial ROS and accumulation of α-synuclein inside mitochondria has been shown to lead to complex I defects and oxidative stress.[25–27] Dopaminergic neurons are hypothesized to be particularly susceptible to damage caused by mitochondrial stressors because of chronically elevated oxidative stress and high energy requirements.[11,28] Elevated oxidative stress is thought to be a product of the autonomous pacemaking properties of dopaminergic neurons, which is accompanied by calcium transients that have been shown to promote basal oxidative stress.[29,30] The extensive axonal arborization of dopaminergic neurons may also contribute to high basal levels of oxidative stress by placing high energy demands on the cells, thus making them more vulnerable to mitochondrial damage.[31,32]

In addition to the evidence of mitochondrial dysfunction in idiopathic PD, proteins found mutated in inherited PD and advances in our understanding of their molecular functions provide further support. For example, Parkin and PINK1 are genes associated with early-onset PD that encode for proteins that together participate in removal of damaged mitochondria through mitophagy.[33] Mutations in PINK1 and Parkin associated with PD result in accumulation of

damaged mitochondria, and it is hypothesized that these impaired mitochondrial dynamics are responsible for the loss of dopaminergic neurons.[34,35]

In summary, mitochondria are essential organelles that are central to cellular metabolism and energy homeostasis and thus, perturbation to the function of these organelles can be detrimental. Mitochondrial dysfunction and oxidative stress have been implicated in the etiology of Parkinson's disease on numerous fronts. For example, mitochondrial toxicants have been identified that cause parkinsonism, there is reduced mitochondrial function in brain tissue from PD patients, and there are genetic mutations associated with PD that lead to dysregulation of proteins involved in mitophagy. Despite this, the exact mechanisms of dopaminergic cell death in PD remain unclear. For example, is oxidative stress an initiating event that leads to mitochondrial dysfunction or is it a result of mitochondrial dysfunction that ultimately leads to cell demise? How does oxidative stress propagate throughout the cell and over time in these processes leading up to dopaminergic cell death? To answer these questions, we need tools to dissect the timeline of events and propagation of ROS and oxidative stress throughout the cell as neurodegeneration proceeds.

1.2 Methods for Measuring Oxidative Stress

Table 1.1 Indirect and direct methods for monitoring oxidative stress and major limitations of direct methods for live cell measurements.

Indirect Methods	**Direct Methods**	**Major Limitation of Direct Methods for Live Cell Measurements**
1.) Measure resulting damage to biomolecules	Measure ROS by electron spin resonance (ESR) spin trapping	Limited subcellular measurements
• Measure biomarkers of DNA or protein damage	Measure ROS using microelectrodes	Limited subcellular measurements
• Measure lipid peroxidation by-products	Measure ROS using fluorescent dyes	Can exhibit toxicity and cross reactivity
2.) Detect antioxidant levels • Measure glutathione ratio ([GSH]/[GSSG]) • Measure SOD and catalase activity	Measure ROS using fluorescent protein-based indicators	Can be complicated by pH sensitivity

Oxidative stress is the imbalance of ROS production and consumption that overwhelms the antioxidant defense system leading to biomolecular damage. There are numerous methods for measuring oxidative stress, which can be categorized as either indirect or direct methods. Indirect

methods measure the resulting effects or products of oxidative stress, which include 1.) measuring resulting damage to biomolecules and 2.) detection of antioxidant levels. Instead, direct methods measure the cellular ROS levels. These broad categories of oxidative stress measurements are summarized in Table 1.1 with example methods for each category. While indirect measures are informative, they are typically end-point assays that lack temporal resolution. In contrast, direct methods can monitor the transient ROS species and are typically more amenable to live cell measurements. Here, indirect and direct measures of ROS will be discussed, including the limitations of using direct measures in live cells.

There are several indirect measures of oxidative stress, which are informative because they tell about the effects of oxidative stress on the system. For example, oxidative stress often results in damage to biomolecules like DNA, proteins and lipids, which can be studied by measuring biomarkers of the damaged products. DNA subject to ROS attack generates a range of nucleotide modification products including the guanine oxidation product, 8-hydroxyguanine (8-oxo-Gua).[36] These oxidized DNA products can be measured by methods such as gas chromatography (GC)-MS, HPLC, liquid chromatography (LC)-MS and antibody-based techniques.[37] Protein oxidation on the other hand, is often more complex since 20 amino acids can be targeted by oxidation vs the four nucleotides in DNA.[38] Carbonyls are the most commonly used biomarkers of protein oxidative damage, which can be measured by spectrophotometric methods, HPLC and ELISA.[39]

During an oxidative attack antioxidants function to defend the cell against damage and aid in regaining redox homeostasis.[40] Thus, the levels and activity of these antioxidant species can be used as an indicator of cellular oxidative stress. For example, glutathione (GSH) is present at mM concentrations and is one of the most important antioxidants in aerobic cells.[41] GSH contains a thiol group that acts as an electron donor to reduce ROS and protein disulfides, which converts it to its oxidized glutathione disulfide form (GSSG). In a healthy cell most of glutathione remains in the reduced form, while under oxidative stress conditions the level of GSSG will increase.[42] Hence, the ratio of [GSH]/[GSSG] or the glutathione redox potential are commonly used indicators of redox status, which are typically measured by absorbance assays, fluorescence assays or HPLC.[43,44] Additionally, superoxide dismutase (SOD) and catalase are important cellular antioxidants. SOD catalyzes the conversion of superoxide (O_2^-) to hydrogen peroxide (H_2O_2) or oxygen (O_2), while catalase initiates the decomposition of H_2O_2 to H_2O and O_2. Thus, the activity

of these enzymes can be used as an indication of oxidative stress, which can be measured by activity gels or commercially available colorimetric activity assays.[45]

Direct measures of oxidative stress are defined as tools that give a dynamic readout of a specific ROS species, rather than a readout of a general effect of ROS (e.g. molecular damage, antioxidant activity). Electron spin resonance (ESR), also called electron paramagnetic resonance (EPR) is an example of a technique that can be used for direct ROS measurement. ESR is a spectroscopic method used to study unpaired electrons, where an unpaired electron can move between energy levels by either absorbing or emitting light that is typically in the microwave region. To measure the short-lived ROS species, ESR is paired with spin trapping, where compounds known as spin traps are used to covalently react with radicals, forming a more stable adduct. The ESR spectrum of the adduct is characteristic of the trapped free radicals, thus the identity of the ROS species can be inferred.[46] ESR measurements can be performed *in vitro* and *in vivo*, but due to low sensitivity, long recording times and low temperatures are typically required to detect the transient ROS.[47] Additionally, spin trap compounds must be added and be sufficiently lipophilic to gain access to cellular compartments, and adducts are often unstable in biological systems, which further complicates this method for live cell measurements.[48]

Electrodes and microelectrodes can be used to measure electroactive ROS species, including hydroxyl radical and superoxide.[49] These tools are limited in biological systems since ROS life span is typically short and must diffuse to the electrode surface to be detected.[50] Additionally, these tools are highly spatially restricted, where only the site of the electrode at the cell membrane or in the cell (with electrode insertion) can be monitored, rather than monitoring ROS throughout the cell or in multiple compartments, which becomes very difficult with electrodes.[50] Fluorescent dyes are another method used to measure ROS, which are much more frequently used in live cell measurements.[51] The ROS sensors, dihydroethidium (DHE), 2'-7'-dichlorodihydrofluorescein ($DCFH_2$), and mitochondrial-targeted DHE (mitoSOX) are particularly popular and measure ROS by a change in fluorescence.[51] For example, $DCFH_2$ is cell-permeable as its acetylated form, $DCFH_2$-DA, which is deacetylated by esterases in the cell to become nonfluorescent. Upon interacting with ROS, $DCFH_2$ is converted to DCF and can be visualized by its strong green fluorescence.[52] While these dyes are easily loaded and can measure ROS throughout the cell, they often suffer from lack of specificity and irreversibility, and they can exhibit toxicity and cross reactivity.[51,53]

Table 1.2 Characteristics of genetically encoded redox probes.

Redox Sensor	Specificity	Excitation (nm)	Emission (nm)	Ratiometric?	pH Sensitive?
rxYFP[54]	2 GSH/GSSG	512	523	No	Yes
roGFP1[55,56]	2 GSH/GSSG	400, 490	510	Yes	Negligible
roGFP2[55,56]	2 GSH/GSSG	400, 490	510	Yes	Negligible
Grx1-roGFP2[57]	2 GSH/GSSG	400, 490	510	Yes	Negligible
Orp1-roGFP2[58]	H2O2	400, 490	510	Yes	Negligible
HyPer[59]	H2O2	420, 500	516	Yes	Yes
HyPerRed[60]	H2O2	575	605	No	Yes
rxRFP1[61]	Thiol/disulfide equilibrium	576	600	No	Yes

Alternatively, fluorescent protein-based indicators are an excellent option for measuring ROS in live cells because they can be easily expressed in cells, targeted to subcellular compartments, are reversible and show low toxicity.[62,63] Thus, they allow for good spatiotemporal measurements of ROS and redox status. There are a number of genetically encoded sensors available for redox measurements that vary across several parameters including specificity, fluorescence readout and pH sensitivity (Table 1.2). The first genetically encoded redox sensor, rxYFP, was developed from wild type (WT) yellow fluorescent protein (YFP), where two cysteines were engineered in the beta barrel (Cys149 and Cys202).[54] These cysteines reversibly form disulfide-bonds in response to equilibration with the cellular redox status primarily due to reduced and oxidized glutathione, which in turn results in a change in the fluorescent signal.[54,64] Since the development of rxYFP several other genetically encoded redox sensors have been engineered, including one of the most popular sensors, the reduction-oxidation sensitive GFP (roGFP).[55,56,65] While the roGFP sensors (roGFP1 and roGFP2) also sense through thiol/disulfide equilibrium they have been further engineered to be specific to glutathione and H_2O_2 (Table 1.2).[57,58] The glutathione version of roGFP (Grx1-roGFP2) was engineered by fusing the human glutaredoxin (Grx1) to roGFP2, while the H_2O_2 version (roGFP2-Orp1) was engineered by fusing the yeast thiol peroxidase (Orp1) to roGFP2.[57,58] The HyPer sensors are a family of genetically encoded probes that are also specific for H_2O_2 (Table 1.2), which were engineered by inserting a fluorescent protein into the *Escherichia coli* hydrogen peroxide sensing protein (OxyR).[59,66]

One of the major advantages of genetically encoded redox sensors is that they can be readily targeted to subcellular compartments, which makes them excellent candidates for

measuring compartmental oxidative stress.[67,68] To measure oxidative stress in more than one cellular compartment at the same time spectrally diverse sensors are needed. Thus, red fluorescent genetically encoded redox sensors have been developed, which can be used in combination with a spectrally distinct sensor for dual compartment imaging (Table 1.2).[60,61,69] To further add to this toolkit, we engineered red-shifted roGFP variants also known as roGFP-RFP sensors, which are discussed extensively in Chapter 2.[70]

In summary, there are various methods available for measuring oxidative stress, which are being classified as either indirect or direct methods. Indirect methods measure biomolecular damage caused by oxidative stress or antioxidant levels, while direct methods measure ROS. Direct measurements of ROS include ESR, microelectrodes, fluorescent dyes and genetically encoded fluorescent sensors. ESR and microelectrodes tend to be spatially limited, while fluorescent dyes and genetically encoded sensors are more amenable to live cell and subcellular measurements. To aid in simultaneous, dual compartment imaging we engineered red-shifted genetically encoded redox sensors.

1.3 The Kallikrein-Kinin System, Neuroinflammation and Implications in Parkinson's Disease

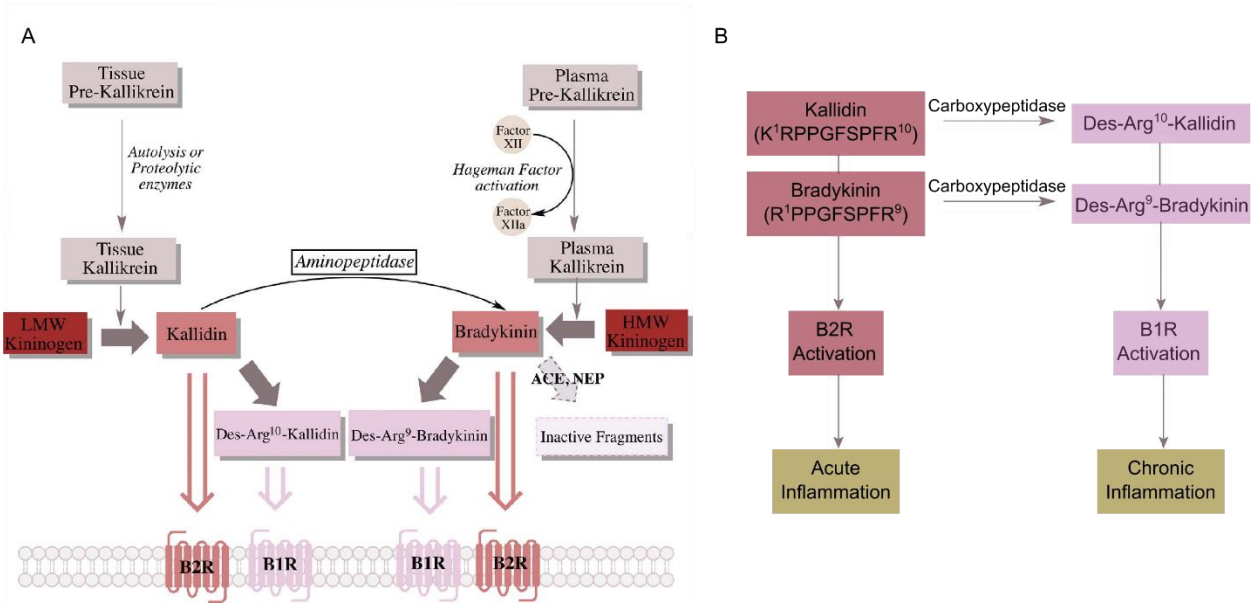

Figure 1.1 Overview of the kallikrein-kinin system (KKS), bradykinin receptor activation and role in inflammation.

(A) Tissue kallikrein is activated by proteolytic enzymes and converts LMW kininogen into kallidin. An aminopeptidase can further convert kallidin into bradykinin. Hageman factor activates plasma kallikrein, which converts HMW kininogen into bradykinin. Kallidin and bradykinin both primarily agonize B2R and can be further broken down into Des-Arg^{10}-kallidin and Des-Arg^{9}-bradykinin, which act on B1R. ACE and NEP can also degrade kallidin and bradykinin. Image borrowed and modified with permission from Elsevier.[71] (B) Kallidin and bradykinin both activate the constitutively expressed receptor, B2R, which leads to acute inflammation. Conversely, the carboxypeptidase converted products, Des-Arg^{10}-kallidin and Des-Arg^{9}-bradykinin, activate the stress-induced B1R, which leads to chronic inflammation.

The kallikrein-kinin system (KKS) is an inflammatory response system involved in numerous physiological pathways, including blood pressure regulation, vascular permeability, inflammation, analgesia and pain transmission.[72,73] The two main components of the KKS are the kallikrein enzymes, tissue kallikrein and plasma kallikrein, which are derived from prekallikrein by proteolytic enzymes or activation of Hageman factor (Factor XII), respectively (Figure 1.1).[73,74] These kallikreins are serine proteases that primarily function to liberate inflammatory peptides from kininogens. Specifically, tissue kallikrein cleaves low molecular weight (LMW) kininogen to produce kallidin (KRPPGFSPFR), while plasma kallikrein cleaves high molecular weight (HMW) kininogen to produce bradykinin (RPPGFSPFR).[73] Kallidin and bradykinin can be further

broken down by the kininase I-type carboxypeptidases into des-Arg^{10}-kallidin and des-Arg^{9}-kallidin, respectively. Kallidin can also be converted to bradykinin by aminopeptidase, and both kallidin and bradykinin can be converted to inactive fragments after digestion by the kininase II, angiotensin converting enzyme (ACE) or neutral endopeptidase (NEP).[75,76] Together, these kinin peptides and their active breakdown products make up a diverse group of inflammatory pathway mediators by acting on the kinin receptors.

Table 1.3 Human kinin receptor affinities determined using radioligand binding assays.

Peptide	**B1R Affinity, K_i (nM)**[77]	**B2R Affinity, K_i (nM)**[78]
Killidin	2.54	0.63
Bradykinin	>10,000	0.54
des-Arg^{10}-Kallidin	0.12	>30,000
des-Arg^{9}-Bradykinin	1930	8,100

The kinin receptor family consists of the G protein-coupled receptors, B1R and B2R. B2R binds kallidin and bradykinin, while B1R primarily binds the des-Arg kinin peptides (Figure 1.1, Table 1.3).[79] Additionally, these receptors are differentiated by their surface expression properties, where B2R is constitutively expressed at the cell surface and rapidly endocytosed and recycled upon ligand binding. On the other hand, B1R shows low basal expression in healthy conditions and is primarily expressed at the cell surface upon stimulus by proinflammatory cytokines following injury and it is slow to desensitize upon binding agonist.[80] Based on this differential regulation of kinin receptors and their overall function, B2R is typically thought to be involved in acute inflammation and pain responses, while B1R is thought to be involved in chronic inflammation (Figure 1.1).[80,81]

In the CNS, the kinin receptors and KKS components are thought to play an important role in neuroinflammation.[81] They are implicated in blood brain barrier (BBB) permeability, leukocyte entrance and cytokine release in the CNS leading to inflammation.[82–85] For example, bradykinin has been shown to regulate the expression of a BBB tight junction protein Claudin-5.[86] Specifically, Zhou et al showed that treating rat brain microvascular endothelial cells (BMECs) with bradykinin led to calcium-induced calcium release and down regulation of claudin-5 leading to BBB disruption.[86] Further, B2R activation and subsequent ROS production is implicated in BBB

disruption.[87] For example, rats acutely dosed with bradykinin showed increased BBB permeability caused by B2R activation leading to arachidonic acid formation and subsequent ROS formation.[84,88]

Indeed, all components of the KKS have been found in the CNS, including pre-kallikrein, tissue and plasma kallikrein, the kininogens, kininases and kinin receptors.[81,89] Additionally, despite the short half-life of the kinins (~30 seconds)[90], bradykinin has been detected at relatively high levels in human cerebral spinal fluid (CSF).[91,92] Not surprisingly, the kinin receptors are differentially expressed in the CNS. Here, B1R is expressed at lower basal levels in the brain, where it is localized on neurons of the hypothalamus, spinal cord and thalamus.[93] Interestingly, B1R in rat brain has been difficult to detect but was measured at increased levels in an epileptic rat model, which supports the role of B1R in response to injury.[94] On the other hand, B2R is more highly distributed in the brain as it is found on neurons of the brain stem, basal nuclei, cerebral cortex, thalamus and hypothalamus, and in the endothelial lining of the superior sagittal dural sinus and ependyma of the lateral and third ventricles.[93,95]

The distribution and function of the KKS components in the CNS provides significant insight into the role of kinin signaling in neuroinflammation. For example, B2R is expressed on astrocytes and has been shown to be important in glial-neuron communication in inflammation.[89,96] Here, astrocytic B2R activation leads to an increase in intracellular Ca^{2+} concentrations, glutamate release and NMDA receptor-mediated increase in neuronal Ca^{2+} levels.[97–100] B2R activation on astrocytes also leads to ROS, matrix metalloproteinase and carbon monoxide production, which may lend to neuronal death.[101,102] Additionally, microglia express kinin receptors and B1R activation on microglia has been shown to trigger microglial migration and have anti-inflammatory effects in LPS-induced microglial activation.[100,103] Thus, it is not surprising that the KKS and its role in neuroinflammation is suspected in the development and progression of several neurological disorders including, Alzheimer's disease, stroke and Parkinson's disease.[71,81]

Of interest is the involvement of the KKS in PD since neuroinflammation is thought to play a role in its pathogenesis.[104,105] For example, morphological changes in endothelial cells of the substantia nigra of PD patients have been observed and suggest BBB disruption, which may lead to peripheral immune cell infiltration and increased inflammation.[106–108] Higher levels of proinflammatory cytokines including IL2, IL6 and tumor necrosis factor α (TNFα) have also been found in brain, CSF and serum samples from PD patients.[109–111] Significantly, activated microglia

have been observed in the substantia nigra pars compacta of human post-mortem PD brain samples.[112] Positron emission tomography (PET) studies have also shown increased microglial activation in several brain regions of PD patients.[113,114]

Altogether, there is significant evidence for neuroinflammatory involvement in PD, however, the exact role of neuroinflammation in the onset and development of PD remains unclear. Indeed, the role of the KKS in neuroinflammatory events of PD would be of interest to study. For example, is B2R activation involved in BBB permeability in PD models and can B2R antagonism aid in reduced CNS inflammatory events relevant to PD? Additionally, an increased number of astrocytes have been found in the substantia nigra of postmortem PD brain samples.[115,116] What role do these astrocytes play in neuroinflammation in PD and is the KKS involved in this process? As previously mentioned, B2R activation on astrocytes leads to ROS production and may aid in neuronal death. Does astrocytic B2R activation in the substantia nigra of PD models lend to dopaminergic cell death? To better dissect the role of the KKS and neuroinflammation in PD we need tools that allow us to monitor KKS signaling in live animals (e.g. PD animal models) and in real-time.

1.4 Methods for Measuring KKS Peptide Signaling

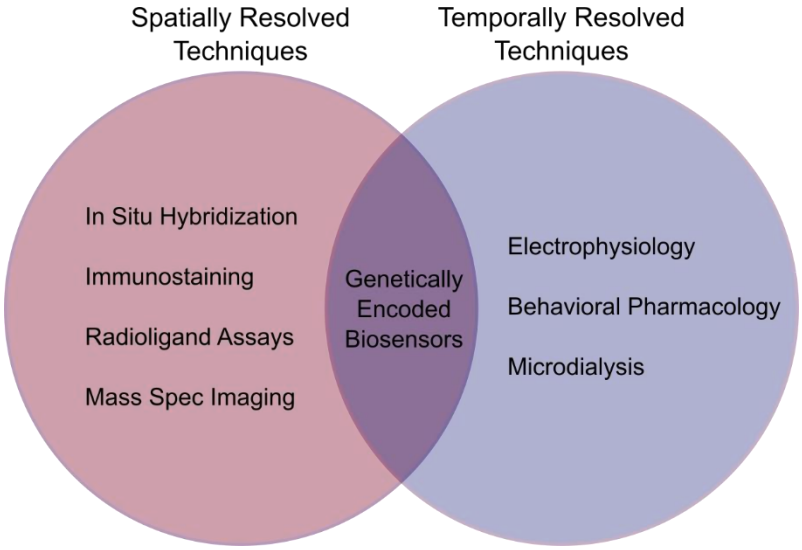

Figure 1.2 Venn diagram of methods to measure KKS signaling components, including kallikrein, kininogen, kinin peptides and kinin receptors.

Methods are primarily limited to high spatial or temporal resolution. However, genetically encoded fluorescent biosensors of kinin peptides have the potential to monitor KKS signaling at high spatiotemporal resolution though no such tools are currently available.

The kallikrein kinin system consists of several protein and peptide components, including the peptide-precursor kininogens, proteolytic kallikreins, the kinin peptide products and the peptide-activated kinin receptors (B1R and B2R). As previously mentioned, all these components have been identified and measured in the CNS. These measurements were performed using a variety of techniques and while these methods have been useful for dissecting the distribution and function of these KKS components, they are limited in either the spatial or temporal regime (Figure 1.2). However, genetically encoded fluorescent biosensors for kinin peptides have the potential of monitoring kinin peptide signaling in the CNS with high spatiotemporal resolution. Herein, these techniques and examples of their application in studying the KKS in the brain will be discussed.

In situ hybridization is a method that has been used to reveal the presence of tissue kallikrein mRNA transcripts in brain regions like the cerebral cortex, hypothalamus, brain stem and pineal gland of rat brain.[117] However, while *in situ* hybridization is a valuable method because it is specific and shows good spatial resolution, it only measures DNA and RNA transcripts, which does not indicate whether these transcripts are functionally expressed. Thus, it is useful to follow *in situ* hybridization with an alternate technique that measures the protein or peptide product, such

as immunostaining or mass spectrometry imaging. In this case, tissue kallikrein has also been measured in human brain by immunostaining and has been found on neurons of the brain stem, cerebral gray matter, hypothalamus, thalamus and epithelial cells of the choroid plexus.[118] Further, immunostaining and radioligand assays have revealed differential expression of the bradykinin receptors (B1R and B2R) throughout the brain[93–95,119]. The techniques used here are important because they have been implemented to determine the specific locations of the KKS components, as well as show that they are present throughout the brain. However, these techniques are temporally limited and are typically used as end-point assays, making them difficult to implement to study the functional activity of these components.

Alternatively, techniques that show good temporal resolution can be used to study KKS signaling (Figure 1.2). For example, electrophysiology is a temporally resolved technique that can be used for functional measurements, and it has been implemented to study the intracellular effects of bradykinin receptor activation. In one study, electrophysiology was used and showed that bradykinin induces a depolarization of astrocytes.[120] Another study confirmed this inward current in response to bradykinin in addition to revealing a corresponding rapid rise in intracellular calcium in astrocytes.[97] Similarly, microdialysis has been used to tease apart the functional effects of bradykinin signaling in the brain. For example, microdialysis was used to measure glutamate release in the hippocampus of kindled rat brain after bradykinin perfusion, which revealed bradykinin-mediated glutamate release.[121] While these methods are useful for teasing apart the functional effects of KKS signaling, they are generally impeded by the number of cells and positions that can be measured simultaneously and low sampling volumes. In addition to measuring the effects of KKS signaling, it would be informative to directly measure the kinin peptides that act as the signaling molecules in this system. We are particularly interested in measuring bradykinin, which primarily acts on the constitutively expressed B2 receptor (Table 1.3).

Brain kinin peptide levels were first estimated using a radioimmunoassay to measure bradykinin in human cerebral spinal fluid, where 0.05 nM (50 fmol/mL) bradykinin was detected.[91] More recently, bradykinin CSF levels in healthy patients were determined by a combination of liquid phase extraction, HPLC and radioimmunoassay and were determined to be lower at 0.0012 nM (1.2 fmol/mL), which is likely due to improved specificity of their technique.[92] Of course, these CSF concentrations may not be representative of bradykinin levels in the brain since plasma

constituents in CSF may contribute to these levels. Thus, bradykinin levels have been further determined in homogenized brain samples, again using radioimmunoassays. In rat brain, bradykinin levels have been estimated to be 100 to 600 fmol/g (~0.1 – 1 nM, assuming 70% water, where 1 g ≈ 0.7 mL) with the pituitary gland containing the highest levels of 4,135 fmol/g (~6 nM) followed by medulla oblongata with 912 fmol/g (~1 nM).[122,123] However, more recent studies have found lower levels of bradykinin in mouse brain at 1.9 to 3.1 fmol/g (~1 pM).[124,125] Here, radioimmunossays have been particularly valuable in measuring bradykinin levels in the brain because they are sensitive and provide low detection limits. However, similar to the other spatially resolved techniques, they do not permit real-time measurements of bradykinin. This makes measuring transient bradykinin signals quite difficult. In fact, while these transient bradykinin signals are anticipated to be at levels closer to the affinity of the B2 receptor (0.54 nM, Table 1.3), they have yet to be directly measured in the CNS.

To measure KKS signaling new tools are needed that provide a real-time readout of the KKS signaling molecules (e.g. bradykinin) with high spatiotemporal resolution. Genetically encoded fluorescent biosensors are tools that can fill this gap because they can be readily targeted and expressed in live cells and live animals to continuously monitor neuronal signaling at the synaptic, circuit and whole brain level. For example, genetically encoded calcium indicators (GECIs) are frequently implemented to monitor cytosolic calcium transients in neurons as a proxy for directly measuring action potentials.[126] Numerous versions of these GECIs are available and are suitable for measuring the wide range of calcium levels that can be encountered *in vivo* (nm – mM) in addition to fast kinetics that allow them to monitor transient and short lived calcium signals.[127,128] In fact, these tools are so well suited and useful for *in vivo* measurements that they have been implemented to study neuronal signaling in the majority of commonly used animal models including worm, fly, zebrafish, mice and non-human primate.[129–133] Obviously, there is enormous potential for the use of genetically encoded sensors to study signaling in the CNS. However, no such tools for measuring bradykinin or peptides in general are available to date. Thus, we aim to engineer the first genetically encoded sensor for measuring bradykinin in live cells and live animals at high spatiotemporal resolution. Herein, progress will be reported on our quest to engineer a bradykinin sensor.

1.5 Specific Aims and Introduction to Chapters

1.5.1 Specific Aim 1 – Engineer Red-Shifted Redox Sensor for Simultaneous Dual Compartment Imaging (Chapter 2)

Oxidative stress in the mitochondria of dopaminergic neurons is implicated in Parkinson's disease. However, open questions remain about the exact role of oxidative stress in cell death. For example, where does oxidative stress initiate in the cell and how does it propagate throughout the cell leading up to cell death? To answer these questions, better tools are needed to dissect the compartment specific and cross-compartmental redox dynamics. For this reason, we engineered red-shifted redox sensors to simultaneously monitor redox dynamics in two separate compartments. In this chapter, the design, library screening, and characterization of a family of genetically encoded redox sensors is described. Moreover, proof of concept experiments are described, which show implementation of these sensors for dual compartment redox imaging in addition to measuring single cell heterogeneity in response to reductive and metabolic stressors.

1.5.2 Specific Aim 2 – Evaluate a Locomotor Assay to Screen for Dopaminergic Disruption in Zebrafish Larvae as an Animal Model of PD (Chapter 3)

To study the etiology of PD, toxicant-induced animal models are often employed, which involve treating an animal with a chemical that has been shown to disrupt dopaminergic signaling and/or result in PD-like symptoms. Herein, we developmentally treated zebrafish with MPTP and ziram to evaluate a light:dark transition locomotor assay for screening for dopaminergic disruption. In this chapter, the overt toxicity of several mitochondrial toxicants and chemicals implicated in PD is shown, and behavioral effects of developmental exposure to a subset of these chemicals is described. Additionally, MPTP, a chemical commonly used in toxin-induced animal models, is further characterized for acute behavioral effects in zebrafish.

1.5.3 Specific Aim 3 – Characterize Oligopeptide-Binding Proteins and Test Engineering Strategies for the Development of a Bradykinin Sensor (Chapter 4 & 5)

Bradykinin is an inflammatory mediator peptide involved in blood vessel dilation, acute inflammation and pain responses. In the CNS, bradykinin receptor activation is implicated in blood brain barrier permeability, leukocyte entrance and neuroinflammation. Thus, to study the role of

inflammation in CNS disorders, including PD, we engineered genetically encoded fluorescent bradykinin biosensors. Our sensor design employs an oligopeptide-binding protein as a sensing domain for bradykinin binding. Thus, in chapter 4 we first extensively characterize the effects of pH and temperature on bradykinin binding and the stability of an oligopeptide-binding protein. In chapter 5, we characterize the thermal stability of additional sensing domains and go on to engineer sensors for bradykinin. We show that bradykinin sensors can be engineered using a single fluorescent protein-based approach and a FRET-based sensor design strategy to produce sensors with diverse spectral properties.

1.6 References

1. Fernie, A. R., Carrari, F. & Sweetlove, L. J. Respiratory metabolism: Glycolysis, the TCA cycle and mitochondrial electron transport. *Curr. Opin. Plant Biol.* **7,** 254–261 (2004).

2. Vakifahmetoglu-Norberg, H., Ouchida, A. T. & Norberg, E. The role of mitochondria in metabolism and cell death. *Biochem. Biophys. Res. Commun.* **482,** 426–431 (2017).

3. Shadel, G. S. & Horvath, T. L. Mitochondrial ROS Signaling in Organismal Homeostasis. *Cell* **163,** 560–569 (2015).

4. Ott, M., Gogvadze, V., Orrenius, S. & Zhivotovsky, B. Mitochondria, oxidative stress and cell death. *Apoptosis* **12,** 913–922 (2007).

5. Kamata, H. *et al.* Reactive oxygen species promote TNFα-induced death and sustained JNK activation by inhibiting MAP kinase phosphatases. *Cell* **120,** 649–661 (2005).

6. Tajeddine, N. How do reactive oxygen species and calcium trigger mitochondrial membrane permeabilisation? *Biochim. Biophys. Acta - Gen. Subj.* **1860,** 1079–1088 (2016).

7. Vafai, S. B. & Mootha, V. K. Mitochondrial disorders as windows into an ancient organelle. *Nature* **491,** 374–383 (2012).

8. Suomalainen, A. & Battersby, B. J. Mitochondrial diseases: The contribution of organelle stress responses to pathology. *Nat. Rev. Mol. Cell Biol.* **19,** 77–92 (2018).

9. Lin, M. T. & Beal, M. F. Mitochondrial dysfunction and oxidative stress in neurodegenerative diseases. *Nature* **443,** 787–795 (2006).

10. Fearnley, J. M. & Lees, A. J. Ageing and parkinson's disease: Substantia nigra regional selectivity. *Brain* **114,** 2283–2301 (1991).

11. Giguère, N., Burke Nanni, S. & Trudeau, L.-E. On Cell Loss and Selective Vulnerability of Neuronal Populations in Parkinson's Disease. *Front. Neurol.* **9,** (2018).

12. Davis, G. C. *et al.* Chronic parkinsonism secondary to intravenous injection of meperidine analogues. *Psychiatry Res.* **1,** 249–254 (1979).

13. Langston, J. William; Ballard, Philip, Tetrud, James W.; Irwin, I. Chronic Parkinsonism in Humans due to a Product of Meperidine-Analog Synthesis Author (s): J . William Langston , Philip Ballard , James W . Tetrud , Ian Irwin Published by : American Association for the Advancement of Science Stable URL : http://www.js. *Adv. Sci.* **219,** 979–980 (1983).

14. Langston, J. W. The MPTP story. *J. Parkinsons. Dis.* **7,** S11–S19 (2017).

15. Ramsay, R. R., Kowal, A. T., Johnson, M. K., Salach, J. I. & Singer, T. P. The inhibition site of MPP+, the neurotoxic bioactivation product of 1-methyl-4-phenyl-1,2,3, 6-tetrahydropyridine is near the Q-binding site of NADH dehydrogenase. *Arch. Biochem. Biophys.* **259,** 645–649 (1987).

16. Sherer, T. B. *et al.* Mechanism of toxicity in rotenone models of Parkinson's disease. *J Neurosci* **23,** 10756–10764 (2003).

17. Johnson, M. E. & Bobrovskaya, L. An update on the rotenone models of Parkinson's disease: Their ability to reproduce the features of clinical disease and model gene-environment interactions. *Neurotoxicology* **46,** 101–116 (2015).

18. Bose, A. & Beal, M. F. Mitochondrial dysfunction in Parkinson's disease. *J. Neurochem.* **139,** 216–231 (2016).

19. Grunewald, Anne; Kumore, Kishore R.; Sue, C. M. New insights into the complex role of mitochondria in Parkinson's disease. *Prog. Neurobiol.* (2018).

20. Vera Dias, Eunsung Junn, M. M. M. The Role of Oxidative Stress in Parkinson's Disease. *J Park. Dis* **3,** 461–491 (2014).

21. Schapira, A. H. V. *et al.* Mitochondrial Complex I Deficiency in Parkinson's Disease. *J. Neurochem.* **54,** 823–827 (1990).

22. Schapira, A. H. V. *et al.* Anatomic and Disease Specificity of NADH CoQ1Reductase (Complex I) Deficiency in Parkinson's Disease. *J. Neurochem.* **55,** 2142–2145 (1990).

23. Shults, C. W., Haas, R. H., Passov, D. & Beal, M. F. Coenzyme Q10 levels correlate with the activities of complexes I and II/III in mitochondria from Parkinsonian and nonparkinsonian subjects. *Ann. Neurol.* **42,** 261–264 (1997).

24. Keeney, P. M. Parkinson's Disease Brain Mitochondrial Complex I Has Oxidatively Damaged Subunits and Is Functionally Impaired and Misassembled. *J. Neurosci.* **26,** 5256–5264 (2006).

25. Murphy, M. P. How mitochondria produce reactive oxygen species. *Biochem. J.* **417,** 1–13 (2009).

26. Hsu, L. J. *et al.* A-Synuclein Promotes Mitochondrial Deficit and Oxidative Stress. *Am. J. Pathol.* **157,** 401–410 (2000).

27. Devi, L., Raghavendran, V., Prabhu, B. M., Avadhani, N. G. & Anandatheerthavarada, H. K. Mitochondrial import and accumulation of α-synuclein impair complex I in human dopaminergic neuronal cultures and Parkinson disease brain. *J. Biol. Chem.* **283,** 9089–9100 (2008).

28. Surmeier, James D.; Guzman, Jaime N.; Sanchez-Padilla, Javier; Schumacker, P. T. The role of calcium and mitochondrial oxidant stress in the loss of substantia nigra pars compacta dopaminergic neurons in Parkinson's disease. *Neuroscience* 221–231 (2011). doi:10.1016/j.neuroscience.2011.08.045.The

29. Guzman, J. N. *et al.* Oxidant stress evoked by pacemaking in dopaminergic neurons is attenuated by DJ-1. *Nature* **468,** 696–700 (2010).

30. Goldberg, J. A. *et al.* Calcium entry induces mitochondrial oxidant stress in vagal neurons at risk in Parkinson's disease. *Nat. Neurosci.* **15,** 1414–1421 (2012).

31. Bolam, J. P. & Pissadaki, E. K. Living on the edge with too many mouths to feed: Why dopamine neurons die. *Mov. Disord.* **27,** 1478–1483 (2012).

32. Pacelli, C. *et al.* Elevated Mitochondrial Bioenergetics and Axonal Arborization Size Are Key Contributors to the Vulnerability of Dopamine Neurons. *Curr. Biol.* **25,** 2349–2360 (2015).

33. Pickrell, Alicia M.; Youle, R. J. The Roles of PINK1, Parkin and Mitochondrial Fidelity in Parkinson's Disease. *Neuron* **85,** 257–273 (2016).

34. Gautier, C. A., Kitada, T. & Shen, J. Loss of PINK1 causes mitochondrial functional defects and increased sensitivity to oxidative stress. *Proc. Natl. Acad. Sci.* **105,** 11364–11369 (2008).

35. Barodia, S. K., Creed, R. B. & Goldberg, M. S. Parkin and PINK1 functions in oxidative stress and neurodegeneration. *Brain Res. Bull.* **133,** 51–59 (2017).

36. Cadet, J. & Wagner, J. R. DNA Base Damage by Reactive Oxygen Species,Oxidizing Agents, and UV Radiation. *Cold Spring Harb. Perspect. Biol.* **5,** 1–16 (2013).

37. Guetens, G., De Boeck, G., Highley, M., van Oosterom, A. & de Bruijn, E. Oxidative DNA damage: Biological significance and methods of analysis. *Crit. Rev. Clin. Lab. Sci.* **39,** 331–457 (2002).

38. Davies, M. J. Protein oxidation and peroxidation. *Biochem. J.* **473,** 805–825 (2016).

39. Weber, D., Davies, M. J. & Grune, T. Determination of protein carbonyls in plasma, cell extracts, tissue homogenates, isolated proteins: Focus on sample preparation and derivatization conditions. *Redox Biol.* **5,** 367–380 (2015).

40. Birben, E. *et al.* Oxidative Stress and Antioxidant Defense. *WAO J.* **5,** 9–19 (2012).

41. Lushchak, V. I. Glutathione Homeostasis and Functions: Potential Targets for Medical Interventions. *J. Amino Acids* **2012,** 1–26 (2012).

42. Owen, J. B. & Butterfield, D. A. Measurement of Oxidized/Reduced Glutathione Ratio. in *Protein Misfolding and Cellular Stress in Disease and Aging: Concepts and Protocols* (eds. Bross, P. & Gregersen, N.) 269–277 (Humana Press, 2010). doi:10.1007/978-1-60761-756-3_18

43. Rahman, I., Kode, A. & Biswas, S. K. Assay for quantitative determination of glutathione and glutathione disulfide levels using enzymatic recycling method. *Nat. Protoc.* **1,** 3159–3165 (2007).

44. Forman, H. J., Zhang, H. & Rinna, A. Glutathione: Overview of its protective roles, measurement, and biosynthesis. *Mol. Aspects Med.* **30,** 1–12 (2010).

45. Weydert, C. J. & Cullen, J. J. Measurement of superoxide dismutase, catalase and glutathione peroxidase in cultured cells and tissue. *Nat. Protoc.* **5,** 51–66 (2010).

46. Suzen, S., Gurer-Orhan, H. & Saso, L. Detection of reactive oxygen and nitrogen species by electron paramagnetic resonance (EPR) technique. *Molecules* **22,** 1–9 (2017).

47. Villamena, F. A. & Zweier, J. L. Detection of Reactive Oxygen and Nitrogen Species by EPR Spin Trapping. *Antioxid. Redox Signal.* **6,** 619–629 (2004).

48. Abbas, K., Babić, N. & Peyrot, F. Use of spin traps to detect superoxide production in living cells by electron paramagnetic resonance (EPR) spectroscopy. *Methods* **109,** 31–43 (2016).

49. Calas-Blanchard, C., Catanante, G. & Noguer, T. Electrochemical Sensor and Biosensor Strategies for ROS/RNS Detection in Biological Systems. *Electroanalysis* **26,** 1277–1286 (2014).

50. Dumitrescu, E. & Andreescu, S. *Bioapplications of Electrochemical Sensors and Biosensors*. *Methods in Enzymology* **589,** (Elsevier Inc., 2017).

51. Wang, X. *et al.* Imaging ROS signaling in cells and animals. *J. Mol. Med.* **91,** 917–927 (2013).

52. Chen, X., Zhong, Z., Xu, Z., Chen, L. & Wang, Y. 2′,7′-Dichlorodihydrofluorescein as a fluorescent probe for reactive oxygen species measurement: Forty years of application and controversy. *Free Radic. Res.* **44,** 587–604 (2010).

53. Woolley, J. F., Stanicka, J. & Cotter, T. G. Recent advances in reactive oxygen species measurement in biological systems. *Trends Biochem. Sci.* **38,** 556–565 (2013).

54. Østergaard, H., Henriksen, A., Hansen, F. G. & Winther, J. R. Shedding light on disulfide bond formation: Engineering a redox switch in green fluorescent protein. *EMBO J.* **20,** 5853–5862 (2001).

55. Hanson, G. T. *et al.* Investigating Mitochondrial Redox Potential with Redox-sensitive Green Fluorescent Protein Indicators. *J. Biol. Chem.* **279,** 13044–13053 (2004).

56. Dooley, C. T. *et al.* Imaging dynamic redox changes in mammalian cells with green fluorescent protein indicators. *J. Biol. Chem.* **279,** 22284–22293 (2004).

57. Gutscher, M. *et al.* Real-time imaging of the intracellular glutathione redox potential. *Nat. Methods* **5,** 553–559 (2008).

58. Gutscher, M. *et al.* Proximity-based protein thiol oxidation by H2O2-scavenging peroxidases. *J. Biol. Chem.* **284,** 31532–31540 (2009).

59. Belousov, V. V. *et al.* Genetically encoded fluorescent indicator for intracellular hydrogen peroxide. *Nat. Methods* **3,** 281–286 (2006).

60. Belousov, V. V. *et al.* Red fluorescent genetically encoded indicator for intracellular hydrogen peroxide. *Nat. Methods* **3,** 281–286 (2014).

61. Fan, Y., Chen, Z. & Ai, H. W. Monitoring Redox dynamics in living cells with a redox-sensitive red fluorescent protein. *Anal. Chem.* **87,** 2802–2810 (2015).

62. Pouvreau, S. Genetically encoded reactive oxygen species (ROS) and redox indicators. *Biotechnol. J.* **9,** 282–293 (2014).

63. Bilan, D. S. & Belousov, V. V. New tools for redox biology: from imaging to manipulation. *Free Radic. Biol. Med.* 1–22 (2016). doi:10.1016/j.freeradbiomed.2016.12.004

64. Østergaard, H., Tachibana, C. & Winther, J. R. Monitoring disulfide bond formation in the eukaryotic cytosol. *J. Cell Biol.* **166,** 337–345 (2004).

65. Schwarzländer, M., Dick, T. P., Meyer, A. J. & Morgan, B. Dissecting Redox Biology using Fluorescent Protein Sensors. *Antioxid. Redox Signal.* **00,** 150413084017007 (2015).

66. Bilan, D. S. & Belousov, V. V. HyPer Family Probes: State of the Art. *Antioxid. Redox Signal.* **24,** 731–751 (2016).

67. Pendin, D., Greotti, E., Lefkimmiatis, K. & Pozzan, T. Exploring cells with targeted biosensors. *J. Gen. Physiol.* **149,** 1–36 (2017).

68. Kostyuk, A. I., Panova, A. S., Bilan, D. S. & Belousov, V. V. Redox biosensors in a context of multiparameter imaging. *Free Radic. Biol. Med.* **128,** 23–39 (2018).

69. Fan, Y. & Ai, H. W. Development of redox-sensitive red fluorescent proteins for imaging redox dynamics in cellular compartments. *Anal. Bioanal. Chem.* **408,** 2901–2911 (2016).

70. Norcross, S. *et al.* Extending roGFP Emission via Förster-Type Resonance Energy Transfer Relay Enables Simultaneous Dual Compartment Ratiometric Redox Imaging in Live Cells. *ACS Sensors* **2,** 1721–1729 (2017).

71. Nokkari, A. *et al.* Implication of the Kallikrein-Kinin system in neurological disorders: Quest for potential biomarkers and mechanisms. *Prog. Neurobiol.* **165–167,** 26–50 (2018).

72. Lalmanach, G., Naudin, C., Lecaille, F. & Fritz, H. Kininogens: More than cysteine protease inhibitors and kinin precursors. *Biochimie* **92,** 1568–1579 (2010).

73. Yarovaya, G. A. & Neshkova, A. E. Past and Present Research on the Kallikrein Kinin System (On the 90th Anniversary of the Discovery of the System). *Russ. J. Bioorganic Chem.* **41,** 245–259 (2015).

74. Schmaier, A. H. The contact activation and kallikrein / kinin systems : pathophysiologic and physiologic activities. *J. Thromb. Haemost.* **14,** 28–39 (2016).

75. Sheikh, I. A. & Kaplan, A. P. Mechanism of digestion of bradykinin and lysylbradykinin (kallidin) in human serum. *Biochem. Pharmacol.* **38,** 993–1000 (1989).

76. Erdös, E. G. Angiotensin I converting enzyme and the changes in our concepts through the years: Lewis K. Dahl memorial lecture. *Hypertension* **16,** 363–370 (1990).

77. Bastian, S., Loillier, B., Paquet, J. L. & Pruneau, D. Stable expression of human kinin B1 receptor in 293 cells: Pharmacological and functional characterization. *Br. J. Pharmacol.* **122,** 393–399 (1997).

78. Hess, J. F. *et al.* Differential pharmacology of cloned human and mouse B2 bradykinin receptors. *Mol. Pharmacol.* **45,** 1–8 (1994).

79. Leeb-lundberg, F., Marceau, F., Pettibone, D. J. & Zuraw, B. L. International Union of Pharmacology. XLV. Classification of the Kinin Receptor Family: from Molecular Mechanisms to Pathophysiological Consequences. *Mol. Pharmacol.* **57,** 27–77 (2005).

80. Enquist, J., Skröder, C., Whistler, J. L. & Leeb-Lundberg, L. M. F. Kinins Promote B2 Receptor Endocytosis and Delay Constitutive B1 Receptor Endocytosis. *Mol. Pharmacol.* **71,** 494–507 (2007).

81. Guevara-Lora, I. Kinin-mediated inflammation in neurodegenerative disorders. *Neurochem. Int.* **61,** 72–78 (2012).

82. Wahl, M. *et al.* Vasomotor and permeability effects of bradykinin in the cerebral microcirculation. *Immunopharmacology* **33,** 257–263 (1996).

83. Prat, A. *et al.* Kinin B1 receptor expression and function on human brain endothelial cells. *J. Neuropathol. Exp. Neurol.* **59,** 896–906 (2000).

84. Sarker, M. H., Hu, D. E. & Fraser, P. A. Acute effects of bradykinin on cerebral microvascular permeability in the anaesthetized rat. *J. Physiol.* **528,** 177–187 (2000).

85. Su, J. *et al.* Blockade of bradykinin B2 receptor more effectively reduces postischemic blood–brain barrier disruption and cytokines release than B1 receptor inhibition. *Biochem. Biophys. Res. Commun.* **388,** 205–211 (2009).

86. Zhou, L. *et al.* Bradykinin regulates the expression of claudin-5 in brain microvascular endothelial cells via calcium-induced calcium release. *J. Neurosci. Res.* **92,** 597–606 (2014).

87. Fraser, P. A. The role of free radical generation in increasing cerebrovascular permeability. *Free Radic. Biol. Med.* **51,** 967–977 (2011).

88. Woodfin, A., Hu, D. E., Sarker, M., Kurokawa, T. & Fraser, P. Acute NADPH oxidase activation potentiates cerebrovascular permeability response to bradykinin in ischemia-reperfusion. *Free Radic. Biol. Med.* **50,** 518–524 (2011).

89. Raidoo, D. M. & Bhoola, K. D. Pathophysiology of the kallikrein-kinin system in mammalian nervous tissue. *Pharmacol. Ther.* **79,** 105–127 (1998).

90. Bhoola, K. D. & Overview, I. Bioregulation of Kinins: kallikreins, kininogens, and kininases. *Phamacological Rev.* **44,** 1–80 (1992).

91. Scicli, A. G., Forbes, G., Nolly, H., Dujovny, M. & Carretero, O. A. Kallikrein-kinins in the central nervous system. *Clin. Exp. Hypertens.* **6,** 1731–1738 (1984).

92. Kunz, M. *et al.* Bradykinin in Blood and Cerebrospinal Fluid after Acute Cerebral Lesions: Correlations with Cerebral Edema and Intracranial Pressure. *J. Neurotrauma* **30,** 1638–1644 (2013).

93. Raidoo, D. M. & Bhoola, K. D. Kinin receptors on human neurones. *J. Neuroimmunol.* **77,** 39–44 (1997).

94. Ongali, B. *et al.* Autoradiographic analysis of rat brain kinin B1 and B2 receptors: Normal distribution and alterations induced by epilepsy. *J. Comp. Neurol.* **461,** 506–519 (2003).

95. Raidoo, D. M. *et al.* Visualization of bradykinin B2 receptors on human brain neurons. *Immunopharmacology* **33,** 104–107 (1996).

96. Gimpl, G., Walz, W., Ohlemeyer, C. & Kettenmann, H. Bradykinin receptors in cultured astrocytes from neonatal rat brain are linked to physiological responses. *Neurosci. Lett.* **144,** 139–142 (1992).

97. Stephens, G. J., Cholewinski, A. J., Wilkin, G. P. & Djamgoz, M. B. A. Calcium-mobilizing and electrophysiological effects of bradykinin on cortical astrocyte subtypes in culture. *Glia* **9,** 269–279 (1993).

98. parpura, V; Basarsky, T. A.; Liu, F.; Jeftinija, K.; Jeftinija, S.; Haydon, P. G. Glutamate-mediated astrocyte-neuron signalling. *Nature* **369,** 744–747 (1994).

99. Rydh-Rinder, M., Kerekes, N., Svensson, M. & Hökfelt, T. Glutamate release from adult primary sensory neurons in culture is modulated by growth factors. *Regul. Pept.* **102,** 69–79 (2001).

100. Liu, H. T., Akita, T., Shimizu, T., Sabirov, R. Z. & Okada, Y. Bradykinin-induced astrocyte-neuron signalling: Glutamate release is mediated by ROS-activated volume-sensitive outwardly rectifying anion channels. *J. Physiol.* **587,** 2197–2209 (2009).

101. Yang, C. M. *et al.* Multiple factors from bradykinin-challenged astrocytes contribute to the neuronal apoptosis: Involvement of astroglial ROS, MMP-9, and HO-1/CO system. *Mol. Neurobiol.* **47,** 1020–1033 (2013).

102. Hsieh, H. L., Chi, P. L., Lin, C. C., Yang, C. C. & Yang, C. M. Up-regulation of ROS-Dependent Matrix Metalloproteinase-9 from High-Glucose-Challenged Astrocytes Contributes to the Neuronal Apoptosis. *Mol. Neurobiol.* **50,** 520–533 (2014).

103. Noda, M. *et al.* Neuroprotective role of bradykinin because of the attenuation of pro-inflammatory cytokine release from activated microglia. *J. Neurochem.* **101,** 397–410 (2007).

104. Wang, Q., Liu, Y. & Zhou, J. Neuroinflammation in Parkinson's disease and its potential as therapeutic target. *Transl. Neurodegener.* **4,** 1–9 (2015).

105. Gelders, G., Baekelandt, V. & Van der Perren, A. Linking Neuroinflammation and Neurodegeneration in Parkinson's Disease. *J. Immunol. Res.* **2018,** 1–12 (2018).

106. Baptiste A Faucheux, Anne-Marie Bonnet, Y. A. & Hirsch, E. C. Blood vessels change in the mesencephalon of patients with Parkinson's disease. *Lancet* **353,** 981–982 (1999).

107. Kortekaas, R. *et al.* Blood-brain barrier dysfunction in Parkinsonian midbrain in vivo. *Ann. Neurol.* **57,** 176–179 (2005).

108. Guan, J. *et al.* Vascular degeneration in parkinsons disease. *Brain Pathol.* **23,** 154–164 (2013).

109. Mogi, M. *et al.* Tumor necrosis factor-α (TNF-α) increases both in the brain and in the cerebrospinal fluid from parkinsonian patients. *Neurosci. Lett.* **165,** 208–210 (1994).

110. Mogi, M. *et al.* Interleukin (IL)-1β, IL-2, IL-4, IL-6 and transforming growth factor-α levels are elevated in ventricular cerebrospinal fluid in juvenile parkinsonism and Parkinson's disease. *Neurosci. Lett.* **211,** 13–16 (1996).

111. Brodacki, B. *et al.* Serum interleukin (IL-2, IL-10, IL-6, IL-4), TNFα, and INFγ concentrations are elevated in patients with atypical and idiopathic parkinsonism. *Neurosci. Lett.* **441,** 158–162 (2008).

112. McGeer, P. L., Itagaki, S., Boyes, B. E. & McGeer, E. G. Reactive microglia are positive for HLA-DR in the substantia nigra of Parkinson's and Alzheimer's disease brains. *Neurology* **38,** 1285 LP-1285 (1988).

113. Gerhard, A. *et al.* In vivo imaging of microglial activation with [11C](R)-PK11195 PET in idiopathic Parkinson's disease. *Neurobiol. Dis.* **21,** 404–412 (2006).

114. Bartels, A. L. *et al.* [11C]-PK11195 PET: Quantification of neuroinflammation and a monitor of anti-inflammatory treatment in Parkinson's disease? *Park. Relat. Disord.* **16,** 57–59 (2010).

115. Damier, P., Hirsch, E. C., Zhang, P., Agid, Y. & Javoy-Agid, F. Glutathione peroxidase, glial cells and Parkinson's disease. *Neuroscience* **52,** 1–6 (1993).

116. Braak, H., Sastre, M. & Del Tredici, K. Development of α-synuclein immunoreactive astrocytes in the forebrain parallels stages of intraneuronal pathology in sporadic Parkinson's disease. *Acta Neuropathol.* **114,** 231–241 (2007).

117. CHAO, J., CHAO, L. E. E., SWAIN, C. C., TSAI, J. & MARGOLIUS, H. S. Tissue Kallikrein in Rat Brain and Pituitary: Regional Distribution and Estrogen Induction in the Anterior Pituitary*. *Endocrinology* **120,** 475–482 (1987).

118. Raidoo, Deshandra M.; Ramsaroop, Reenadevi; Naidoo, Strini; Bhoola, K. D. Regional distribution of tissue kallikrein in the human brain. *Immunopharmacology* **3109,** (1996).

119. Hosli, Elisabeth; Hosli, L. Autoradiographic localization of binding sites for neuropeptide Y and bradykinin on astrocytes. 159–162 (1993).

120. Hosli, E., Kaeser, H. & Lefkovits, M. Colocalization of receptors for vasoactive peptides on astrocytes of cultured rat spinal cord and brain stem : electrophysiological effects of atrial and brain natriuretic peptide , neuropeptide Y and bradykinin. 114–116 (1992).

121. Simonato, M. *et al.* Induction of B1 Bradykinin Receptors in the Kindled Brain. in *Kindling 6* (eds. Corcoran, M. E. & Moshé, S. L.) 209–217 (Springer US, 2005).

122. Kariya, K., Yamauchi, A. & Sasaki, T. Regional Distribution and Characterization of Kinin in the CNS of the Rat. *J. Neurochem.* **44,** 1892–1897 (1985).

123. Perry, D. C. & Snyder, S. H. Identification of Bradykinin in Mammalian Brain. *J. Neurochem.* **43,** 1072–1080 (1984).

124. Gröger, M. *et al.* Release of bradykinin and expression of kinin B2 receptors in the brain: Role for cell death and brain edema formation after focal cerebral ischemia in mice. *J. Cereb. Blood Flow Metab.* **25,** 978–989 (2005).

125. Trabold, R. *et al.* The role of bradykinin B1 and B2 receptors for secondary brain damage after traumatic brain injury in mice. *J. Cereb. Blood Flow Metab.* **30,** 130–139 (2010).

126. Tian, L., Andrew Hires, S. & Looger, L. L. Imaging neuronal activity with genetically encoded calcium indicators. *Cold Spring Harb. Protoc.* **7,** 647–656 (2012).

127. Helassa, N., Podor, B., Fine, A. & Török, K. Design and mechanistic insight into ultrafast calcium indicators for monitoring intracellular calcium dynamics. *Sci. Rep.* **6,** 1–14 (2016).

128. Dana, H. *et al.* High-performance GFP-based calcium indicators for imaging activity in neuronal populations and microcompartments. *bioRxiv* 434589 (2018). doi:10.1101/434589

129. Chung, S. H., Sun, L. & Gabel, C. V. In vivo Neuronal Calcium Imaging in C. elegans. *J. Vis. Exp.* 1–9 (2013). doi:10.3791/50357

130. Xing, X. & Wu, C.-F. Unraveling Synaptic GCaMP Signals: Differential Excitability and Clearance Mechanisms Underlying Distinct Ca 2𝑐 Dynamics in Tonic and Phasic Excitatory, and Aminergic Modulatory Motor Terminals in Drosophila. **5,** 362–17 (2018).

131. Migault, G. *et al.* Whole-Brain Calcium Imaging during Physiological Vestibular Stimulation in Larval Zebrafish. *Curr. Biol.* 3723–3735 (2018). doi:10.1016/j.cub.2018.10.017

132. Tian, L. *et al.* Imaging neural activity in worms, flies and mice with improved GCaMP calcium indicators. *Nat. Methods* **6,** 875–881 (2009).

133. Heider, B., Nathanson, J. L., Isacoff, E. Y., Callaway, E. M. & Siegel, R. M. Two-photon imaging of calcium in virally transfected striate cortical neurons of behaving monkey. *PLoS One* **5,** 1–13 (2010).

CHAPTER 2. EXTENDING ROGFP EMISSION VIA FÖRSTER-TYPE RESONANCE ENERGY TRANSFER RELAY ENABLES SIMULTANEOUS DUAL COMPARTMENT RATIOMETRIC REDOX IMAGING IN LIVE CELLS

*This work has been published and is reproduced with permission from Norcross, S., Trull, K. J., Snaider, J., Doan, S., Kiet, T., Huang, L., Tantama, M. Extending roGFP Emission via Förster-Type Resonance Energy Transfer Relay Enables Simultaneous Dual Compartment Ratiometric Redox Imaging in Live Cells. *ACS Sensors* **2,** 1721–1729 (2017).

2.1 Abstract

Reactive oxygen species (ROS) mediate both intercellular and intraorganellar signaling, and ROS propagate oxidative stress between cellular compartments such as mitochondria and the cytosol. Each cellular compartment contains its own sources of ROS as well as antioxidant mechanisms, which contribute to dynamic fluctuations in ROS levels that occur during signaling, metabolism, and stress. However, the coupling of redox dynamics between cellular compartments has not been well studied because of the lack of available sensors to simultaneously measure more than one subcellular compartment in the same cell. Currently, the redox-sensitive green fluorescent protein, roGFP, has been used extensively to study compartment-specific redox dynamics because it provides a quantitative ratiometric readout and it is amenable to subcellular targeting as a genetically-encoded sensor. Here, we report a new family of genetically-encoded fluorescent protein sensors that extend the fluorescence emission of roGFP via Förster-type resonance energy transfer to an acceptor red fluorescent protein for dual-color live-cell microscopy. We characterize the redox and optical properties of the sensor proteins, and we demonstrate that they can be used to simultaneously measure cytosolic and mitochondrial ROS in living cells. Furthermore, we use these sensors to reveal cell-to-cell heterogeneity in redox coupling between the cytosol and mitochondria when neuroblastoma cells are exposed to reductive and metabolic stresses.

2.2 Introduction

Reduction-oxidation (redox) reactions must be kept in a careful balance in order to maintain healthy cell growth and function.[1–3] Loss of redox balance can lead to both reductive and oxidative stresses associated with aging, cancer, cardiovascular disease, and Parkinson's disease.[4–7] For example, reactive oxygen species (ROS), such as hydrogen peroxide (H_2O_2) and superoxide anion

($O2^{\bullet-}$), can oxidize protein-bound cysteines and other molecular species during normal metabolism and signaling.[8] However, excess ROS can cause oxidative stress and damage that leads to loss of function or cell death. To prevent such pathologies, redox enzymes and cellular redox buffers such as glutathione (GSH) are critical for maintaining proper redox balance. Together, both enzymatic and non-enzymatic components make up a "redox network"1 that contributes to homeostasis in the face of changing intracellular and environmental conditions faced by prokaryotes and eukaryotes.

Like metabolic and signaling networks, the redox network is spatially organized within a cell, and compartments such as the cytosol and mitochondria contain distinct sources of ROS as well as distinct antioxidant mechanisms involving redox enzymes and redox buffers.1 As a result, compartment-specific redox and ROS dynamics exist with varying degrees of cross-compartment coupling.[9–12] Redox coupling across compartments is a critical aspect of network response. For example, the production of mitochondrially-derived cytosolic ROS plays an integral role in retrograde mitonuclear communication and stress response.[13,14] However, compartment-specific ROS dynamics and redox signaling between organelles has been poorly studied because of the lack of spectrally-compatible redox probes that are available to simultaneously quantify redox in multiple compartments within the same living cell.

Currently, the redox-sensitive green fluorescent protein (roGFP) sensors are widely used to study redox biology across model species, including yeast, plants, and animals.[15–21] The roGFP sensors were originally developed by engineering two solvent-facing cysteines on the β-barrel of GFP.[18] Upon oxidation, the cysteines form a disulfide bond, causing a structural change that alters the protonation state of the internal chromophore. Redox state is reported as the ratio of the two peaks in the fluorescence excitation spectrum near 400 nm and 485 nm, in which oxidation causes an increase in the 400 nm peak and a decrease in the 485 nm peak. There are two versions of the sensor: the roGFP1 sensor is based on wildtype GFP in which the 400 nm peak is greater in absolute magnitude, and the roGFP2 sensor is based on GFP(S65T) in which the 485 nm peak is greater in absolute magnitude. The roGFP sensors are particularly useful because they can be genetically targeted to specific cell types and subcellular locations, including the cytosol and mitochondria. Furthermore, they provide ratiometric readouts that are independent of expression level and enable quantitative measurements that can be compared between independent experiments.

However, the roGFP-based sensors are solely green fluorescent, which makes accurate measurement of redox dynamics in multiple compartments within the same cell difficult or impossible. Recently, red fluorescent redox sensors, HyPerRed[22] and rxRFP[23], were engineered and can be used for dual-compartment, dual-color live-cell microscopy[24], but these sensors are not ratiometric, which can render quantitative analysis more challenging.

Therefore, in this work we describe the design, development, characterization, and validation of a first-generation family of roGFP-based sensors that exhibit long-wavelength emission via Förster-type resonance energy transfer (FRET) from a roGFP donor to a red fluorescent protein (RFP) acceptor. Importantly, we show that the redox properties of the parent roGFP donor are maintained when measuring the red emission of the roGFP-RFP sensors. We also report proof-of-principle studies that demonstrate that using multicolor imaging we can measure redox dynamics in the cytosol and mitochondria simultaneously within the same cell.

2.3 Materials and Methods

2.3.1 Materials

Chemicals and cell culture reagents were purchased from Sigma, Formedium, Qiagen, and ThermoFisher Scientific.

2.3.2 Molecular Biology

roGFP-RFP fusions were constructed using Gibson assembly in the pRSETB bacterial expression vector or the GW1 mammalian expression vector. Four copies of the COX8 mitochondrial signal sequence were appended in tandem to the N-terminus for mitochondrial targeting.[25] Plasmid constructs are distributed via Addgene.

2.3.3 Protein Expression and Purification

Polyhistidine-tagged protein was expressed in BL21(DE3) *E. coli* in Auto Induction Media (AIM) with continuous shaking at 37°C overnight and then at room temp for 48 hours. Cells were lysed and protein was purified by nickel affinity chromatography using a HiTrap™ Chelating HP column according to the manufacturer's instructions. Purified protein was dialyzed to remove

excess imidazole, snap frozen, and stored at -80°C until use. Protein lacking the polyhistidine tag was expressed in mammalian cells.

2.3.4 Steady-State Fluorescence Spectroscopy

Protein concentration was determined by denaturing in 1 M NaOH and measuring chromophore absorbance at 447 nm using an extinction coefficient of 44,000 $M^{-1}cm^{-1}$, accounting for the number of chromophores per construct. UV-vis and steady-state fluorescence spectroscopy was performed using a BioTek Synergy H4 microplate reader at room temperature. For all spectroscopy measurements protein was diluted to a final concentration of 1 µM in 75 mM HEPES, 125 mM KCl, 1 mM EDTA, pH 7.3, except in the redox titration experiments where the buffer pH was adjusted to 7.0. Solutions were degassed under vacuum for 10 minutes followed by flushing with argon gas, and the cycle was repeated three times in total. In general, diluted protein samples were equilibrated with reduced DTT (1, 4-Dithiothreitol) or oxidized DTT (trans-4,5-Dihydroxy-1,2-dithiane) under argon gas for 1 hour prior to measurements.

Fluorescence anisotropy was determined for samples oxidized with 10 mM oxidized DTT. A Semrock 510 nm single-edge dichroic beamsplitter was used (P/N: FF510-Di02-25x36) along with a 420/50 nm excitation filter and 528/20 nm or 620/40 nm emission filter. Redox titrations were performed by measuring the excitation spectra of protein diluted in solutions in which the ratio of reduced DTT to oxidized DTT was varied, keeping the total DTT concentration equal to 10 mM. Midpoint potentials (E'_o) were calculated as previously described.[18,20] Briefly, E'_{roGFP} was calculated assuming equilibrium between the sensor and DTT (E'_{DTT} = -323 mV).[26] The degree of sensor reduction was plotted against E'_{roGFP}, and midpoint potentials were then determined by fitting data to a Boltzmann function in Origin.

For the dynamic range measurements, proteins were diluted in 10 mM reduced DTT or 10 mM oxidized DTT in separate microcentrifuge tubes. For each reduced and oxidized sample, the F_{400nm}/F_{480nm} excitation ratio (R) was calculated, for the oxidized ($R_{Oxidized}$) and reduced ($R_{Reduced}$) states. The dynamic range was calculated as $R_{Oxidized}/R_{Reduced}$. Sensor spectral bleed-through was determined as the % FRET emission, exciting at 400 nm or 480 nm and collecting emission at the peak emission wavelengths of 592 nm, 600 nm, or 610 nm, relative to the single roGFPs and RFPs oxidized with 10 mM oxidized DTT.

2.3.5 Time-Resolved Fluorescence Spectroscopy

Fluorescence lifetimes were measured on a custom-built confocal microscope. Protein was diluted to a final concentration of 1 µM in 75 mM HEPES, 125 mM KCl, 1 mM EDTA, pH 7.3. Solutions were degassed under vacuum and purged with argon gas, and protein solutions were equilibrated with 10 mM oxidized DTT for 1 hour before measurements. Solution samples were placed in a 35 mm glass bottom dish (In Vitro Scientific, D35-20-1.5-N), and light was focused using a 20× objective with a coverslip correction ring at 0.17 mm (Olympus LUCPlanFL, NA = 0.45). Samples were excited with a 447 nm pulsed diode laser at a 10 MHz repetition rate (PicoQuant, LDH-P-C-450B). Donor roGFP emission was collected using a combination of 500 longpass and 550 shorpass filters. Lifetimes were measured using a single photon avalanche diode (Pico-Quant, PDM series) and a single photon counting module (Pico-Quant) with a time resolution of ~ 100 ps. Empirical mean lifetimes were measured directly from peak-to-tail because the instrument response function, ~150 ps full-width at half maximum, was far shorter than fluorescein standard and sensor lifetimes. Fluorescein standard lifetimes were in agreement with accepted values and measured before each experiment. FRET efficiency was calculated as $1 - \tau_{roGFP-RFP}/\tau_{roGFP}$.

2.3.6 Cell Culture and Transfections

Mouse neuroblastoma cells (Neuro2A) were cultured in Dulbecco's modified eagle's medium with 4.5 g/L glucose, 4 mM glutamine, 10% cosmic calf serum, 3.7 g/L sodium bicarbonate, pH 7.0-7.4. The cells were maintained at 37°C and 5% CO_2. One day prior to transfection approximately $2.5x10^5$ cells were plated into a 33 mm 6-well dish with 2 mL of media. Cells were transfected using Effectene (Qiagen) with 400 ng of DNA total (in co-transfections 200 ng of each construct was used) according to the manufacturer's instructions. One day post transfection cells were split at a ratio of 1:10 into a glass-bottom 12-well plate and imaged two days later.

2.3.7 Live-Cell Imaging

Neuro2A cells were imaged in imaging solution containing 15 mM HEPES, 120 mM NaCl, 3 mM KCl, 3 mM $NaHCO_3$, 1.25 mM NaH_2PO_4, 1 mM $MgCl_2$, 2 mM $CaCl_2$, and 10 mM glucose.

Cells were equilibrated at room temperature for at least one hour before all imaging experiments. NAC and rotenone/FCCP were diluted to 2X working stocks in imaging solution immediately prior to use. Equal volume additions were performed to ensure efficient mixing. H_2O_2 and DTT working stocks were prepared at 20X concentrations and used in the calibrations.

For widefield microscopy, cells were imaged in 12-well plates at a 6-minute interval on an Olympus IX83 using a Plan Apo VC 20X objective (0.75 NA) with a Prior motorized stage and an Andor Zyla 4.2 sCMOS camera (6.5 μm pixel) at 2x2 pixel binning with exposure times ranging from 50 to 200 millseconds. Lumencor light source using the following filter pairs (Semrock or Chroma): ex. 475/34nm, em. 525/50nm; ex. 395/25nm, em. 525/50nm, ex. 475/34nm, em. 632/60nm, ex. 395/25nm, em. 632/60nm, ex. 575/25nm, em. 632/60nm. DIC images were taken before and after each imaging experiment to verify cell health.

Confocal microscopy was carried out in the Purdue Life Sciences Imaging Facility on a Nikon A1R confocal laser scanning microscope with a Plan Apo VC 60X oil DIC N2 objective (1.4 NA), pinhole size 26.82 μm. Laser excitation at 488 nm or 561 nm was used with a 405nm/488nm/561nm/640nm multiband dichroic mirror and 525/50nm or 595/50nm emission filters. Images were acquired using a Galvano scanner at 30 fps, and collected on an A1-DU4, 4 detector unit with 4 normal PMTs, pixel size 0.41, 0.41, 0.5 μm (x,y,z).

2.3.8 Data Analysis

Images were analyzed using ImageJ as previously described.[25] First, a threshold mask was applied to reject background pixels. To generate the threshold mask, five background regions of interest (ROIs) were drawn to obtain an average background for the cytosolic green fluorescence channels for each image. After background subtraction, fluorescent pixels were identified with a mask that was generated using a minimum threshold set at three times the original background standard deviation. Masks were generated for both the 395nm/525nm and 475/525nm green channels for each image. Then, for each image the Boolean "AND" function was applied to the two channels to generate a final mask that included pixels present in both channels above background. The final mask was applied to the background subtracted images in order to reject background pixels. A second threshold mask was next created and applied to isolate mitochondria. The same threshold masking procedure described above was carried out for the single direct RFP acceptor 575nm/632nm channel for each image. This generated a mitochondrial mask, which was

then applied to the 395nm/632nm and 476nm/632nm FRET channels. Lastly, the mitochondrial mask was then inverted and applied to the 395nm/525nm and 475/525nm cytosolic green fluorescence channels in order to remove pixels that contained significant contributions from the residual roGFP donor green fluorescence in mitochondria.

Cellular ROIs were manually selected and analyzed for the mitochondrial images in the FRET channels or for the cytosolic images in the green fluorescence channels. Ratio signals were measured from pixel-by-pixel ratio images obtained by frame-by-frame stack division in ImageJ. The fraction of oxidized sensor was calculated according to the equation $Y_{oxidized}$ = (Ratio - $Ratio_{reduced}$) / [($F_{475,oxidized}$ / $F_{395,oxidized}$)·($Ratio_{oxidized}$ - Ratio) + (Ratio - $Ratio_{reduced}$)] where Ratio = F_{395}/F_{475}, $Ratio_{oxidized}$ = Ratio of the fully oxidized sensor obtained during the H_2O_2 calibration step, $Ratio_{reduced}$ = Ratio of the fully reduced sensor obtained during the DTT calibration step, and %oxidized = 100% · $Y_{oxidized}$. The pH-corrected potential was calculated according to the equation $E_0'(pH) = E_{roGFP}^{0'} - (RT/nF)\cdot\ln[(1-Y_{oxidized}) / Y_{oxidized})] - (0.0601\ V)\cdot(pH - 7)$ where it was assumed the cytosolic pH = 7.2 and mitochondrial matrix pH = 8.0 from literature reports[27,28] and in which $E_{roGFP}^{0'}$ is the midpoint potential of roGFP1 (-0.287 V) or roGFP2 (-0.274 V) measured in this work.

2.4 Results and Discussion

2.4.1 Sensor Design

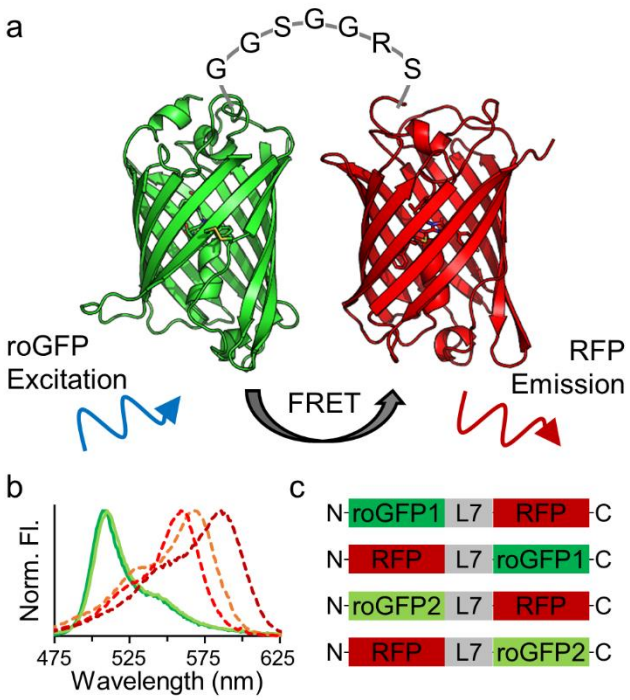

Figure 2.1 Design of the roGFP-RFP sensor library.

(A) Diagram of the FRET relay from the roGFP donor to the RFP acceptor. (B) Fluorescence spectra showing roGFP (solid, green) emission and RFP excitation (dashed, left-to-right: mRuby2, mApple, mCherry). (C) Diagram of the N- versus C-terminal fusions tested in this work, in which L7 indicates the GGSGGRS linker.

Our sensor design employs a FRET "relay" strategy in which the roGFP serves as a redox-sensing donor that is fused to an RFP acceptor (Figure 2.1).[29–32] Excitation of the roGFP at any wavelength in its excitation spectrum will result in red fluorescence from the RFP while preserving both redox sensing properties and a ratiometric readout. In principle, the roGFP-RFP red emission will be spectrally distinct and enable dual color imaging by coexpressing both roGFP and roGFP-RFP in the same cell. This FRET relay strategy has been demonstrated with both CFP-YFP as well as GFP-RFP fusions engineered for high efficiency FRET, and this relay strategy has been used to overcome autofluorescence in live-cell imaging.[29–32] It is important to note that FRET between the roGFP donor and RFP acceptor is designed to be constant in this strategy, and the ratiometric redox

sensing originates solely from the change in the roGFP excitation spectrum. Thus, our design is fundamentally different from sensors that report redox changes by a change in FRET.[33,34]

To implement our design, we first generated a library of 12 roGFP-RFP fusions to identify constructs that provide red emission via our FRET relay strategy. FRET efficiency depends on the distance, orientation, and spectral overlap between the donor and acceptor fluorescent proteins.[35] Therefore, we considered four main variables in our library design: the roGFP choice, the fusion linker, the RFP choice, and the orientation of the fusion. We included both roGFP1 and roGFP2 as possible donors in our library because they have similar redox sensing capabilities and provide ratiometric readouts.[18] Although the roGFP2 sensor is more commonly used, the roGFP1 sensor can be beneficial for live-cell imaging because of its greater brightness when excited at 400 nm. For the fusion linker, we used a short seven amino acid linker (GGSGGRS) that has previously been used for high efficiency FRET between fluorescent proteins.[36] For the acceptor, we included the RFPs mRuby2, mApple, and mCherry (Figure 2.1).[37–39] The mRuby2 acceptor provides the greatest spectral overlap between the roGFP green emission and its absorbance, and it has been used as a FRET acceptor for the GFP Clover.[37] The mCherry acceptor provides the greatest spectral separation between the green and red emission profiles, and it has been used in FRET pairs with GFPs both in vitro and in vivo.[40] We included mApple as an acceptor with intermediate spectral profile and high brightness.[38] Finally, we also included constructs in which the RFP acceptor was fused to either the N- or C-terminus of the roGFP donor (Figure 2.1).

2.4.2 Library Screen and Characterization of Constructs as Purified Protein in Solution

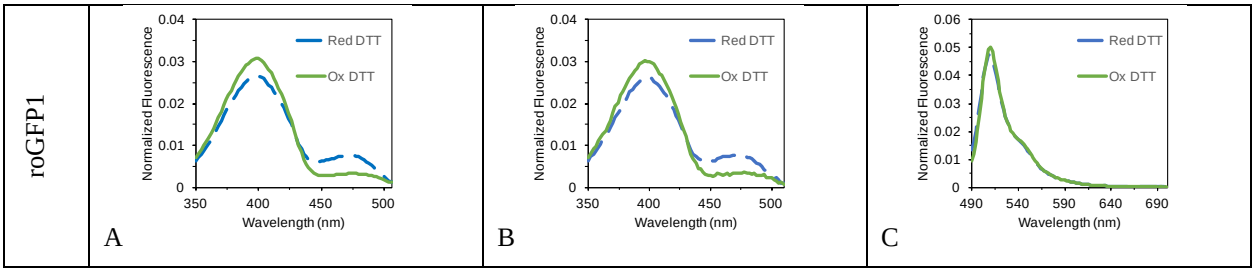

Figure 2.2 Fluorescence spectra of all roGFP1 sensor constructs.

(A) Excitation spectra collecting green donor emission, (B) excitation spectra collecting red acceptor emission and (C) emission spectra exciting at the isosbestic point.

Figure 2.2 Continued

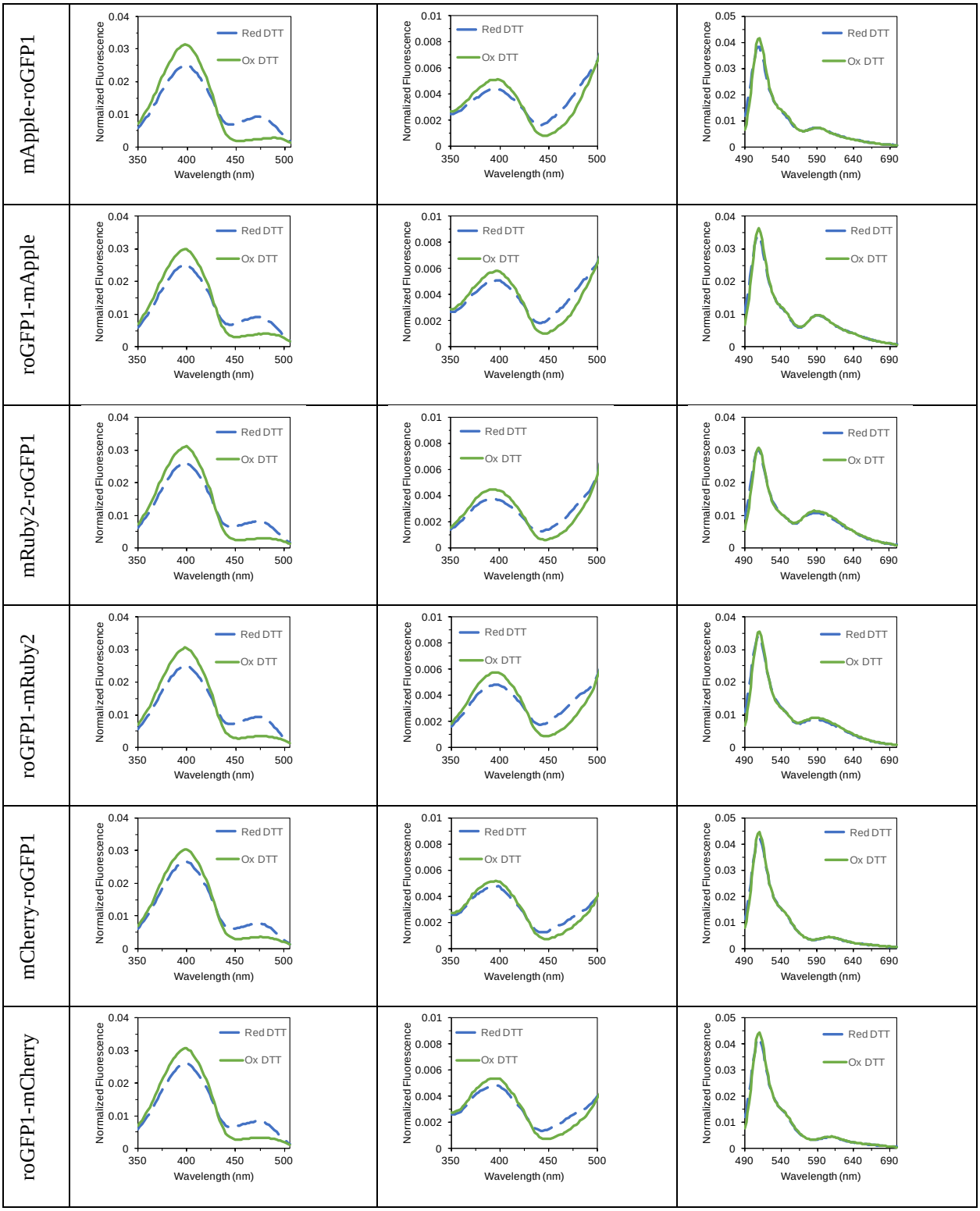

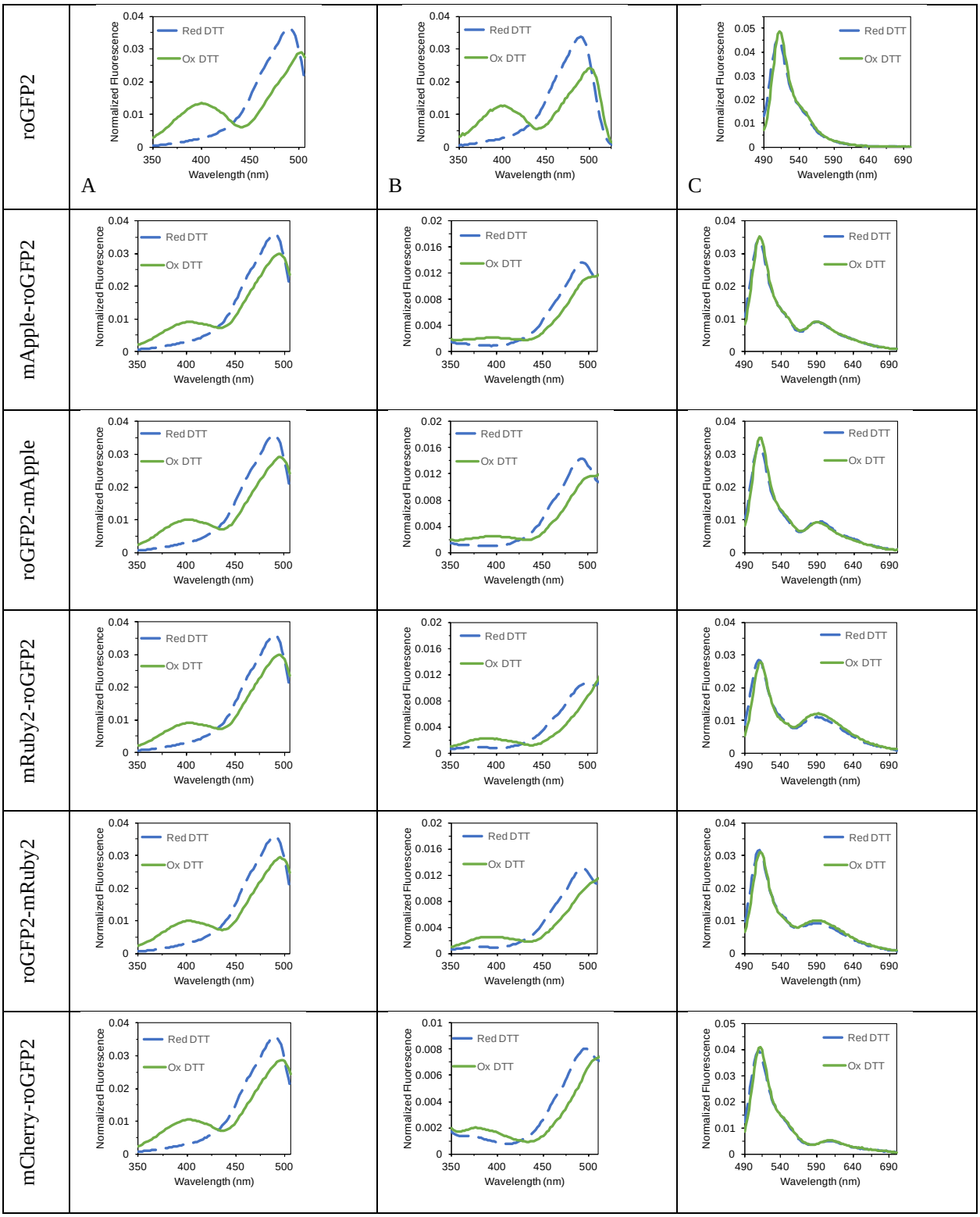

Figure 2.3 Fluorescence spectra of all roGFP2 sensor constructs.

(A) Excitation spectra collecting green donor emission, (B) excitation spectra collecting red acceptor emission and (C) emission spectra exciting at the isosbestic point.

Figure 2.3 Continued

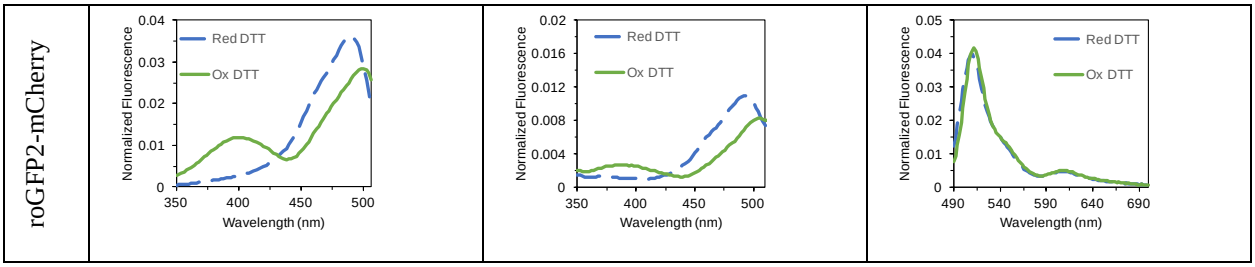

Table 2.1 Spectral bleed-through (mean ± stdev)

Construct	400 nm Bleed-Through (%)	480 nm Bleed-Through (%)
mApple-roGFP1, roGFP1-mApple	6.8 ± 0.1	14.3 ± 0.7
mRuby2-roGFP1, roGFP1-mRuby2	4.82 ± 0.07	10 ± 1
mCherry-roGFP1, roGFP1-mCherry	7.3 ± 0.9	7.3 ± 0.9
mApple-roGFP2, roGFP2-mApple	6.9 ± 0.1	13.1 ± 0.2
mRuby2-roGFP2, roGFP2-mRuby2	4.7 ± 0.2	9.3 ± 0.1
mCherry-roGFP2, roGFP2-mCherry	4.06 ± 0.09	6.65 ± 0.07

In order to select the best performing fusion constructs, we screened our library using steady-state and time-resolved fluorescence measurements of the purified proteins in solution. We first qualitatively screened our 12 constructs by measuring emission spectra and fluorescence anisotropy. We discovered that all 12 roGFP-RFP fusion constructs exhibit a clear red fluorescence FRET emission peak upon donor excitation (Figures 2.2, 2.3). Although there is substantial residual green emission, the red emission peak is distinct and well above background (Table 2.1). Furthermore, FRET is expected to cause depolarization of the red emission and thus a decrease in anisotropy. Indeed, all constructs also exhibit a large decrease in fluorescence anisotropy in the red emission channel upon donor excitation, despite the increase in overall protein size (Table 2.2). Thus, significant FRET occurs in all 12 constructs.

Table 2.2 Steady-state and time-resolved fluorescence characterization of roGFP-RFP library (n = 3 ± stdev).

Construct	Anisotropy	Ratio(Ox) / Ratio(Red)	Donor Lifetime (ps)	FRET Efficiency
roGFP1	0.270 ± 0.001	2.61 ± 0.02	3145 ± 2	N/A
mApple-L7-roGFP1	0.047 ± 0.002	1.62 ± 0.04	2370 ± 10	0.247 ± 0.006
roGFP1-L7-mApple	-0.028 ± 0.001	1.51 ± 0.02	2175 ± 5	0.308 ± 0.003 *
mRuby2-L7-roGFP1	0.107 ± 0.001	1.63 ± 0.01	2140 ± 30	0.32 ± 0.01 *
roGFP1-L7-mRuby2	0.0660 ± 0.003	1.75 ± 0.01	2360 ± 20	0.249 ± 0.007
mCherry-L7-roGFP1	0.04 ± 0.02	1.44 ± 0.03	2280 ± 1	0.275 ± 0.001
roGFP1-L7-mCherry	0.03 ± 0.02	1.63 ± 0.04	2290 ± 20	0.273 ± 0.008
roGFP2	0.270 ± 0.001	8.07 ± 0.01	2905 ± 5	N/A
mApple-L7-roGFP2	0.022 ± 0.002	3.22 ± 0.03	2085 ± 2	0.282 ± 0.002
roGFP2-L7-mApple	-0.0132 ± 0.0008	3.66 ± 0.07	2074 ± 5	0.286 ± 0.003
mRuby2-L7-roGFP2	0.126 ± 0.001	4.86 ± 0.04	2130 ± 30	0.27 ± 0.01
roGFP2-L7-mRuby2	0.0698 ± 0.007	4.15 ± 0.07	2180 ± 20	0.248 ± 0.008
mCherry-L7-roGFP2	0.053 ± 0.002	2.92 ± 0.03	1986 ± 4	0.316 ± 0.003 *
roGFP2-L7-mCherry	0.018 ± 0.002	4.456 ± 0.008	2062 ± 2	0.290 ± 0.002

* Three highest FRET efficiency constructs chosen for in-depth characterization.

We next assessed whether the constructs preserve redox sensing by measuring the steady-state fluorescence excitation spectra in the presence of excess reduced or oxidized dithiothreitol (10 mM DTT). Purified proteins of all 12 constructs exhibit a redox-dependent ratiometric change in the excitation spectrum when collecting either direct donor roGFP green fluorescence emission or FRET acceptor red fluorescence emission (Figures 2.2, 2.3), we quantified the excitation ratios for the FRET acceptor red fluorescence emission channel (ratio = F_{400nm}/F_{485nm}) in the oxidized and reduced states, and we measured the dynamic range as the maximal fold change in ratio signal upon oxidation (dynamic range = $ratio_{oxidized}/ratio_{reduced}$) (Table 2.2). Compared to the roGFP1 and roGFP2 parent sensors, the roGFP-RFP fusion constructs exhibit on average a 40% and 50% reduction in dynamic ranges. The attenuation in the dynamic ranges is a consequence of spectral cross-talk, and the primary contribution comes from the direct excitation of the RFP acceptor when exciting at 490 nm (Table 2.1). Despite the attenuation in dynamic range, all constructs exhibit clear preservation of redox sensing as well as a ratiometric response of the same magnitude as other sensors that have proven useful in live-cell imaging.[19,20,37]

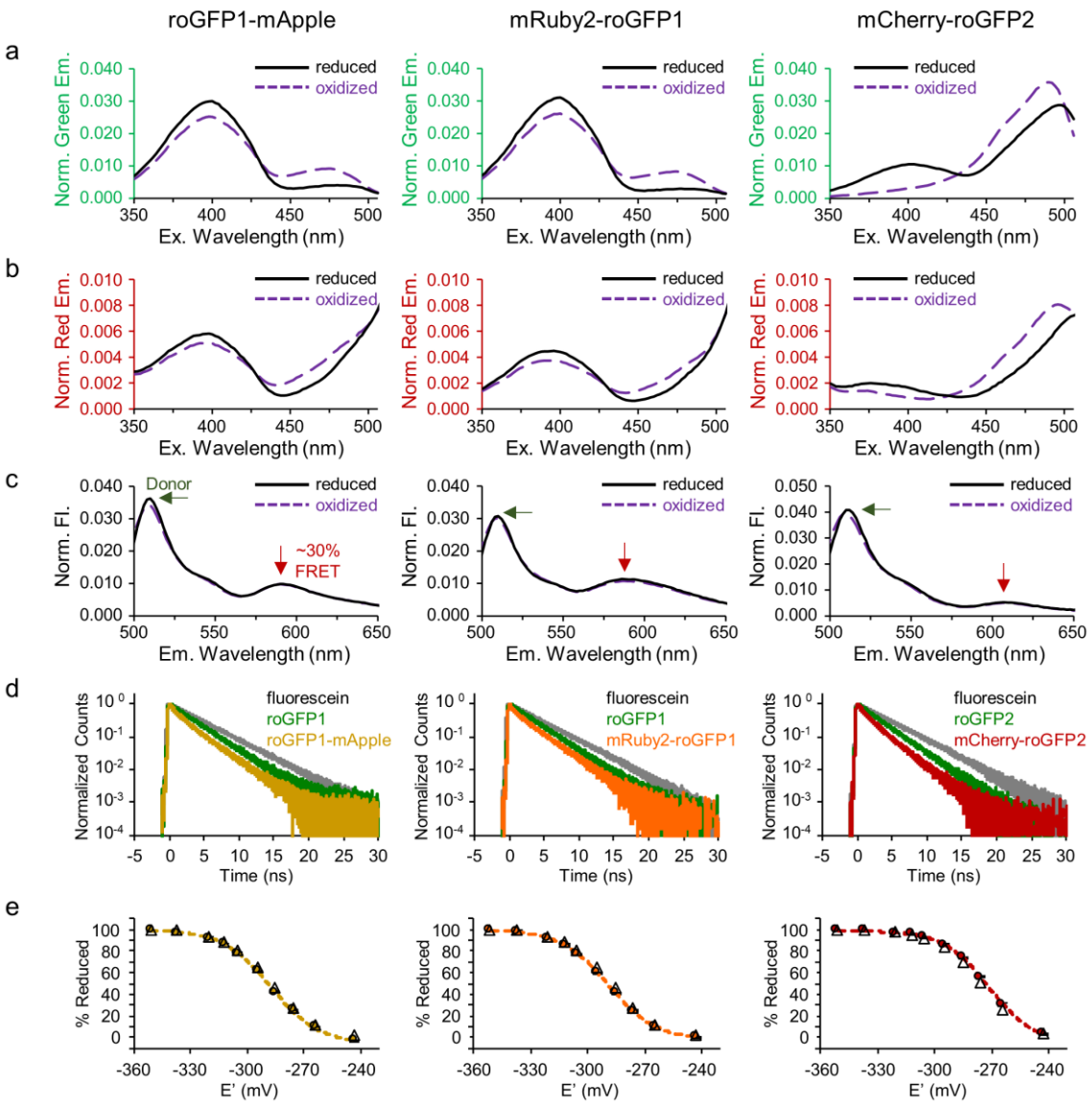

Figure 2.4 Characterization of steady-state and time-resolved fluorescence properties of the highest FRET efficiency roGFP-RFP constructs.

(a-b) Redox-dependent ratiometric changes in the fluorescence excitation spectra when collecting (a) residual roGFP donor green emission and (b) RFP emission via FRET. (c) Fluorescence emission spectra show the residual roGFP donor (green arrow) and RFP FRET acceptor emission peaks (red arrow). (d) The roGFP-RFP constructs exhibit a decreased donor fluorescence lifetime, which is used to quantify FRET efficiency. (e) The roGFP-RFP constructs (circles, measured; dashed line, fitted) preserve redox sensing and exhibit similar DTT reduction potentials relative to the parent roGFP (triangles, measured).

In order to quantitatively compare FRET efficiencies of the 12 constructs, we measured donor fluorescence lifetimes, which decrease with increasing FRET efficiency. As expected, the

purified proteins of all the roGFP-RFP constructs exhibit reduced donor fluorescence lifetimes relative to the roGFP1 and roGFP2 parent sensors, indicating FRET efficiencies from 25 to 32% (Table 2.2). We therefore selected three constructs with the highest FRET efficiencies, roGFP1-mApple, mRuby2- roGFP1, and mCherry-roGFP2, for further characterization of their redox sensing properties (Figure 2.4).

To determine if the redox properties of the parent roGFP are preserved in these three selected fusion constructs, we carried out redox titrations against increasing ratios of oxidized-to-reduced DTT. We determined that the midpoint potentials of roGFP1-mApple (−287.1 ± 0.4 mV) and mRuby2-roGFP1 (−288.7 ± 0.8 mV), measured in both direct donor green fluorescence and FRET acceptor red fluorescence channels, are in agreement with the midpoint potential of the parent roGFP1 measured in this work (−287.4 ± 0.7 mV) and as originally reported by Hanson and co-workers using the same method (−288 mV).[15,18] Likewise, we also determined that the midpoint potential of mCherry-roGFP2 (−272 ± 1 mV) is in agreement with the midpoint potential of the parent roGFP2 measured in this work (−274.4 ± 0.5 mV) and as originally reported (−272 mV).[15,18] Thus, our results confirm that our FRET relay constructs preserve the original redox properties of the parent roGFP and provide an excitation ratiometric response when measuring the FRET acceptor red fluorescence emission (n = 3, mean ± SD).

With ∼30% FRET efficiency, the roGFP-RFP constructs generate significant red fluorescence signal, but there is still a substantial amount of residual green fluorescence from the donor. The remaining spectral overlap precludes the use of both the parent roGFP and these first-generation roGFP-RFP sensors within the same cellular compartment. However, despite the residual green donor emission, we hypothesized that the roGFP-RFP fluorescence could be spatially separated from the roGFP fluorescence by targeting the roGFP-RFP sensors to a subcellular location. Thus, in order to validate the function of the roGFP1-mApple, mRuby2-roGFP1, and mCherry-roGFP2 constructs for dual-color imaging, we next measured mitochondrial and cytosolic redox potentials simultaneously within the same cells.

2.4.3 Cytosolic and Mitochondrial Redox Potential

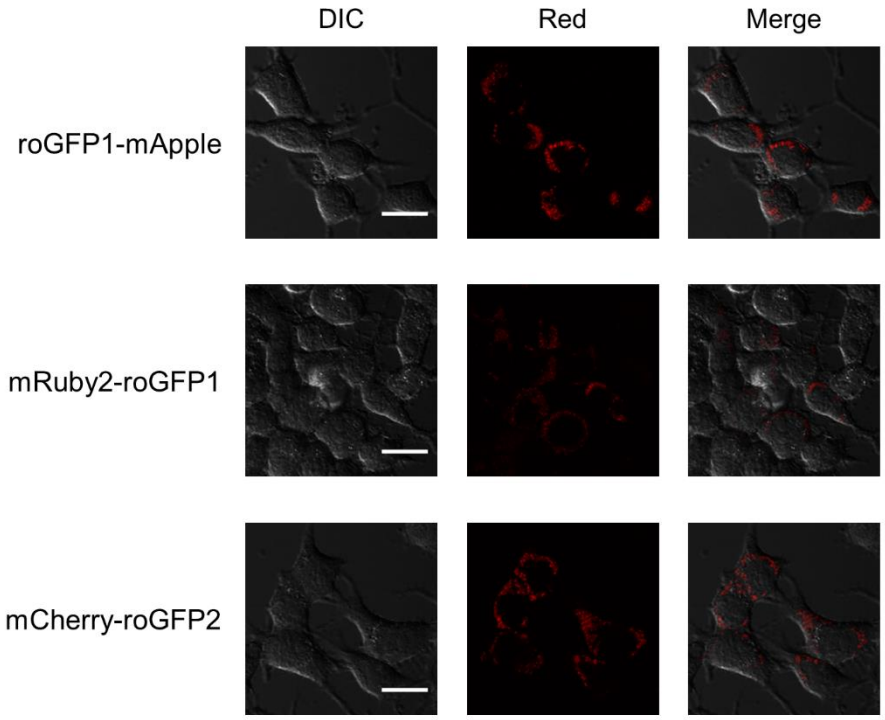

Figure 2.5 Confocal images show excellent subcellular localization for mito-roGFP-RFP constructs, targeted with the COX8 mitochondrial localization signal.

We previously observed[25] that undifferentiated Neuro2A cells exhibit large nuclei, causing the perinuclear appearance of the mitochondria, which are also rounded under high glucose conditions. In this study, we observe similar morphology in which the mito-roGFP1-mApple, mito-mRuby2-roGFP1, and mitomCherry-roGFP2 sensors target to the mitochondria well. Scale bar = 20 μM.

When Neuro2A mouse neuroblastoma cells were cotransfected pairwise with a mitochondrially targeted roGFP-RFP fusion and its respective parent roGFP for cytosolic expression, we found that the red and green fluorescence signals were spectrally and spatially separated as hypothesized. The mito-roGFP-RFP fusions were targeted to the mitochondrial matrix by appending the signal sequence from cytochrome c oxidase subunit VIII (Cox8), which we and others have previously employed, and we observed excellent subcellular localization to mitochondria using confocal microscopy, as expected (Figure 2.5).[25]

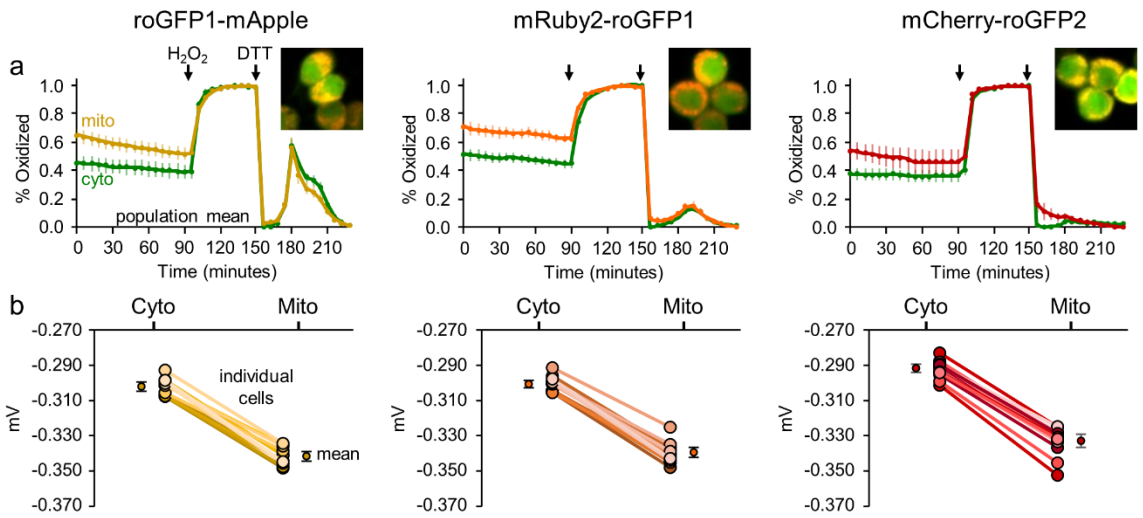

Figure 2.6 Simultaneous measurement of cytosolic and mitochondrial matrix redox potentials by the coexpression of cyto-roGFP and mito-roGFP-RFP in Neuro2A cells.

(a) Mean response of the cell populations during the imaging time course (roGFP1-mApple, n = 12 cells; mRuby2-roGFP1, n = 14 cells; mCherry-roGFP2, n = 15; errors are 95% confidence intervals). A baseline measurement period is followed by treatment with excess H_2O_2 and DTT (arrows) in order to calibrate the fully oxidized and fully reduced states of the sensor. The calibration is used to determine the sensor percent oxidation on a cell-by-cell basis for every experiment. (b) Single-cell analysis of compartment-specific redox potentials. Lines connect cytosolic and mitochondrial redox potentials for individual cells. Mean ± SEM is shown for the population.

Next, ratiometric imaging was carried out using widefield microscopy with sequential collection of green and red emission, in which the red emission was localized to mitochondria (Figure 2.6). The red emission was also used to generate a mitochondrial mask during image analysis in order to isolate mitochondrial and cytosolic signals, minimizing mixing of the residual roGFP-RFP donor emission with the cytosolic roGFP signal. To measure redox potentials, we carried out baseline ratio measurements followed by a sensor calibration as previously described.[15,18,20] In the calibration, sensors were fully oxidized by the addition of 1 mM H_2O_2 to the imaging solution followed by full reduction with 10 mM DTT, and the calibration values were used to calculate the percent oxidation of the respective sensors (Figures 2.6).[15,18,20] As expected from previous reports, the mitochondrially targeted sensors on average are more oxidized than the cytosolic sensors because of the alkaline pH of the mitochondrial matrix.[15,18,20] Taking compartment-specific pH into account (assuming cytosolic pH = 7.2 and mitochondrial matrix pH = 8.0),[27,28] our average measurements of the cytosolic and mitochondrial redox potential, −298 ±

6 mV and −338 ± 5 mV (mean ± SD) respectively, agree well with previously reported values (Figure 2.6).[15,18,20] Importantly, our approach enables the direct comparison of the average mitochondrial and cytosolic redox potentials within the same cell. We discovered that mitochondrial redox potential is set −40 mV relative to cytosolic redox potential, which was highly consistent across independent cells and sensor pairings (Figure 2.6). Thus, our roGFP-RFP FRET relay redox sensors enable steady-state differences in redox potential between subcellular compartments to be quantified. We next tested whether our new sensors could also quantify differences in subcellular redox dynamics.

2.4.4 Heterogeneous Response to Cytosolic Reductive Stress

We found that our dual-compartment imaging approach was able to reveal cell-to-cell population heterogeneity in compartment-specific responses to cytosolic reductive stress induced by exposure to excess N-acetylcysteine (NAC). In our initial redox studies (Figure 2.6), we observed that the Neuro2A cells exhibited an oxidative rebound following DTT addition during the final calibration phase, which indicates that Neuro2A cells respond to reductive stress. It has previously been observed that reductive stress causes a paradoxical oxidative response in HEK293, H9c2, and other cell types.[41–43] NAC is a cell-permeant reductant that increases the levels of cytosolic reduced glutathione, but NAC is mitochondrially impermeant.[41,43] Interestingly, NAC-induced reductive stress causes an oxidative response in mitochondria but not the cytosol.[41,43] However, the compartment-specific difference in redox dynamics was determined by comparing population averages from cells separately transfected with cytosolic or mitochondrial roGFP-based probes, and therefore open questions remain regarding whether a difference in compartment-specific responses actually exists within a single cell and whether there is variability from cell-to-cell.

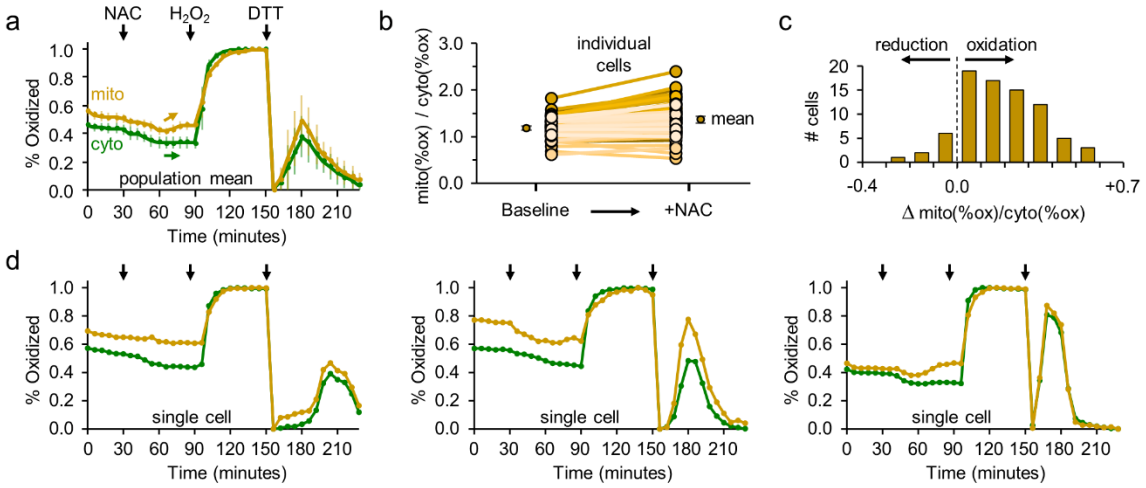

Figure 2.7 Single-cell heterogeneity in compartment-specific redox dynamics is observed in response to reductive stress when Neuro2A cells are treated with 6 mM N-acetylcysteine (NAC).

(a) Mean compartment-specific time-course responses of the cell populations (n = 80 cells, errors are 95% confidence intervals.). On average, Neuro2A cells coexpressing mito-roGFP1-mApple (yellow) and cyto-roGFP1 (green) exhibit an oxidative rebound in the mitochondria (yellow arrow) that is not observed in the cytosol (green arrow). (b–d) Single-cell analysis reveals population heterogeneity in the compartment-specific response to NAC. (b) The ratio of mitochondrial sensor oxidation to cytosolic sensor oxidation quantifies the variability in the mitochondrial redox change relative to the cytosol at the single-cell level. Lines show responses for individual cells, and the population mean ± SEM is shown. (c) Cell count histogram shows the heterogeneity in the magnitude of the single-cell responses. (d) Examples of single-cell responses.

To answer this question, we used our dual-compartment imaging approach. After a baseline measurement period, Neuro2A cells expressing mitochondrial roGFP1-mApple and cytosolic roGFP1 were exposed to 6 mM NAC[41,43] followed by cell-by-cell sensor calibration with H_2O_2 and DTT after every experiment (Figure 2.7). At the level of the population average, we observed that both the cytosol and mitochondrial matrix experienced an initial reduction in redox potential upon addition of NAC; however, a small oxidative rebound was observed in the mitochondria after several minutes, which was absent in the cytosol (Figure 2.7). Our population measurement is in agreement with the previous population measurements, and the smaller magnitude of the oxidative rebound likely reflects cell-type differences.[41,43] Furthermore, our measurements also reveal a reductant-specific difference in the stress response because, while NAC-induced stress causes an oxidative rebound in mitochondria only, DTT-induced stress causes an oxidative rebound in both the cytosol and the mitochondria. Importantly, our dual-compartment imaging approach revealed heterogeneous responses at the single-cell level.

2.4.5 Heterogeneous Response to Mitochondrial Inhibition

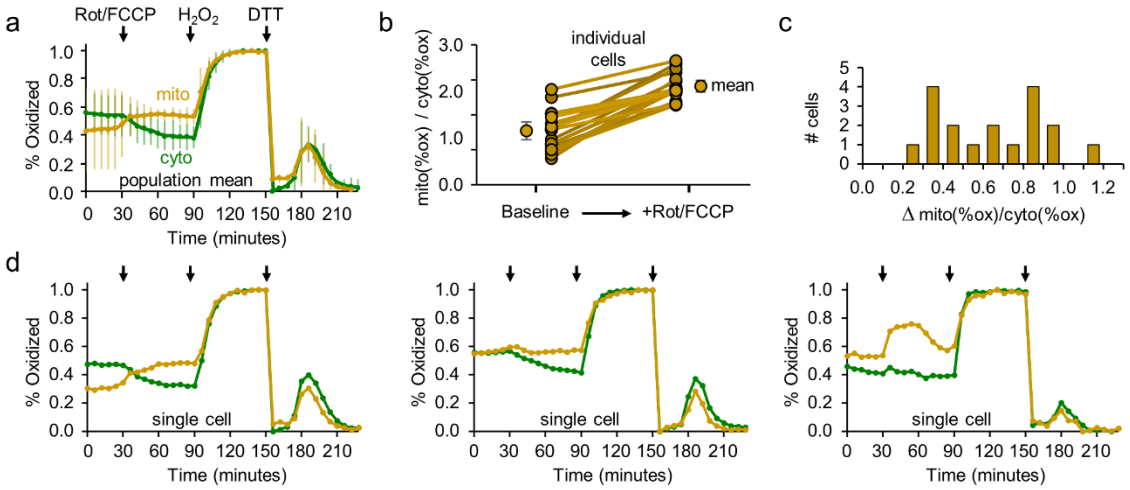

Figure 2.8 Single-cell heterogeneity in compartment-specific redox dynamics observed in response to metabolic stress when Neuro2A cells are treated with mitochondrial inhibitors (rot/FCCP: 2 μM rotenone and 2 μM FCCP) under low glucose conditions.

(a) Mean compartment-specific time- course responses of the cell populations (n = 18 cells, errors are 95% confidence intervals). On average, Neuro2A cells coexpressing mito-roGFP1-mApple (yellow) and cyto-roGFP1 (green) exhibit mitochondrial oxidation and cytosolic reduction in response to mitochondrial inhibition. (b−d) Single-cell analysis reveals significant heterogeneity in the extent to which mitochondria oxidize relative to the cytosol in individual cells. (b) The ratio of mitochondrial sensor oxidation to cytosolic sensor oxidation quantifies the variability in the mitochondrial redox change relative to the cytosol at the single-cell level. Lines show responses for individual cells, and the population mean ±SEM is shown. (c) Cell count histogram shows the the heterogeneity in the magnitude of the single-cell responses. (d) Examples of single-cell responses.

Lastly, we tested whether our dual-compartment imaging approach could reveal cell-to-cell population heterogeneity in compartment-specific responses to mitochondrial inhibition. The mitochondrial electron transport chain is a major source of both mitochondrial and cytosolic ROS. Inhibition of electron transport is expected to cause a decrease in ROS production, but low dose treatment with transport inhibitors or proton uncouplers can also cause an increase in ROS.[41,44,45] However, there remains an open question to what extent mitochondrial and cytosolic redox dynamics are coupled in the face of mitochondrial inhibition. To answer this question Neuro2A cells expressing roGFP1-mApple in mitochondria and roGFP1 in the cytosol were grown in low glucose media in order to increase mitochondrial respiration prior to imaging.[46] During imaging, mitochondrial inhibition was induced with the complex I inhibitor rotenone and the uncoupling

protonophore carbonyl cyanide 4-(trifluoromethoxy)-phenylhydrazone (FCCP) (Figure 2.8). At the level of the population average, we observed a trend suggesting that mitochondrial inhibition causes cytosolic reduction and mitochondrial oxidation (Figure 2.8). Importantly, our dual compartment imaging approached revealed cell-to-cell variation in the magnitude of mitochondrial oxidation relative to cytosolic reduction, and it also revealed that at the single-cell level complex compartment-specific dynamics can occur in response to mitochondrial inhibition (Figure 2.8). The heterogeneity may reflect cell-specific differences in respiratory efficiency as well as variability in redox buffer capacity in the face of metabolic inhibition. Overall, these results demonstrate that our roGFP-RFP FRET relay redox sensors can quantify how mitochondrial stress alters cytosolic redox dynamics at the single-cell level.

2.5 Conclusion

In this work, we developed a first-generation family of genetically encoded redox sensors that exhibit an excitation-ratiometric red fluorescence readout, and we demonstrated their utility in dual-color, dual-compartment live-cell imaging. These roGFP-RFP sensors utilize a FRET relay strategy to extend the emission spectrum of the donor roGFP out to red fluorescence wavelengths, and they preserve the redox sensing properties of the donor roGFP sensors. However, these first-generation sensors exhibit modest FRET efficiencies of approximately 30%, and they suffer from residual donor green fluorescence. Future optimization of the linker length could improve the FRET efficiency, but currently the residual donor emission leads to a spectral mixing problem that precludes the use of the roGFP-RFP sensors with other green fluorescence sensors if they are expressed in the same compartment. To circumvent this problem, we targeted the roGFP-RFP sensors to mitochondria and roGFP sensors to the cytosol, and spatial localization allowed us to measure cytosolic and mitochondrial redox potentials simultaneously within the same cell for the first time to our knowledge. Thus, these sensors are advantageous for quantifying subcellular redox potentials because they can be targeted to organelles, they exhibit an emission profile that is spectrally distinct from green fluorescent redox sensors, and they preserve the redox sensing properties of the roGFP sensors. Our results also demonstrate that our FRET relay strategy can in principle be used to extend the fluorescence emission of other green fluorescent sensors of redox or other analytes into red wavelengths for multiparameter imaging studies.

2.6 References

1. Sies, H., Berndt, C. & Jones, D. P. Oxidative Stress. *Annu. Rev. Biochem.* **86,** 715–748 (2017).

2. Dickinson, B. C. & Chang, C. J. Chemistry and biology of reactive oxygen species in signaling or stress responses. *Nat. Chem. Biol.* **7,** 504–511 (2011).

3. Schieber, M. & Chandel, N. S. ROS Function in Redox Signaling and Oxidative Stress. *Curr. Biol.* **24,** R453–R462 (2014).

4. Gorrini, C., Harris, I. S. & Mak, T. W. Modulation of oxidative stress as an anticancer strategy. *Nat. Rev. Drug Discov.* **12,** 931–947 (2013).

5. Griendling, K. K. *et al.* Measurement of Reactive Oxygen Species, Reactive Nitrogen Species, and Redox-Dependent Signaling in the Cardiovascular System. *Circ. Res.* **119,** e39–e75 (2016).

6. Brewer, A. C., Mustafi, S. B., Murray, T. V. A., Rajasekaran, N. S. & Benjamin, I. J. Reductive stress linked to small HSPs, G6PD, and Nrf2 pathways in heart disease. *Antioxid. Redox Signal.* **18,** 1114–27 (2013).

7. Surmeier, D. J., Guzman, J. N., Sanchez, J. & Schumacker, P. T. Physiological Phenotype and Vulnerability in Parkinson's Disease. *Cold Spring Harb. Perspect. Med.* **2,** a009290–a009290 (2012).

8. Paulsen, C. E. & Carroll, K. S. Cysteine-Mediated Redox Signaling: Chemistry, Biology, and Tools for Discovery. *Chem. Rev.* **113,** 4633–4679 (2013).

9. Dey, S., Sidor, A. & O'Rourke, B. Compartment-specific Control of Reactive Oxygen Species Scavenging by Antioxidant Pathway Enzymes. *J. Biol. Chem.* **291,** 11185–11197 (2016).

10. Al-Mehdi, A.-B. *et al.* Perinuclear mitochondrial clustering creates an oxidant-rich nuclear domain required for hypoxia-induced transcription. *Sci. Signal.* **5,** ra47 (2012).

11. Booth, D. M., Enyedi, B., Geiszt, M., Várnai, P. & Hajnóczky, G. Redox Nanodomains Are Induced by and Control Calcium Signaling at the ER-Mitochondrial Interface. *Mol. Cell* **63,** 240–8 (2016).

12. Exposito-Rodriguez, M., Laissue, P. P., Yvon-Durocher, G., Smirnoff, N. & Mullineaux, P. M. Photosynthesis-dependent H2O2 transfer from chloroplasts to nuclei provides a high-light signalling mechanism. *Nat. Commun.* **8,** 49 (2017).

13. Shadel, G. S. & Horvath, T. L. Mitochondrial ROS Signaling in Organismal Homeostasis. *Cell* **163,** 560–569 (2015).

14. Quirós, P. M., Mottis, A. & Auwerx, J. Mitonuclear communication in homeostasis and stress. *Nat. Rev. Mol. Cell Biol.* **17,** 213–226 (2016).

15. Dooley, C. T. *et al.* Imaging dynamic redox changes in mammalian cells with green fluorescent protein indicators. *J. Biol. Chem.* **279,** 22284–22293 (2004).

16. Gutscher, M. *et al.* Real-time imaging of the intracellular glutathione redox potential. *Nat. Methods* **5,** 553–559 (2008).

17. Gutscher, M. *et al.* Proximity-based Protein Thiol Oxidation by H_2O_2-scavenging Peroxidases. *J. Biol. Chem.* **284,** 31532–31540 (2009).

18. Hanson, G. T. *et al.* Investigating Mitochondrial Redox Potential with Redox-sensitive Green Fluorescent Protein Indicators. *J. Biol. Chem.* **279,** 13044–13053 (2004).

19. Lohman, J. R. & Remington, S. J. Development of a Family of Redox-Sensitive Green Fluorescent Protein Indicators for Use in Relatively Oxidizing Subcellular Environments † ‡. *Biochemistry* **47,** 8678–8688 (2008).

20. Meyer, A. J. & Dick, T. P. Fluorescent Protein-Based Redox Probes. *Antioxid. Redox Signal.* **13,** 621–650 (2010).

21. Wagener, K. C. *et al.* Redox Indicator Mice Stably Expressing Genetically Encoded Neuronal roGFP: Versatile Tools to Decipher Subcellular Redox Dynamics in Neuropathophysiology. *Antioxid. Redox Signal.* **25,** 41–58 (2016).

22. Ermakova, Y. G. *et al.* Red fluorescent genetically encoded indicator for intracellular hydrogen peroxide. *Nat. Commun.* **5,** 5222 (2014).

23. Fan, Y., Chen, Z. & Ai, H. Monitoring Redox Dynamics in Living Cells with a Redox-Sensitive Red Fluorescent Protein. *Anal. Chem.* **87,** 2802–2810 (2015).

24. Fan, Y., Makar, M., Wang, M. X. & Ai, H.-W. Monitoring thioredoxin redox with a genetically encoded red fluorescent biosensor. *Nat. Chem. Biol.* **13,** 1045–1052 (2017).

25. Tantama, M., Hung, Y. P. & Yellen, G. Imaging Intracellular pH in Live Cells with a Genetically Encoded Red Fluorescent Protein Sensor. *J. Am. Chem. Soc.* **133,** 10034–10037 (2011).

26. Szajewski, R. P. & Whitesides, G. M. Rate Constants and Equilibrium Constants for Thiol-Disulfide Interchange Reactions Involving Oxidized Glutathione. *J. Am. Chem. Soc.* **102,** 2011–2026 (1980).

27. Deutsch, C., Erecińska, M., Werrlein, R. & Silver, I. A. Cellular energy metabolism, trans-plasma and trans-mitochondrial membrane potentials, and pH gradients in mouse neuroblastoma. *Proc. Natl. Acad. Sci. U. S. A.* **76,** 2175–9 (1979).

28. Dickens, C. J., Gillespie, J. I. & Greenwell, J. R. Interactions between intracellular pH and calcium in single mouse neuroblastoma (N2A) and rat pheochromocytoma cells (PC12). *Q. J. Exp. Physiol.* **74,** 671–9 (1989).

29. Allen, M. D. & Zhang, J. A Tunable FRET Circuit for Engineering Fluorescent Biosensors. *Angew. Chemie Int. Ed.* **47,** 500–502 (2008).

30. Shimozono, S. *et al.* Concatenation of cyan and yellow fluorescent proteins for efficient resonance energy transfer. *Biochemistry* **45,** 6267–71 (2006).

31. Wiens, M. *et al.* A tandem green-red heterodimeric fluorescent protein with high FRET efficiency. *ChemBioChem* **118,** 2858–2871 (2016).

32. Evers, T. H., van Dongen, E. M. W. M., Faesen, A. C., Meijer, E. W. & Merkx, M. Quantitative Understanding of the Energy Transfer between Fluorescent Proteins Connected via Flexible Peptide Linkers. *Biochemistry* **45,** 13183–13192 (2006).

33. Yano, T. *et al.* A Novel Fluorescent Sensor Protein for Visualization of Redox States in the Cytoplasm and in Peroxisomes. *Mol. Cell. Biol.* **30,** 3758–3766 (2010).

34. Abraham, B. G. *et al.* Fluorescent protein based FRET pairs with improved dynamic range for fluorescence lifetime measurements. *PLoS One* **10,** 1–15 (2015).

35. Iqbal, A. *et al.* Orientation dependence in fluorescent energy transfer between Cy3 and Cy5 terminally attached to double-stranded nucleic acids. *Proc. Natl. Acad. Sci. U. S. A.* **105,** 11176–81 (2008).

36. Subach, O. M., Entenberg, D., Condeelis, J. S. & Verkhusha, V. V. A FRET-Facilitated Photoswitching Using an Orange Fluorescent Protein with the Fast Photoconversion Kinetics. *J. Am. Chem. Soc.* **134,** 14789–14799 (2012).

37. Lam, A. J. *et al.* Improving FRET dynamic range with bright green and red fluorescent proteins. *Nat. Methods* **9,** 1005–12 (2012).

38. Shaner, N. C. *et al.* Improving the photostability of bright monomeric orange and red fluorescent proteins. *Nat. Methods* **5,** 545–551 (2008).

39. Shaner, N. C. *et al.* Improved monomeric red, orange and yellow fluorescent proteins derived from Discosoma sp. red fluorescent protein. *Nat. Biotechnol.* **22,** 1567–72 (2004).

40. Bajar, B., Wang, E., Zhang, S., Lin, M. & Chu, J. A Guide to Fluorescent Protein FRET Pairs. *Sensors* **16,** 1488 (2016).

41. Kolossov, V. L. *et al.* Thiol-based antioxidants elicit mitochondrial oxidation via respiratory complex III. *Am. J. Physiol. - Cell Physiol.* ajpcell.00006.2015 (2015). doi:10.1152/ajpcell.00006.2015

42. Korge, P., Calmettes, G. & Weiss, J. N. Increased reactive oxygen species production during reductive stress: The roles of mitochondrial glutathione and thioredoxin reductases. *Biochim. Biophys. Acta* **1847,** 514–25 (2015).

43. Zhang, H. *et al.* Glutathione-dependent reductive stress triggers mitochondrial oxidation and cytotoxicity. *Faseb J.* **26,** 1442–1451 (2012).

44. Li, N. *et al.* Mitochondrial complex I inhibitor rotenone induces apoptosis through enhancing mitochondrial reactive oxygen species production. *J. Biol. Chem.* **278,** 8516–8525 (2003).

45. Zhou, Q. *et al.* Rotenone induction of hydrogen peroxide inhibits mTOR-mediated S6K1 and 4E-BP1/eIF4E pathways, leading to neuronal apoptosis. *Toxicol. Sci.* **143,** 81–96 (2015).

46. Gohil, V. M. *et al.* Nutrient-sensitized screening for drugs that shift energy metabolism from mitochondrial respiration to glycolysis. *Nat. Biotechnol.* **28,** 249–55 (2010).

CHAPTER 3. EVALUATING A LOCOMOTOR ASSAY TO SCREEN FOR TOXICANT-INDUCED DOPAMINERGIC DISRUPTION IN ZEBRAFISH LARVAE

*This work was performed at the National Health and Environmental Effects Research Laboratory (NHEERL) of the U.S. Environmental Protection Agency under the guidance of Dr. Stephanie Padilla. This work does not reflect the views of the Agency, nor does mention of trade names or commercial products constitute endorsement or recommendation for use.

3.1 Abstract

Dopamine is a remarkable molecule involved in a number of signaling pathways, including movement and reward-motivated behavior, and dopaminergic disruption is associated with Parkinson's disease onset. Dopaminergic disruption in animals has become an important method for modeling Parkinson's disease. Including, toxicant-induced dopaminergic disruption in zebrafish using chemicals such as ziram and MPTP. Zebrafish are a particularly useful model because they exhibit functionally similar neuronal signaling pathways, behaviors that can be used to assess neural circuit function and can be readily studied through high-throughput screening formats. However, no such behavioral assay has been assessed for robustly screening for dopaminergic disruption. To this end, we evaluated the light:dark transition assay as a high-throughput method for screening dopaminergic disruption in zebrafish larvae after developmental treatment with MPTP or ziram. We report the overt toxicity of ziram, MPTP and additional mitochondrial toxicants, including maneb and fenamidone. We show that the light:dark transition assay is not appropriate for screening for dopaminergic disruption. Instead, locomotion should be monitored in light only to consistently screen for MPTP or ziram-induced dopaminergic disruption in zebrafish larvae after developmental treatment. Additionally, we report for the first time that developmental treatment with the mitochondrial toxicant, picoxystrobin, does not cause behavioral changes in zebrafish larvae as assessed by the light:dark transition assay. However, acute treatment with MPTP causes significant locomotor changes in zebrafish larvae and skin darkening, which implicates noradrenergic disruption in this acute MPTP toxicity.

3.2 Introduction

Parkinson's disease is a neurodegenerative disorder characterized by a loss of dopaminergic neurons in the pars compacta of the substantia nigra.[1,2] While the specific mechanism(s) of dopaminergic depletion remain under intense study, mitochondrial dysfunction and oxidative stress are strongly implicated in this process.[3] The first evidence for mitochondrial dysfunction in PD came about when scientists discovered that the complex I inhibitor, 1-methyl-4-phenyl-1,2,3,6-tetrahydropyridine (MPTP) caused rapid onset of parkinsonian symptoms in people.[4,5] Further, post-mortem studies showed a selective depletion of dopaminergic neurons.[4] The mechanism of MPTP neurotoxicity has since been described, and it is now known that MPTP readily crosses the blood brain barrier and is then converted to MPP^+ by monoamine oxidase type B (MAO-B).[6–9] Following, MPP^+ is selectively taken up into dopaminergic neurons by the dopamine transporter and accumulates in the mitochondria causing ATP depletion, oxidative stress and cell death.[10–12] Since this discovery, other mitochondrial toxicants have been implicated in the pathogenesis of Parkinson's disease, including the herbicide paraquat, and fungicides ziram and maneb.[13,14] These chemicals have been especially useful for developing toxicant-induced animal models of Parkinson's disease; models that continue to be important tools for dissecting the molecular mechanism of Parkinson's disease.[15,16]

Zebrafish (*Danio rerio*) have become a popular and powerful model system for studying behavioral, genetic and molecular aspects of brain disorders.[17,18] Zebrafish genes have at least one ortholog for ~70% of human genes and despite obvious neuroanatomical differences, there is remarkable functional similarity between signaling pathways and key brain regions of zebrafish and mammalian brains.[19–21] For example, the habenula is a group of cells that regulate release of dopamine and serotonin, which is conserved across vertebrate systems.[22] This region is hyper-activated in rodent models of depression and in zebrafish showing fear and anxiety-related behaviors.[23–25] Zebrafish also display a number of simple and complex behaviors, including locomotor, social, anxiety, reward-related and sleep behaviors, which are useful for teasing apart neural circuit function and modeling various central nervous system (CNS) disorders.[26,27] Additionally, zebrafish produce hundreds of offspring weekly, develop rapidly and are relatively economical to maintain.[28] Their externally developing, translucent embryos, and small size at embryonic and larval stages make them especially amenable to high-throughput (e.g. 96-well plate format) developmental and behavioral studies.[29,30] They can also be readily treated with a variety

of chemicals by adding the chemicals directly to the rearing solution, which then diffuses into the animal.[31] For these reasons, zebrafish are a valuable means for developing toxicant-induced models of CNS disorders, and continue to be implemented to study dopaminergic disruption and model Parkinson's disease.[32]

The most commonly used zebrafish toxicant-induced Parkinson's disease model is the MPTP-induced model.[32] MPTP has repeatedly been shown to cause dopaminergic neuronal loss in zebrafish larvae after developmental treatment.[33–38] Similar to humans, this MPTP toxicity is at least in part dependent on monoamine oxidase activity, and dopaminergic neuronal loss is more severe in the posterior tuberculum of the ventral diencephalon of larvae zebrafish, which is thought to correspond to dopaminergic neurons of the mammalian midbrain.[34,35,37,38] Further, this dopaminergic destruction in zebrafish larvae has been shown to cause locomotor impairments, including reduced distance moved and reduced tail reflex in response to touch stimulus.[33,35,38,39] Other toxins used to produce zebrafish models of Parkinson's disease include, 6-hydroxydopamine (6-OHDA), paraquat, rotenone and ziram, though these models have shown varying degrees of dopaminergic depletion and behavioral effects.[32] For example, ziram has been shown to deplete dopaminergic neurons, and one study found that 50 nM ziram treated zebrafish had reduced activity in the dark as assessed by a light:dark transition assay.[40] However, another study found that 10 nM ziram treated zebrafish had increased total activity in a dark-light preference test, though this result was inconsistent between two trials.[41] So while zebrafish are a powerful animal system for modeling Parkinson's disease, further study of the validity and reliability of behavioral assays for assessing dopaminergic disruption in these models is needed.

To this end, we evaluated the applicability of the light:dark transition locomotor assay for screening for dopaminergic disruption in zebrafish larvae using MPTP or ziram. The light:dark transition assay involves tracking the movement of zebrafish in light, turning the light off and continuing to track zebrafish movement in the dark. This light:dark cycle is repeated any number of times and then total distance moved is calculated for a specified interval of time, typically within the light and dark regions.[42,43] This assay was selected because it can be used to assess more than one locomotor behavior type e.g. basal locomotor activity in the light and O-bend activity (~180° orientation changes) following the light:dark transition.[26,42] Additionally, it can be readily implemented in a 96-well plate high throughput screening format, as shown in several previous studies.[44–46]

Herein, we report the overt toxicity of MPTP or ziram as well as other PD-associated and mitochondrial inhibitor chemicals that may be of interest for future studies. We show that the light:dark transition locomotor assay is not appropriate for screening for MPTP and ziram-induced dopaminergic depletion in zebrafish larvae, but that locomotor measurements in light only may be a more applicable and simplified system. Additionally, we report for the first time that the mitochondrial toxicant, picoxystrobin, does not cause any significant locomotor effects as assessed by the light:dark transition locomotor assay, however, acute MPTP treatments result in significant locomotor defects in the light and dark. These findings may indicate applicability of the light:dark transition locomotor assay for screening for noradrenergic disruption in zebrafish.

3.3 Materials and Methods

3.3.1 Husbandry

All studies were approved and in accordance with the guidelines of the Institutional Animal Care and Use Committee (IACUC) at the National Health and Environmental Effects Research Laboratory of the U.S. Environmental Protection Agency. Wild-type adult zebrafish (*Danio rerio*, undefined – an outbred stock of wild-type zebrafish originally obtained from Aquatic Research Organisms, NH and EkkWill Waterlife Resources, FL) were maintained as breeders in an Association for Assessment and Accreditation of Laboratory Animal Care (AAALAC)-approved animal facility with a 14:10 hr light:dark cycle. Adult fish were kept in stand-alone recirculating colony tanks with water temperature at ~28◦C. On the evening prior to embryo collection, adults were placed in a static breeding tank. Embryos were collected the following morning, approximately one hour after light onset.

3.3.2 Embryo Rearing

Embryos collected from breeding tanks were stored in a 28◦C water bath before washing. Embryos were washed with a 0.06% bleach solution in 10% Hank's balanced salt solution (HBSS) (13.7 mM NaCl, 0.54 mM KCl, 25 µM Na_2HPO_4, 44 µM KH_2PO_4, 130 µM $CaCl_2$, 100 µM $MgSO_4$, 420 µM $NaHCO_3$) for 5 minutes, rinsed three times with 10% Hank's solution, and the bleaching and rinsing was repeated once more. Next, fertilized eggs were individually selected and placed in ~200 mL fresh 10% Hank's solution. When embryos reached high blastula stage they were

selected and placed into individual wells of a 96-well microtiter plate with a mesh insert (Multiscreen™ catalog# MANMN4050, Millipore Corp., Bedford, MA) with 250 µL 10% Hank's solution. Plates were sealed with a non-adhesive sealer (Type A, BioRad, Hercules, CA), covered with a lid and wrapped with Parafilm. When not being dosed, plates were kept in an incubator on a 14:10 hr light:dark cycle at 26◦C.

3.3.3 Chemicals and Stock Solutions

Chemicals were purchased from Sigma-Aldrich, including fenamidone (CAS# 161326-34-7, catalog# 33965-100MG-R), maneb (CAS# 12427-38-2, catalog# 45554-250MG), MPTP (CAS# 23007-85-4, catalog# M0896-100MG), picoxystrobin (CAS# 117428-22-5, catalog# 33658-100MG-R), pyraclostrobin (CAS# 175013-18-0, catalog# 33696-100MG-R), and ziram (CAS# 137-30-4, catalog# 45708-250MG).

Fenamidone, MPTP, picoxystrobin and pyraclostrobin were prepared as 20 mM stock solutions in 100% DMSO. A significant amount of vortexing (~10 min) was necessary to solubilize MPTP at 20 mM. Maneb was prepared as a 10 mM stock solution in 100% DMSO due to limited solubility at 20 mM. Ziram was also prepared as a 10 mM stock solution in 100% DMSO but was readily soluble. Because of the highly toxic nature of these chemicals, all solutions containing these compounds were handled with care. Dosing was carried out in a fume hood, and appropriate safety equipment (labcoat, gloves, mask, and goggles) was worn throughout all experiments. Materials were properly disposed of as hazardous waste.

3.3.4 Chemical Treatment

Stock plates for developmental dosing were prepared by serial diluting chemical stock solutions (20 or 10 mM in 100% DMSO) into 100% DMSO at 0.5 log increments. Vehicle controls (DMSO) and positive controls (chlorpyrifos) were included in all plates, and all experimental conditions for each chemical tested were represented on each plate. Stock plates were sealed and stored at 4◦C until further use. For treatment, stock plates were thawed and 1 µL stock solution was diluted in 250 µL 10% Hank's solution to the desired final concentration in 96-well plates containing the zebrafish. The final DMSO concentration was 0.4% (v/v) for all wells.

For developmental treatment, embryos were dosed with chemical starting at 6-8 hours post fertilization (hpf). Solutions were refreshed at 3 days post fertilization (dpf). Plates were moved to

fresh 10% Hank's solution the morning of 5 dpf for chemical washout and to allow for one day depuration before assessment. On the morning of assessment (6 dpf), the 10% Hank's solution was refreshed by again moving the plates into fresh 10% Hank's solution. These chemical washout steps are necessary to ensure that behavioral results are indicative of developmental effects and are not confounded by acute effects due to residual chemical in the well.

For acute treatment, embryos were reared in 96-well plates in 10% Hank's solution. On the morning of 5 dpf, 10% Hank's solution was refreshed, and it was refreshed once more before behavioral measurements on the morning of 6 dpf. Immediately prior to behavioral measurements, plates were acutely treated with DMSO (vehicle control) and MPTP (2.53 – 80 μM) from stock plates.

3.3.5 Overt Toxicity Assessment

Lethality and malformation (terata) was assessed by visual inspection of larvae under a dissection scope at 6 dpf. Dead larvae were noted, as indicated by coagulation, decay or no visible heartbeat. Unhatched larvae were also noted. Otherwise, larvae were assessed for malformations in the following general categories: swim bladder inflation, craniofacial (e.g. small eyes or head), edema (e.g. mild or severe), position (e.g. lying on side), tail (e.g. kinked or shortened), or hemorrhage. Toxicity was qualitatively scored as follows: dead = 40, severely abnormal = 25, unhatched = 20, abnormal = 15, otherwise normal with uninflated swim bladder = 10, normal = 0. These qualitative scores are based on previous reports that describe more thorough malformation assessments using a similar 0 – 40 score range.[31,47]

Toxicity scores for each compound were used to determine chemical potencies as half-maximal activity concentrations (AC50). Here, average dose response toxicity scores were fitted to a sigmoidal dose response equation in Origin® 2019.

3.3.6 Behavioral Testing

For developmental neurotoxicity behavioral testing, the highest dose used was determined by the overt toxicity studies and was set to the highest concentration that did not cause lethality or malformation for each chemical. This step is especially important to ensure that the behavioral data is representative of developmental neurotoxicity, rather than overt toxicity or malformations. For example, a curved spine is likely to cause reduced locomotion, which would be difficult if not

impossible to differentiate from locomotor changes caused by neurotoxicity. Consequently, fish showing physical malformations were not included in behavioral assessment data. Thus, terata was also assessed immediately after behavioral tests and abnormal fish (including uninflated swim bladder) were not included in the behavioral analysis. As a positive control for chemical potency, the lowest dose that caused lethality or malformation from the overt toxicity data was included for each chemical on the plate, but none of the fish at this dose were included in the behavioral analysis.

Behavioral testing was performed at 6 dpf in 96-well plates after one day depuration and an additional 10% Hank's solution refresh the morning of testing. Immediately following the 10% Hank's solution refresh, the plates were placed in a light tight drawer in a dark room at 26◦C to acclimate for at least two hours. All behavior measurements were started after 11 am, when zebrafish locomotion is expected to be relatively stable for the day.[43] After acclimation, plates were placed on a light box of a Noldus behavior system and locomotion was measured for a 20-minute dark equilibration period, followed by 40 minutes of light (20 lux), and then 40 minutes of dark. The 20-minute dark equilibration period was included to allow the fish to settle after moving the plates, and thus was not included in the final analysis.

Acute testing was performed similarly at 6 dpf in 96-well plates, except fish were dosed with MPTP immediately prior to placing them on the light box and beginning behavioral measurement. Locomotion was measured for a 20-minute dark equilibration period, followed by three cycles of 40 minutes of light (20 lux) and 40 minutes of dark. Three light:dark cycles were included to ensure that peak dose effect was measured and to determine how acute effects in the light and dark change over time. Acute behavioral measurements were also started after 11 am and malformation was assessed immediately afterward.

Zebrafish locomotion was measured from videos using Ethovision software Version 8.5 with a tracking rate of 5 frames/sec. Tracking was analyzed for distance moved (cm). All locomotion data is given as distance moved (cm) per 2-minute measurement interval.

3.3.7 Statistics

All initial statistical comparisons were performed by multiple comparison analysis of variance (ANOVA), including movement measured across all light periods in a single test to avoid an increased probability of type 1 errors from multiple comparisons in the same set of data. When interactions existed across light periods and movement, data were then further divided into

individual light periods for lower-order ANOVAs. When interaction between an individual light period and movement was found, a post hoc Fisher's Protected Least Significant Difference (PLSD) test was performed to determine doses that were significantly different from the vehicle control. Significance was set at $p \leq 0.05$.

For developmental neurotoxicity, data was averaged across each 40-minute light setting (40 minutes in light, 40 minutes in dark) (Figures 3.4, 3.5, 3.6). Later, the developmental neurotoxicity data was further separated into four epochs that were 20 minutes each (Figure 3.7) to approximate different light transition stages (1. 0 – 20 minute dark:light transition, 2. 20 – 40 minute basal light, 3. 40 – 60 minute light:dark transition, 4. 60 – 80 minute basal dark). Acute toxicity data was similarly analyzed, but data was averaged across each 40-minute light setting to give a total of three individual light periods and three individual dark periods (Figure 3.8).

3.4 Results

3.4.1 Overt Toxicity

We selected MPTP and ziram as our primary chemicals for dopaminergic disruption because they have previously been reported to cause a loss of dopaminergic neurons in larval zebrafish after developmental treatment.[33–38,48] However, previous studies did not determine the overt toxicity of these chemicals, and in fact, there has been considerable discrepancy in the concentrations of MPTP used to developmentally treat zebrafish and showing behavioral effects.[33–36,38,39] For example, one study found larvae treated with 50 μM MPTP showed curved body and were completely motionless, while another study found reduced locomotion at 1000 μM, but not 100 μM MPTP.[36,38] It is especially important to determine overt toxicity because it allows us to hone our dosing range for the behavioral assay and ensures that locomotor measurements are not confounded by morphological abnormalities.

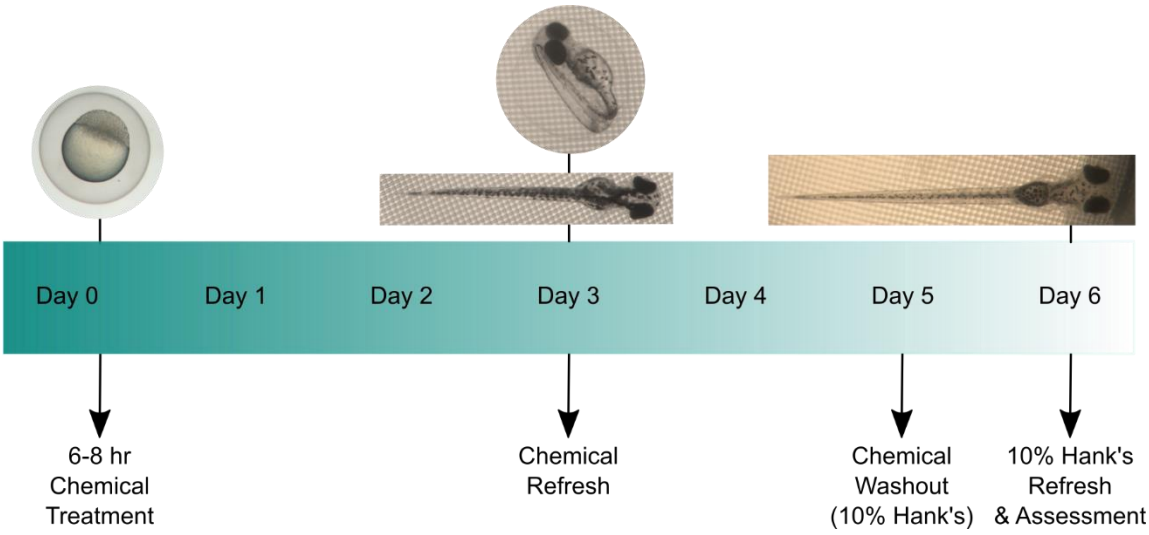

Figure 3.1 Protocol for zebrafish developmental treatment with chemicals.

Fertilized eggs were selected, placed in 96-well plates and developmentally treated as shown. Zebrafish were assessed for survival and morphological abnormalities at 6 dpf. For behavioral assessment, locomotor assays were run at 6 dpf, followed by survival and morphological assessment.

Therefore, we first qualitatively assessed the overt toxicity of MPTP and ziram across a wide range of concentrations following our developmental treatment protocol (Figure 3.1, Table 3.1). In this protocol, embryos were individually placed in wells of 96-well plates and treated with chemicals starting at 6-8 hpf. Chemicals were refreshed at 3 dpf, washed out at 5 dpf and zebrafish were assessed for death, morphological abnormality, hatching and swim bladder inflation at 6 dpf (Figure 3.1). Additionally, we determined the overt toxicity of several other chemicals that may be of interest for future studies because of their action as mitochondrial inhibitors and their oxidative stress effects in zebrafish (Table 3.1), including, the PD-associated fungicide, maneb, and two strobilurin fungicides, which inhibit mitochondrial respiration by binding to the ubiquinol oxidizing site (Qo) of complex III (Table 3.1).[49,50]

Table 3.1 PD-associated and mitochondrial inhibitor chemicals tested for overt toxicity in developing zebrafish.

Chemical	Use	Mode of Action in Mitochondria	Relevant Effects in Zebrafish	AC50 (μM)	Behavioral Dose Range (μM)
MPTP	Destruction of dopaminergic neurons in animal models of PD[51]	Interferes with complex I[10,11]	Loss of dopaminergic neurons & oxidative stress[33–38,48]	No Fit	0.25 – 25.3
Ziram	Fungicide	Unknown, inhibits the ubiquitin-proteasomal system (UPS)[52]	Loss of dopaminergic neurons[40]	0.45	0.0004 – 0.04
Maneb	Fungicide	Inhibits complex III[53]	Oxidative stress not detected[54]	4.03	Not tested
Picoxystrobin	Fungicide	Inhibits Qo in complex III[50,55,56]	Oxidative stress[57,58]	0.29	0.0025 – 0.25
Pyraclostrobin	Fungicide	Inhibits Qo in complex III[50,55,56]	Oxidative stress[57,59]	0.24	Not tested
Fenamidone	Fungicide	Inhibits Qo in complex III[55]	Limited testing, oxidative stress not assessed[31]	2.45	Not tested

Terata assessment data was scored similar to previous studies and data were fitted to a sigmoidal dose response curve to determine AC50's (Table 3.1, Figure 3.2).[31,47] We found MPTP to be the least overtly toxic, where only the highest dose (80 μM) showed significant morphological effects in zebrafish, including uninflated swim bladders and edema. Thus, at these concentrations we were unable to fit the MPTP overt toxicity curve to determine an AC50 (Table 3.1, Figure 3.2). However, these data allowed us to determine the highest usable MPTP concentration for our behavioral assay, which is the highest dose with minimal terata effects (25.3 μM). Thus, our behavioral dose range for MPTP was set to 0.25 – 25.3 μM (Table 3.1). We determined that pyraclostrobin is the most overtly toxic (AC50 = 0.24 μM), followed closely by the related strobilurin fungicide, picoxystrobin (Table 3.1). Interestingly, both diothiocarbamate chemicals tested resulted in embryos that were alive, but unhatched by 6 dpf at 0.13, 0.4 and 1.26 μM ziram and 4 μM maneb. The reduced hatching rate for ziram and maneb is in line with previous reports that measured the developmental toxicity of these chemicals.[41,54] From these data, behavioral dose ranges were determined for the other two chemicals selected for behavioral testing – ziram and picoxystrobin (Table 3.1).

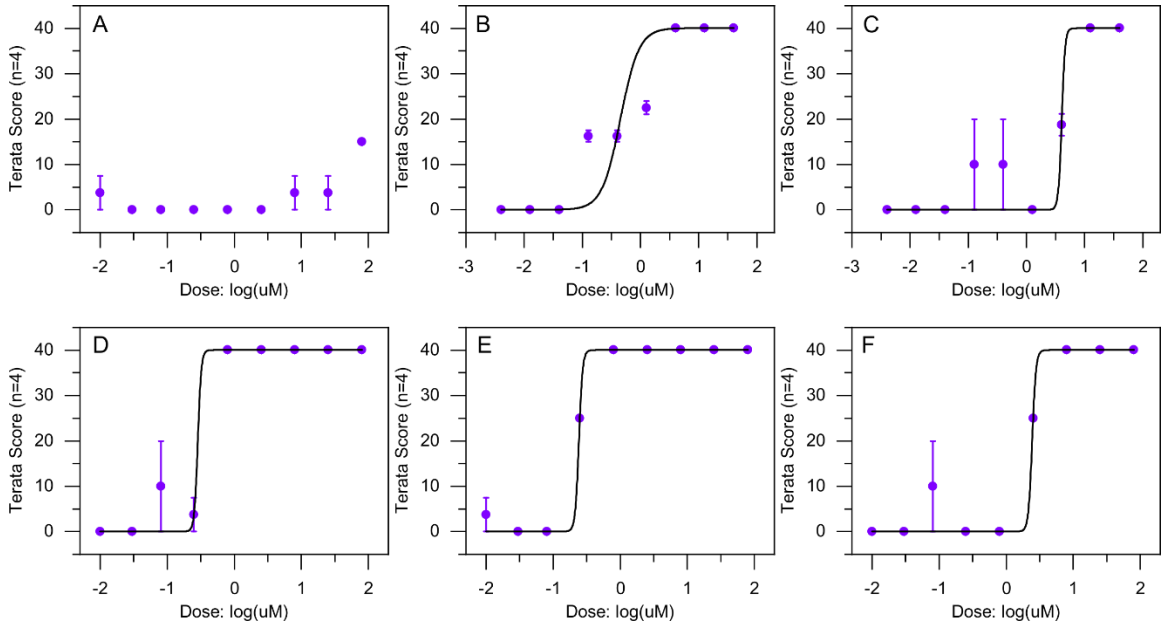

Figure 3.2 Terata dose response data to determine overt toxicity of selected chemicals.

Zebrafish were developmentally treated with (A) MPTP, (B) ziram, (C) maneb, (D) picoxystrobin, (E) pyraclostrobin, and (F) fenamidone and terata data were fitted to a dose response to determine AC50's. Lines show the average fit for n = 4. Error bars are sem.

3.4.2 Neurodevelopmental Toxicity

We next assessed neurodevelopmental toxicity of MPTP, ziram and picoxystrobin by developmentally treating zebrafish embryos with these chemicals and measuring their movement in a light:dark transition behavioral assay. In this behavioral assay, 6 dpf zebrafish in fresh 10% Hank's solution are tested after 11 am, when overall fish movement is expected to be more stable as described by MacPhail et al.[43] The 96-well plate containing the fish is moved to a light box, locomotion is measured in the dark for 20 minutes to allow the fish to equilibrate (not shown), immediately followed by 40 minutes in the light and 40 minutes in the dark (Figure 3.3). Zebrafish larvae follow a typical pattern in these light settings, where movement initially increases and then plateaus in the light, followed by a sharp increase in movement in the dark that then levels off to a lower basal level than in the light (Figure 3.3).[42,43] In the dark period following the light:dark transition, fish movement differs because fish show O-bend activity (~180° turns).[26,42] Thus, we made comparisons across dose groups in the average light and average dark periods for each 40

minute measurement to determine if there are any significant changes in locomotion in these light periods with chemical treatment.

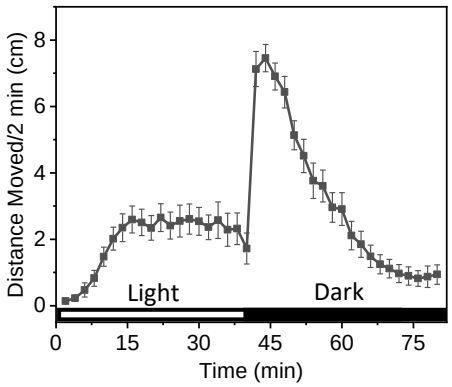

Figure 3.3 Typical larval zebrafish locomotor response in the light:dark transition behavioral assay.

Zebrafish larvae were developmentally treated with 0.4% DMSO in Hank's solution, and locomotion was measured in 2-minute intervals across 40 minutes light, followed by 40 minutes dark. The horizontal white bar indicates light exposure, while the black bar indicates dark. Lines show average movement for n = 30. Error bars are sem.

For zebrafish treated with MPTP (0.253 – 25.3 μM) during development, no overall effect of treatment on locomotion was observed in the light or dark (Figure 3.4). While there does appear to be a reduction in locomotion in the light at 25.3 μM MPTP, this effect was not significant within the dosing range tested. Thus, the light:dark transition assay does not reveal locomotor deficits induced by MPTP dopaminergic depletion. However, it should be noted that in this MPTP assay the light phase was cut short at 30 minutes, rather than the planned 40 minutes. For this reason, this experiment should be repeated with 40 minutes light and 40 minutes dark in order to state with certainty that MPTP does not cause locomotor effects in this specific light:dark transition assay format.

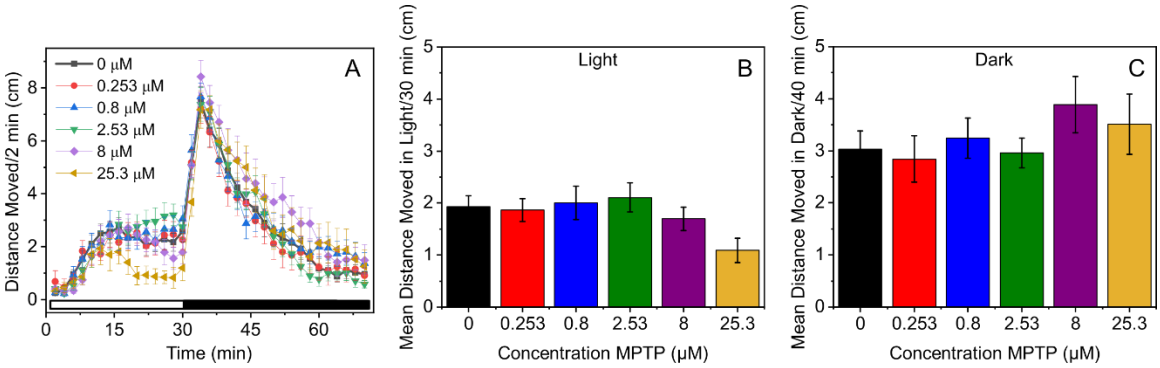

Figure 3.4 Developmental MPTP treatment does not alter larval locomotion in a light:dark transition assay.

Zebrafish were treated with MPTP from 6-8 hpf to 5 dpf, and (A) locomotor activity was measured at 6 dpf in 30 minutes light, followed by 40 minutes dark. The horizontal white bar indicates light exposure, while the black bar indicates dark. Average locomotor activity was not significantly different from controls in the (B) light (distance moved in light x dose interaction, $p = 0.1539$) or (C) dark (distance moved in dark x dose interaction, $p = 0.5700$). All data represented as mean ± sem. n for 0 µM = 31, n for 0.253 µM = 23, n for 0.8 µM = 24, n for 2.53 µM = 22, n for 8 µM = 19, n for 25 µM = 17. Significance set at $p \leq 0.05$.

For zebrafish treated with ziram (0.4 – 40 nM) during development, no overall effect of treatment on locomotion was observed in the light or dark (Figure 3.5). Additionally, zebrafish developmentally treated with picoxystrobin (2.53 – 250.3 nM) showed no overall effect of treatment on locomotion in the light or dark (Figure 3.6). Picoxystrobin was tested because two previous reports showed that it causes oxidative stress in zebrafish, though dopaminergic depletion has not been reported for this chemical.[57,58] Thus, our results reveal that the light:dark transition assay is not appropriate for screening for locomotor deficits induced by MPTP or ziram dopaminergic depletion, and picoxystrobin does not result in locomotor changes detectable by this behavioral assay.

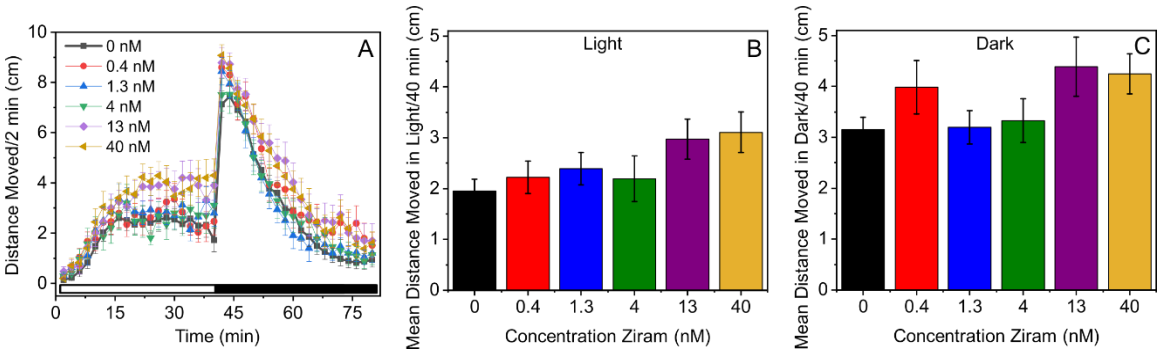

Figure 3.5 Developmental ziram treatment does not alter larval locomotion in a light:dark transition assay.

Zebrafish were treated with ziram from 6-8 hpf to 5 dpf, and (A) locomotor activity was measured at 6 dpf in 40 minutes light, followed by 40 minutes dark. The horizontal white bar indicates light exposure, while the black bar indicates dark. Average locomotor activity was not significantly different from controls in the (B) light (distance moved in light x dose interaction, $p = 0.1093$) or (C) dark (distance moved in dark x dose interaction, $p = 0.1530$). All data represented as mean ± sem. n for 0 nM = 30, n for 0.4 nM = 21, n for 1.3 nM = 22, n for 4 nM = 21, n for 13 nM = 21, n for 40 nM = 22. Significance set at $p \leq 0.05$.

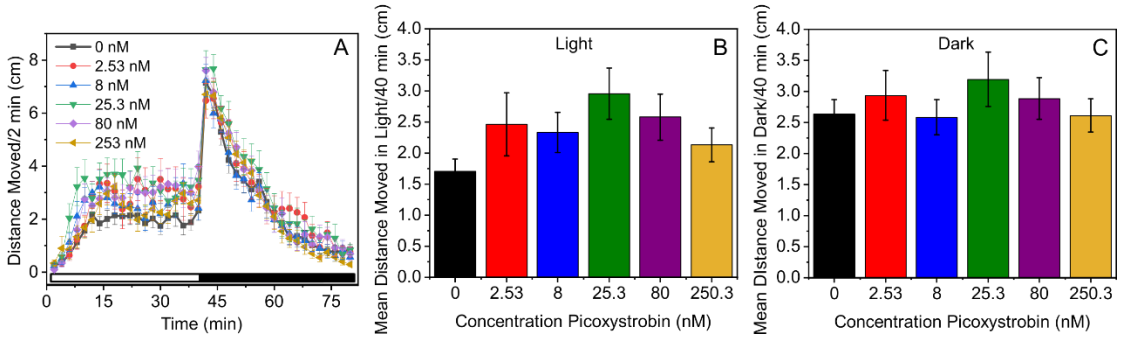

Figure 3.6 Developmental picoxystrobin treatment does not alter larval locomotion in a light:dark transition assay.

Zebrafish were treated with picoxystrobin from 6-8 hpf to 5 dpf, and (A) locomotor activity was measured at 6 dpf in 40 minutes light, followed by 40 minutes dark. The horizontal white bar indicates light exposure, while the black bar indicates dark. Average locomotor activity was not significantly different from controls in the (B) light (distance moved in light x dose interaction, $p = 0.1562$) or (C) dark (distance moved in dark x dose interaction, $p = 0.7555$). All data represented as mean ± sem. n for 0 nM = 32, n for 2.53 nM = 23, n for 8 nM = 22, n for 25.3 nM = 23, n for 80 nM = 24, n for 250.3 nM = 24. Significance set at $p \leq 0.05$.

At first thought, these results appear counter to previous reports, particularly for MPTP, which has consistently been shown to cause reduced locomotion in zebrafish developmentally treatment with it.[33,38,39,60,61] However, no previous reports have assessed locomotor activity for

developmental MPTP treatment using the light:dark transition assay, but rather measure locomotion in a single light setting.[33,38,39,60,61] While it is known that zebrafish larvae show a unique locomotor response in the light:dark transition, it is unclear if locomotion differs in the dark:light transition vs basal light or basal dark.[26,42] Though, it is possible that zebrafish larvae show distinct locomotor effects or other neurobehavioral effects in these different light conditions. For this reason, we further analyzed our behavioral data as four epochs, two for the light period and two for dark: 1. Dark:light transition (0 – 20 min), 2. Basal light (20 – 40 min), 3. Light:dark transition (40 – 60 min), and 4. Basal dark (60 – 80 min). This analysis revealed that larval zebrafish locomotion is significantly reduced in basal light after developmental treatment with 25.3 μM MPTP and significantly increased in basal light after developmental treatment with 13 or 40 μM ziram (Figure 3.7). Locomotion was not significantly different in the other three lighting epochs (dark:light transition, light:dark transition and basal dark) for MPTP and ziram and, picoxystrobin developmental treatment did not result in any significant changes in locomotion in basal light or the other three lighting epochs (Figure 3.7).

These data show that behavioral effects related to MPTP and ziram developmental treatment are most prominent in basal light and indicate that the light:dark transition assay may not be necessary for screening for MPTP and ziram behavioral effects. However, further studies should be performed monitoring zebrafish movement after developmental treatment with MPTP and ziram in light only conditions to eliminate the potential cross-talk between light settings and provide further support for these findings.

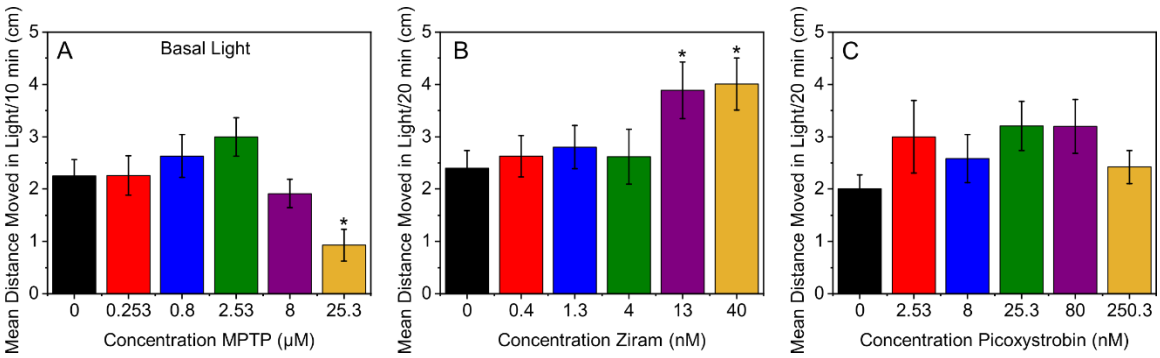

Figure 3.7 Developmental MPTP and ziram treatments alter larval locomotion in basal light, while picoxystrobin does not.

Locomotor activity was assessed for larval zebrafish in basal light (after 20-minute light equilibration). (A) MPTP developmental treatment showed significantly reduced locomotor activity in basal light at 25.3 μM in comparison to the 0 μM control (distance moved in basal light x dose interaction, $p = 0.0079$; 0 μM MPTP x 25.3 μM interaction, $p = 0.0112$), (B) ziram developmental treatment showed significantly increased locomotor activity in basal light at 13 and 40 μM in comparison to the 0 μM control (distance moved in basal light x dose interaction, $p = 0.0347$; 0 μM ziram vs 13 μM, $p = 0.0154$; 0 μM ziram vs 40 μM, $p = 0.0081$), and (C) picoxystrobin developmental treatment did not show any significant changes in locomotor activity in basal light (distance moved in basal light x dose interaction, $p = 0.2936$). All data represented as mean ± sem. Significance set at $p \leq 0.05$, *p-value ≤ 0.05, **p-value ≤ 0.001, ***p-value ≤ 0.0001.

3.4.3 MPTP Acute Toxicity

Previous studies have shown significant locomotor defects in adult zebrafish after acute treatment with MPTP, despite having no reduction in dopaminergic neurons.[33,62] We were curious if larval zebrafish similarly show locomotor defects with acute MPTP treatment and whether our light:dark transition assay could be used to screen for these motor deficits. Therefore, we next assessed locomotor changes in larval zebrafish acutely treated with MPTP using our light:dark transition assay.

Herein, 6 dpf zebrafish that developed normally in 10% Hank's solution were acutely treated with varying concentrations of MPTP (2.53 – 80 μM). 96-well plates containing the acutely treated zebrafish were immediately placed on a light box after treatment and allowed to equilibrate for 20-minutes in the dark (data not shown). Then, movement was measured for three cycles of 40 minutes light, 40 minutes dark (Figure 3.8). We discovered that acute MPTP causes significant changes in locomotion across all light and dark periods. Locomotion was most significantly

reduced in the first light and dark periods, and reduction in movement became less pronounced over time (Figure 3.8). Overall, we see more of an effect in light versus dark, which indicates that routine swimming behavior is more affected than O-bend activity. Interestingly, 25.3 μM MPTP activity is significantly reduced in the first dark period, but gradually increases and becomes significantly increased by the 3rd dark period, which is a markedly different pattern from the other doses tested (Figure 3.8).

Additionally, a distinct pigmentation pattern change was noted for ~71% (12 out of 17) zebrafish acutely treated with 80 μM MPTP, where treated fish appeared much darker than controls (Figure 3.9). This pigmentation change looks to be due to melanosome dispersion, which is the main factor responsible for zebrafish skin darkening. We did not note any pigmentation changes in fish developmentally treated with MPTP, ziram or picoxystrobin, nor have any previous studies. However, this type of skin-darkening effect has been reported in adult zebrafish after acute injection with 225 mg/kg MPTP.[33] Thus, these distinct behavioral and skin pigmentation changes in larval zebrafish after acute MPTP treatment may be similar to those observed in adult zebrafish acutely treated with MPTP. These results show that the light:dark transition assay is an effective method for screening for neurotoxic effects in larval zebrafish after acute MPTP treatment.

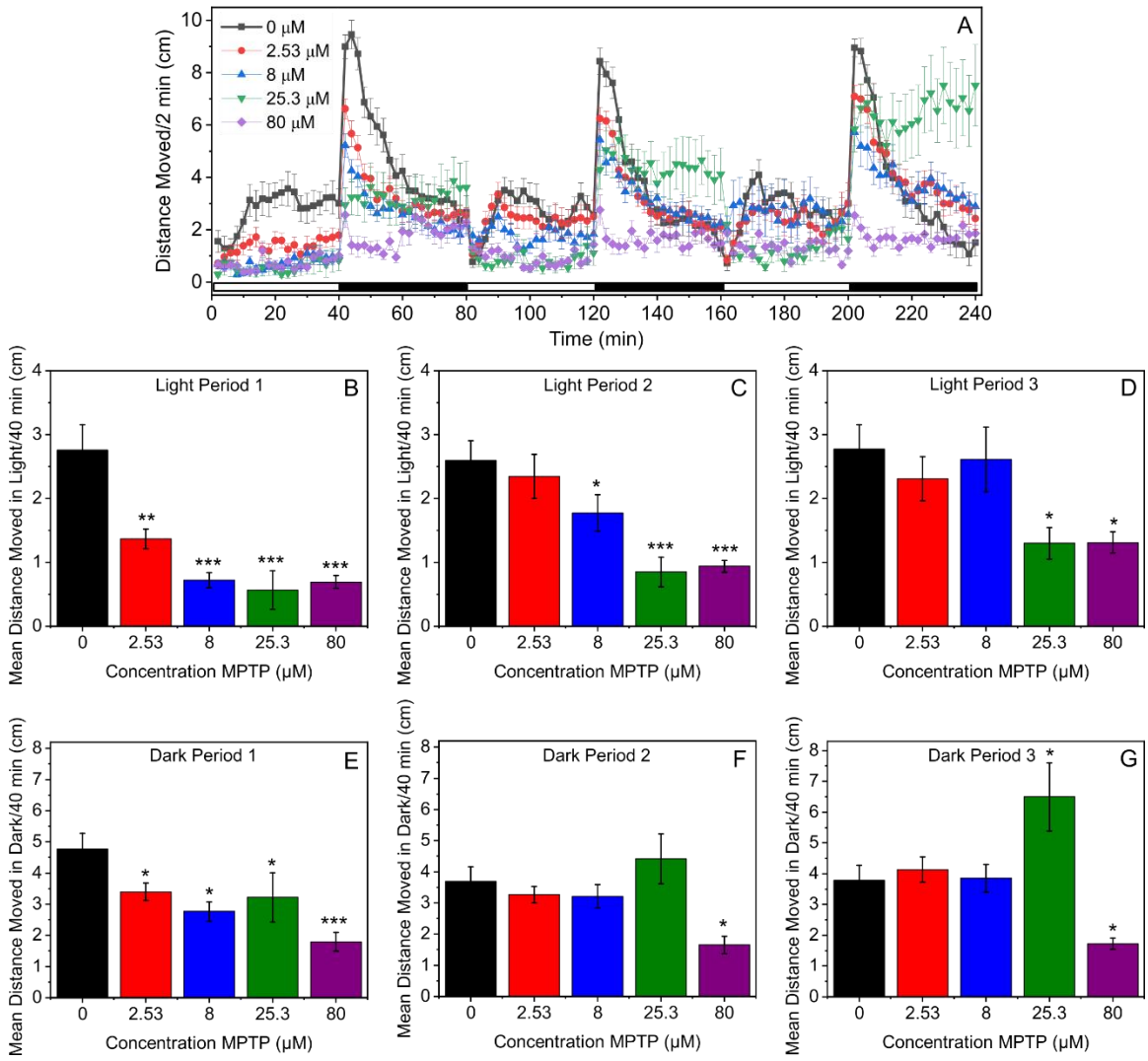

Figure 3.8 Acute MPTP treatment significantly alters larval locomotion in a light:dark transition assay.

Zebrafish were acutely treated with MPTP at 6 dpf and (A) locomotor activity was measured in three cycles of 40 minutes light, followed by 40 minutes dark. The horizontal white bar indicates light exposure, while the black bar indicates dark. Average locomotor activity was significantly different from controls in (B) light period 1 (distance moved in light period 1 x dose interaction, $p < 0.0001$; 0 µM MPTP vs 2.53 µM, $p = 0.0003$; 0 µM MPTP vs 8.0 µM, $p < 0.0001$; 0 µM MPTP vs 25.3 µM $p < 0.0001$; 0 µM MPTP vs 80 µM, $p < 0.0001$), (C) light period 2 (distance moved in light period 2 x dose interaction, $p < 0.0001$; 0 µM MPTP vs 8.0 µM, $p = 0.0339$; 0 µM MPTP vs 25.3 µM, $p < 0.0001$; 0 µM MPTP vs 80 µM, $p < 0.0001$), (D) light period 3 (distance moved in light period 3 x dose interaction, $p = 0.0058$; 0 µM MPTP vs 25.3 µM, $p = 0.0034$; 0 µM MPTP vs 80 µM, $p = 0.0043$), (E) dark period 1 (distance moved in dark period 1 x dose interaction, $p = 0.0006$; 0 µM MPTP vs 2.53 µM, $p = 0.0384$; 0 µM MPTP vs 8.0 µM, $p = 0.0030$; 0 µM MPTP vs 25.3 µM, $p = 0.0201$; 0 µM MPTP vs 80 µM, $p < 0.0001$), (F) dark period 2 (distance moved in dark period 2 x dose interaction, $p = 0.0044$; 0 µM MPTP vs 80 µM, $p < 0.0030$), and (G) dark period 3 (distance moved in dark period 3 x dose interaction, $p < 0.0001$; 0

μM MPTP vs 25.3 μM, $p < 0.0014$, 0 μM MPTP vs 80 μM, $p = 0.0161$). All data represented as mean ± sem. n for 0 μM = 24, n for 2.53 μM = 18, n for 8 μM = 18, n for 25.3 μM = 18, n for 80 μM = 17. Significance set at $p \leq 0.05$, *p-value ≤ 0.05, **p-value ≤ 0.001, ***p-value ≤ 0.0001.

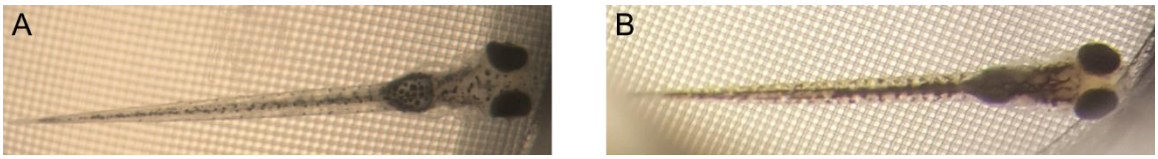

Figure 3.9 Larval zebrafish acutely treated with 80 μM MPTP have darkened pigmentation patterns.

(A) Control zebrafish that were not treated with MPTP show typical pigmentation pattern with small spots, while (B) zebrafish acutely treatment with 80 μM MPTP appear darker due to significant melanosome dispersion.

3.5 Discussion

In this study, we investigated the efficacy of light:dark transition assay for screening for dopaminergic disruption in zebrafish larvae using MPTP and ziram. First, we measured the overt toxicity of MPTP, ziram and other PD-associated and mitochondrial toxicants including, maneb, picoxystrboin, pyraclostrobin and fenamidone. While we were unable to determine an exact AC50 for MPTP at the dosing range tested, we did find that 80 μM MPTP results in abnormalities including uninflated swim bladder and edema, while 25.3 μM treated fish appeared normal. Thus, we selected 25.3 μM as our maximum concentration for the behavioral assay. While this level of MPTP toxicity is comparable to some studies, it is markedly different from other studies that have performed developmental treatments of MPTP for behavioral assays at concentrations as high as 1000 μM.[33–36,38,39,60,61] It is unclear if these differences in MPTP toxicity are due to lot variability, solubility issues or difference in treatment protocols, which is why we opted to determine overt toxicity for our specific methods. We strongly recommend that future studies do the same in addition to ensuring that malformed or abnormal animals are not included in behavioral data.

Furthermore, of the chemicals tested in this study we found pyraclostrobin and picoxystrobin to be the most acutely toxic with AC50's of 0.24 and 0.29 μM, respectively. Ziram is also relatively toxic (AC50 = 0.29 μM), while fenamidone (AC50 = 2.45 μM) and maneb (AC50 = 4.03 μM) are less so. Interestingly, the two diothiocarbamates tested, ziram and maneb, significantly reduced

hatching rates as zebrafish remained unhatched by 6 dpf, which is thought to be a result of oxidative stress and impaired mitochondrial bioenergetics.[41,54]

After determining over toxicity levels, we screened MPTP, ziram and picoxystrobin for locomotor changes using the light:dark transition behavioral assay. When averaging distance traveled across the two different lighting conditions used in this assay (light and dark) we did not find any significant changes in locomotion for any of the chemicals tested. However, after further splitting these lighting conditions into 4 epochs (dark:light transition, basal light, light:dark transition, basal dark) we found locomotion to be significantly reduced in basal light for larval zebrafish developmentally treated with MPTP and ziram, but not picoxystrobin. To our knowledge, this is the first report on picoxystrobin behavioral affects in zebrafish, or the lack thereof.

Our developmental MPTP results align well with previous reports that used MPTP and showed reduced locomotion in a single light setting.[33,38,39,60,61] For ziram, however, our results differ from a previous study that reported that zebrafish developmentally treated with 50 nM ziram moved less in the light:dark transition period.[40] However, this study only measured behavior for one concentration of ziram and did not record in the light long enough to reach a basal light response. This discrepancy provides further support for the need to characterize these behavioral assays for applicability for robustly screening for specific neurodevelopmental effects. Indeed, our results indicate that the light:dark transition assay may not be appropriate to screen for dopaminergic disruption after developmental treatment with MPTP or ziram. Rather, a simpler behavioral assay using light only should prove more effective.

On the other hand, larval zebrafish acutely treated with MPTP showed significant locomotor changes across all doses tested in both the light and dark. These effects declined over time, but were not completely abated after three light:dark cycles. These results were intriguing not only because of the dramatic behavioral changes, but because we also observed skin darkening at the highest MPTP dose group. It is known that zebrafish can quickly adjust their pigmentation to appear darker or lighter to blend in with their background. Skin darkening is accomplished by the dispersion of pigment granules, called melanosomes, which are found in the melanophore cells, while skin lightening is the aggregation of melanosomes. This process is controlled by adrenergic receptors, primarily by noradrenaline activation.[63]

While this skin darkening behavior has not previously been reported for zebrafish developmentally treated with MPTP, it has been observed in adult zebrafish after acute treatment

with MPTP.[33] Interestingly, these adult zebrafish showed significant motor changes in the absence of dopaminergic neuronal loss, but with a reduction in dopamine and noradrenaline levels.[33,62] Thus, these acute MPTP effects in adult zebrafish are thought to be distinct from developmental MPTP treatment effects. Given that we also observed skin darkening with acute MPTP treatment and the fact that zebrafish brains are mostly developed by 6 dpf, the acute neurotoxic effects we observed here are likely to be more similar to acute MPTP effects in adult zebrafish than developmental effects. Thus, the distinct behavioral changes we observed in our light:dark transition assay for acute MPTP treatment may be noradrenergic-related.

It is not currently known why zebrafish exhibit increased movement immediately following a quick transition from light to dark in the light:dark transition assay. This ~180° turn (O-bend) behavior is thought to be a navigational effect to move away from the dark, maybe to avoid a potential threat, which is supported by the fact that zebrafish larvae exhibit scotophobia or a dark avoiding behavior.[26,42] In either case, our work here suggests that noradrenaline may be involved in this behavioral response. Indeed, a previous study reported significant changes in larval zebrafish behavior in the light:dark transition assay after acute treatment with the anxiolytic compound, ethanol.[44] Thus, the light:dark transition assay may be useful for assessing for anxiety-related or noradrenergic-related behavioral affects. Future studies should further characterize the applicability of the light:dark transition assay to robustly screen for noradrenergic disruption.

3.6 References

1. Fearnley, J. M. & Lees, A. J. Ageing and parkinson's disease: Substantia nigra regional selectivity. *Brain* **114,** 2283–2301 (1991).

2. Giguère, N., Burke Nanni, S. & Trudeau, L.-E. On Cell Loss and Selective Vulnerability of Neuronal Populations in Parkinson's Disease. *Front. Neurol.* **9,** (2018).

3. Vera Dias, Eunsung Junn, M. M. M. The Role of Oxidative Stress in Parkinson's Disease. *J Park. Dis* **3,** 461–491 (2014).

4. Davis, G. C. *et al.* Chronic parkinsonism secondary to intravenous injection of meperidine analogues. *Psychiatry Res.* **1,** 249–254 (1979).

5. Langston, J. William; Ballard, Philip, Tetrud, James W.; Irwin, I. Chronic Parkinsonism in Humans due to a Product of Meperidine-Analog Synthesis Author (s): J . William Langston , Philip Ballard , James W . Tetrud , Ian Irwin Published by : American Association for the Advancement of Science Stable URL : http://www.js. *Adv. Sci.* **219,** 979–980 (1983).

6. Langston, J. W., Irwin, I., Langston, E. B. & Forno, L. S. 1-Methyl-4-phenylpyridinium ion (MPP+): Identification of a metabolite of MPTP, a toxin selective to the substantia nigra. *Neurosci. Lett.* **48,** 87–92 (1984).

7. Markey, S. P.; Johannessen, J. N.; Chiueh, C. C.; Burns, R. S.; Herkenham, M. A. Intraneuronal Generation of a Pyridinium Metabolite May Cause Drug-Induced Parkinsonism. *Nat. Publ. Gr.* **311,** 464–467 (1984).

8. Chiba, Kan; Trevor, Anthony; Castagnoli, N. Metabolism of the Neurotoxic Tertiary Amine, MPTP, by Brain Monoamine Oxidase. *Biochem. Biophys. Res. Commun.* **120,** 574–578 (1984).

9. Heikkila, R. E., Manzino, L., Cabbat, F. S. & Duvoisin, R. C. Protection against the dopaminergic neurotoxicity of 1-methyl-4-phenyl-1,2,5,6-tetrahydropyridine by monoamine oxidase inhibitors. *Nature* **311,** (1984).

10. Ramsay, R. R., Dadgar, J., Trevor, A. & Singer, T. P. Energy-driven uptake of N-methyl-4-phenylpyridine by brain mitochondria mediates the neurotoxicity of MPTP. *Life Sci.* **39,** 581–588 (1986).

11. Ramsay, R. R., Salach, J. I. & Singer, T. P. Uptake of the neurotoxin 1-methyl-4-phenylpyridine (MPP+) by mitochondria and its relation to the inhibition of the mitochondrial oxidation of NAD+-linked substrates by MPP+. *Biochem. Biophys. Res. Commun.* **134,** 743–748 (1986).

12. Chan, P., Delanney, L. E., Irwin, I., Langston, J. W. & Monte, D. Rapid ATP Loss Caused by 1-Methyl-4-Phenyl-1,2,3,6-Tetrahydropyridine in Mouse Brain. *J. Neurochem.* **57,** 348–351 (1991).

13. Tanner, C. M. *et al.* Rotenone, paraquat, and Parkinson's disease. *Environ. Health Perspect.* **119,** 866–872 (2011).

14. Wang, A. *et al.* Parkinson's disease risk from ambient exposure to pesticides. *Eur. J. Epidemiol.* **26,** 547–555 (2011).

15. Martinez, T. N. & Greenamyre, J. T. Toxin Models of Mitochondrial Dysfunction in Parkinson's Disease. *Antioxid. Redox Signal.* **16,** 920–934 (2012).

16. Jagmag, S. A., Tripathi, N., Shukla, S. D., Maiti, S. & Khurana, S. Evaluation of models of Parkinson's disease. *Front. Neurosci.* **9,** (2016).

17. Kalueff, A. V., Stewart, A. M. & Gerlai, R. Zebrafish as an emerging model for studying complex brain disorders. *Trends Pharmacol. Sci.* **35,** 63–75 (2014).

18. Fontana, B. D., Mezzomo, N. J., Kalueff, A. V. & Rosemberg, D. B. The developing utility of zebrafish models of neurological and neuropsychiatric disorders: A critical review. *Exp. Neurol.* **299,** 157–171 (2018).

19. Howe, K. *et al.* The zebrafish reference genome sequence and its relationship to the human genome. *Nature* **496,** 498–503 (2013).

20. Panula, P. *et al.* The comparative neuroanatomy and neurochemistry of zebrafish CNS systems of relevance to human neuropsychiatric diseases. *Neurobiol. Dis.* **40,** 46–57 (2010).

21. Randlett, O. *et al.* Whole-brain activity mapping onto a zebrafish brain atlas. *Nat. Methods* **12,** 1039–1046 (2015).

22. Beretta, C. A., Dross, N., Guiterrez-Triana, J. A., Ryu, S. & Carl, M. Habenula circuit development: Past, present, and future. *Front. Neurosci.* **6,** 1–10 (2012).

23. Li, K. *et al.* βCaMKII in Lateral Habenula Mediates Core Symptoms of Depression. *Science (80-.).* **341,** 1016–1020 (2013).

24. Agetsuma, M. *et al.* The habenula is crucial for experience-dependent modification of fear responses in zebrafish. *Nat. Neurosci.* **13,** 1354–1356 (2010).

25. Mathuru, A. S. & Jesuthasan, S. The medial habenula as a regulator of anxiety in adult zebrafish. *Front. Neural Circuits* **7,** 5–7 (2013).

26. Kalueff, A. V. *et al.* Towards a Comprehensive Catalog of Zebrafish Behavior 1.0 and Beyond. *Zebrafish* **10,** 70–86 (2013).

27. Best, J. D.; Alderton, W. K. Zebrafish: An in vivo model for the study of neurological diseases. *Neuropsychiatr. Dis. Treat.* **4,** 567–576 (2008).

28. Kimmel, C. B., Ballard, W. W., Kimmel, S. R., Ullmann, B. & Schilling, T. F. Stages of Embryonic Development of the Zebrafish. *Dev. Dyn.* **10,** 253–310 (1995).

29. Selderslaghs, I. W. T., Van Rompay, A. R., De Coen, W. & Witters, H. E. Development of a screening assay to identify teratogenic and embryotoxic chemicals using the zebrafish embryo. *Reprod. Toxicol.* **28,** 308–320 (2009).

30. Rihel, J. & Schier, A. F. Behavioral screening for neuroactive drugs in zebrafish. *Dev. Neurobiol.* **72,** 373–385 (2012).

31. Padilla, S. *et al.* Zebrafish developmental screening of the ToxCast™ Phase I chemical library. *Reprod. Toxicol.* **33,** 174–187 (2012).

32. Vaz, R. L., Outeiro, T. F. & Ferreira, J. J. Zebrafish as an animal model for drug discovery in Parkinson's disease and other movement disorders: A systematic review. *Front. Neurol.* **9,** (2018).

33. Bretaud, S., Lee, S. & Guo, S. Sensitivity of zebrafish to environmental toxins implicated in Parkinson's disease. *Neurotoxicol. Teratol.* **26,** 857–864 (2004).

34. McKinley, E. T. *et al.* Neuroprotection of MPTP-induced toxicity in zebrafish dopaminergic neurons. *Mol. Brain Res.* **141,** 128–137 (2005).

35. Lam, C. S., Korzh, V. & Strahle, U. Zebrafish embryos are susceptible to the dopaminergic neurotoxin MPTP. *Eur. J. Neurosci.* **21,** 1758–1762 (2005).

36. Thirumalai, V. & Cline, H. T. Endogenous Dopamine Suppresses Initiation of Swimming in Prefeeding Zebrafish Larvae. *J. Neurophysiol.* **100,** 1635–1648 (2008).

37. Wen, L. *et al.* Visualization of monoaminergic neurons and neurotoxicity of MPTP in live transgenic zebrafish. *Dev. Biol.* **314,** 84–92 (2008).

38. Sallinen, V. *et al.* MPTP and MPP+ target specific aminergic cell populations in larval zebrafish. *J. Neurochem.* **108,** 719–731 (2009).

39. Chong, C. M. *et al.* Discovery of a novel neuroprotectant, BHDPC, that protects against MPP+/MPTP-induced neuronal death in multiple experimental models. *Free Radic. Biol. Med.* **89,** 1057–1066 (2015).

40. Embryos, S. Z. *et al.* Neurotoxicity of the Parkinson Disease-Associated Pesticide Ziram Is Synuclein-Dependent in Zebrafish Embryos. **1766,** 1766–1775 (2016).

41. Cao, F. *et al.* Developmental toxicity of the fungicide ziram in zebrafish (Danio rerio). *Chemosphere* **214,** 303–313 (2019).

42. Burgess, H. A. & Granato, M. Modulation of locomotor activity in larval zebrafish during light adaptation. *J. Exp. Biol.* **210,** 2526–2539 (2007).

43. MacPhail, R. C. *et al.* Locomotion in larval zebrafish: Influence of time of day, lighting and ethanol. *Neurotoxicology* **30,** 52–58 (2009).

44. Irons, T. D., MacPhail, R. C., Hunter, D. L. & Padilla, S. Acute neuroactive drug exposures alter locomotor activity in larval zebrafish. *Neurotoxicol. Teratol.* **32,** 84–90 (2010).

45. Irons, T. D.; Kelly, P.; Hunter, D. L.; MacPhail, R. C.; Padilla, S. Acute Administration of Dopaminergic Drugs has Differential Effects on Locomotion in Larval Zebrafish. *Pharmacol Biochem Behav.* **103,** 792–813 (2014).

46. Jarema, Kimberly A.; Hunter, Deborah L.; Shaffer, Rachel M.; Behl, Mamta; Padilla, S. Acute and developmental behavioral effects of flame retardants and related chemicals in zebrafish. *Neurotoxicol. Teratol.* **52,** 194–209 (2015).

47. Padilla, S., Hunter, D. L., Padnos, B., Frady, S. & MacPhail, R. C. Assessing locomotor activity in larval zebrafish: Influence of extrinsic and intrinsic variables. *Neurotoxicol. Teratol.* **33,** 624–630 (2011).

48. Díaz-Casado, M. E. *et al. In Vivo* Determination of Mitochondrial Respiration in 1-Methyl-4-Phenyl-1,2,3,6-Tetrahydropyridine-Treated Zebrafish Reveals the Efficacy of Melatonin in Restoring Mitochondrial Normalcy. *Zebrafish* **15,** 15–26 (2018).

49. Costello, S., Cockburn, M., Bronstein, J., Zhang, X. & Ritz, B. Parkinson's disease and residential exposure to maneb and paraquat from agricultural applications in the central valley of California. *Am. J. Epidemiol.* **169,** 919–926 (2009).

50. Bartlett, D. W. *et al.* The strobilurin fungicides. *Pest Manag. Sci.* **58,** 649–662 (2002).

51. Blesa, J. & Przedborski, S. Parkinson's disease: animal models and dopaminergic cell vulnerability. *Front. Neuroanat.* **8,** 1–12 (2014).

52. Chou, A. P. *et al.* Ziram causes dopaminergic cell damage by inhibiting E1 ligase of the proteasome. *J. Biol. Chem.* **283,** 34696–34703 (2008).

53. Zhang, J. *et al.* Manganese ethylene-bis-dithiocarbamate and selective dopaminergic neurodegeneration in rat: A link through mitochondrial dysfunction. *J. Neurochem.* **84,** 336–346 (2003).

54. Cao, F. *et al.* Developmental neurotoxicity of maneb: Notochord defects, mitochondrial dysfunction and hypoactivity in zebrafish (Danio rerio) embryos and larvae. *Ecotoxicol. Environ. Saf.* **170,** 227–237 (2019).

55. Becker, W. F.; Jagow, G. V.; Anke, T.; Steglich, W. Oudemansin, strobilurin A, strobilurin B and myxothiazol: new inhibitors of the bc1 segment of the respiratory chain with an E-B-methoxyacrylate system as common structural element. *FEBS Lett.* **132,** 329–333 (1981).

56. Jagow, G. Von, Gribble, G. W. & Trumpower, B. L. Mucidin and Strobilurin A Are Identical and Inhibit Electron Transfer in the Cytochrome bc1Complex of the Mitochondrial Respiratory Chain at the Same Site as Myxothiazol. *Biochemistry* **25,** 775–780 (1986).

57. Li, H. *et al.* Developmental toxicity, oxidative stress and immunotoxicity induced by three strobilurins (pyraclostrobin, trifloxystrobin and picoxystrobin) in zebrafish embryos. *Chemosphere* **207,** 781–790 (2018).

58. Jia, W., Mao, L., Zhang, L., Zhang, Y. & Jiang, H. Effects of two strobilurins (azoxystrobin and picoxystrobin) on embryonic development and enzyme activities in juveniles and adult fish livers of zebrafish (Danio rerio). *Chemosphere* **207,** 573–580 (2018).

59. Zhang, C. *et al.* Acute and subchronic toxicity of pyraclostrobin in zebrafish (Danio rerio). *Chemosphere* **188,** 510–516 (2017).

60. Díaz-Casado, M. E. *et al.* Melatonin rescues zebrafish embryos from the parkinsonian phenotype restoring the parkin/PINK1/DJ-1/MUL1 network. *J. Pineal Res.* 96–107 (2016). doi:10.1111/jpi.12332

61. Li, C. *et al.* Pinostrobin Exerts Neuroprotective Actions in Neurotoxin-Induced Parkinson's Disease Models through Nrf2 Induction. *J. Agric. Food Chem.* **66,** 8307–8318 (2018).

62. Anichtchik, Oleg V.; Kaslin, Jan; Peitsaro, Nina; Scheinin, Mika; Panula, P. Neurochemical and behavioural changes in zebrafish Danio rerio after systemic administration of 6-hydroxydopamine and 1-methyl-4-phenyl-1,2,3,6-tetrahydropyridine. *J. Neurochem.* **88,** 443–453 (2004).

63. Xu, J. & Xie, F. kang. α- and β-Adrenoceptors of zebrafish in melanosome movement: A comparative study between embryo and adult melanophores. *Biochem. Biophys. Res. Commun.* **405,** 250–255 (2011).

CHAPTER 4. PH- AND TEMPERATURE-DEPENDENT PEPTIDE BINDING TO THE LACTOCOCCUS LACTIS OLIGOPEPTIDE-BINDING PROTEIN A MEASURED WITH A FLUORESCENCE ANISOTROPY ASSAY

*This work has been published and is reproduced with permission from Norcross, S., Sunderraj, A., Tantama, M. pH- and Temperature-Dependent Peptide Binding to the *Lactococcus Lactis* Oligopeptide-Binding Protein A Measured with a Fluorescence Anisotropy Assay. *ACS Omega* **4,** 2812–2822 (2019).

4.1 Abstract

Bacterial ATP-binding cassette (ABC) transporters are a superfamily of transport systems involved in the import of various molecules including amino acids, ions, sugars and peptides. In the lactic acid bacteria *Lactococcus lactis*, the oligopeptide-binding protein A (OppA) binds peptides for import to support nitrogen metabolism and cell growth. The OppA protein is of great interest because it can bind peptides over a broad variety of lengths and sequences, however current methods to study peptide binding have employed low throughput, endpoint, or low dynamic range techniques. Therefore, in this study we developed a fluorescence anisotropy-based peptide-binding assay that can be readily employed to quantify OppA function. To test the utility of our assay, we characterized the pH dependence of oligopeptide binding because *L. lactis* is commonly used in fermentation and often must survive in low pH environments caused by lactic acid export. We determined that OppA affinity increases as pH or temperature decreases, and circular dichroism spectroscopy further indicated that acidic conditions increase the thermal stability of the protein, increasing the unfolding transition temperature by 10°C from pH 8 to pH 6. Thus, our fluorescence anisotropy assay provides an easy technique to measure peptide binding, and it can be used to understand molecular aspects of OppA function under stress conditions experienced during fermentation and other biotechnology applications.

4.2 Introduction

The lactic acid bacteria *Lactococcus lactis* is vital to the dairy industry and has become a synthetic biology platform for recombinant protein production, metabolic engineering, as well as

the development of probiotics and vaccines[1–8]. Like many bacteria, *L. lactis* relies on extracellular peptides as a major source of nutrients to support carbon and nitrogen metabolism, and peptide transport plays an important role in bacterial growth and survival. In general, bacteria can utilize proton-coupled transporters and ATP-binding cassette (ABC) type transporters to import di-, tri-, and oligopeptides. For *L. lactis*, which is a branched-chain amino acid auxotroph, the oligopeptide ABC transporter is necessary for growth on natural substrates such as milk casein peptides[9–14]. The oligopeptide ABC transporter is a multi-subunit complex consisting of two transmembrane proteins (OppB and OppC), two ATP-binding proteins (OppD and OppF), and a substrate-binding protein (OppA).[12] The *L. lactis* OppA is part of a superfamily of substrate-binding proteins that share similar overall tertiary structure and domain organization[15–17].

OppA is particularly interesting because it has a broad capacity to bind peptides of varying length and sequence[18–25] unlike other substrate-binding proteins that have high specificity for ligands such as metal cofactors and sugars[15–17,26,27]. The crystal structures of several OppA proteins from diverse bacteria have been solved, including that of *L. lactis* OppA[17,28–31]. In general, substrate-binding proteins consist of two domains connected by a hinge region with the substrate-binding pocket located between the two domains. Upon binding substrate, the protein undergoes a conformational change from open to closed as it clamps down on the substrate, which is known as the 'Venus flytrap' mechanism[26,27,30,32]. The OppA proteins also undergo the canonical substrate-dependent conformational change (Figure 4.1), but they have an additional third domain that increases the size of the binding pocket, which classifies them as a cluster C substrate-binding proteins[28–30]. The *L. lactis* OppA accepts peptides ranging from 4 to 35 residues in length with a preference for hydrophobic and basic ligands. Overall it has relatively low specificity for peptide sequence, which is likely because hydrogen bonds are almost exclusively formed between the protein and the peptide backbone and not with peptide side chains[18–25]. The crystal structures of *L. lactis* OppA reveal that the peptide-binding site is a large, aqueous cavity with a single hydrophobic pocket that can accommodate a bulky residue. Crystal structures with peptide bound show that the termini of peptides are not in fixed positions and peptides of same length and composition, but differing sequences can bind different registers[29,31]. Thus, peptide selection is based on composition rather than exact sequence, which allows OppA to import a wide range of peptides for nutrients.

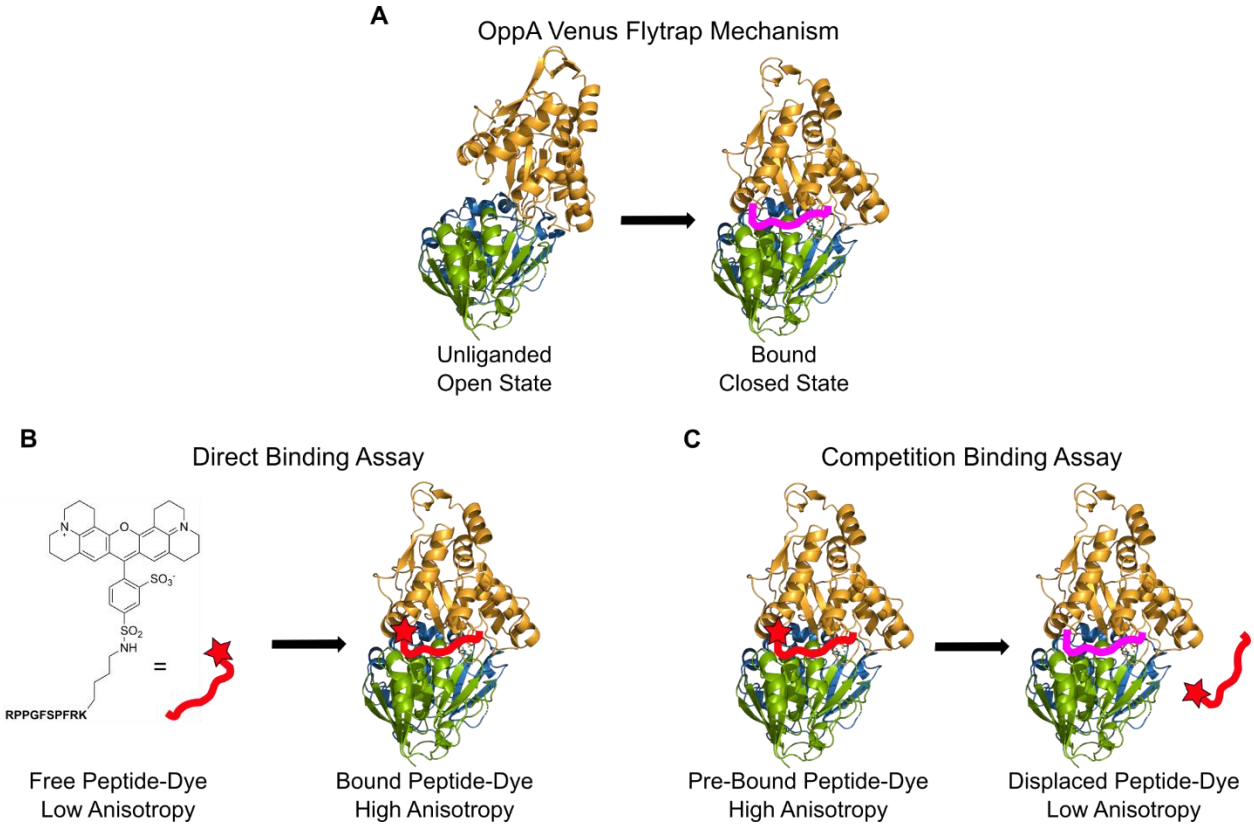

Figure 4.1 Fluorescence anisotropy peptide binding assays used to quantify relative changes in *L. lactis* OppA binding affinity.

(A) Substrate peptide binding causes a "Venus flytrap" conformational change from an open state (PDB 3DRK) to a closed state (PDB 3DRG). (B) A dye-labeled peptide rotates freely in solution with low fluorescence anisotropy. Once bound to OppA, the fluorescent peptide-OppA complex rotates more slowly, causing an increase in fluorescence anisotropy. (C) For competition binding assays, the fluorescent peptide is pre-bound to OppA. Unlabeled peptide displaces the fluorescent peptide, causing a decrease in fluorescence anisotropy. Green, blue, and orange indicate lobes Ia, Ib, and II in the protein structures. Unlabeled peptide is pink, and dye-labeled peptide is shown in red with a star.

While the specificity of OppA peptide binding and its role in nutrient import have been well established, no studies have been performed to characterize the peptide binding properties of OppA under stress conditions. Lactic acid bacteria frequently experience stress conditions particularly when used in food fermentation[33]. *L. lactis* exhibits optimal growth at pH 6.3 and at 30°C, thus stress conditions could include both pH and temperature changes that still reside within mesophilic ranges[34,35]. Furthermore, several studies have shown differential expression of genes involved in amino acid metabolism under stress conditions, including and implicating OppA in stress response.[36–38] Thus, in this study we developed a fluorescence anisotropy assay that can be

used to measure the effects of pH and temperature on peptide binding to the *L. lactis* OppA protein. To quantify relative changes in OppA function and structure, we used a combination of our fluorescence anisotropy peptide binding assays and circular dichroism. We discovered that increased peptide affinity under acidic conditions correlates with increased structural stability and neutralization of surface charge within the substrate-binding pocket, pointing to a potential molecular adaptation to the optimal growth conditions for *L. lactis*.

4.3 Materials and Methods

4.3.1 Reagents and Materials

Chemicals and media were purchased from Fisher Scientific, Sigma and Formedium. High-fidelity master mix for Gibson Assembly was from New England Biolabs (Cat# M0492). Bradykinin peptide (RPPGFSPFR) was purchased from and HPLC purified (98% purity) by Bachem. All other unlabeled peptides were custom synthesized and HPLC purified (>95% purity) by GenScript. The sulforhodamine 101 labeled bradykinin peptides (SR101-RPPGFSPFR and RPPGFSPFRK-SR101) were synthesized and HPLC purified (>90% purity) by Anaspec.

4.3.2 Plasmid Construct

The *Lactococcus lactis* oligopeptide-binding protein A (OppA) amino acid sequence is from subspecies cremoris MG1363 (GenBank accession AAO63470.1). The N-terminal signal peptide for palmitoylation and surface tethering was removed similar to previous studies (Figure 4.2).[21,22,29] The nucleotide sequence was optimized to minimize hairpins for cloning and was synthesized as a gBlock by Integrated DNA Technologies (IDT). The OppA gBlock was cloned into a pRSETB vector by Gibson Assembly for bacterial expression and purification (Figure 4.3).

MNKLKVTLLASSVVLAATLLSACGSNQSSSTSTK

Figure 4.2 N-terminal sequence removed from the *Lactococcus lactis* OppA to prevent palmitoylation, where C is the N-palmitoyl cysteine.

MRGSHHHHHHGMASMTGGQQMGRDLYDDDDKDPTMKLKAGNFDVAYQNPDKAIKG
GNLKVAYQSDSPMKAQWLSGLSNDATFATMSGPGGGQDGLFFTDSGFKFIKGGAADV
ALDKESKTATITLRKDLKWSDGSEVTAKDYEFTYETIANPAYGSDRWTDSLANIVGLSD
YHTGKAKTISGITFPDGENGKVIKVQFKEMKPGMTQSGNGYFLETVAPYQYLKDVAPK
DLASSPKTTTKPLVTGPFKPENVVAGESIKYVPNPYYWGEKPKLNSITYEVVSTAKSVA
ALSSSKYDIINGMVSSQYKQVKNLKGYKVLGQQAMYISLMYYNLGHYDAKNSINVQD
RKTPLQDQNVRQAIGYARNVAEVDNKFSNGLSTPANSLIPPIFKQFTSSSVKGYEKQDLD
KANKLLDEDGWKLNKSTGYREKDGKELSLVYAARVGDANAETIAQNYIQQWKKIGVK
VSLYNGKLMEFNSWVDHMTTPPGANDWDITDGSWSLASEPSQQDLFSAAAPYNFGHF
NDSEITKDLNDIDSAKSENPTYRKAAFVKYQEDMNKKAYVIPTNFMLNYTPVNKRVVG
MTLDYGAMNTWSEIGVSSAKLATK

Figure 4.3 Protein sequence for the OppA construct. Color: 6x His tag and T7 leader from pRSETB vector, OppA.

4.3.3 OppA Expression and Purification

Polyhistidine-tagged protein was expressed in BL21(DE3) *E. coli* in Auto Induction Media (AIM) purchased from ForMedium (Cat# AIMLB0205). Heterologous expression was used to avoid co-purification with endogenous *L. lactis* peptides, and there was no evidence that endogenous peptides interfered with any assays reported here. First, single colonies were picked and used to inoculate 4 mL Luria broth (LB) starter cultures. Starter cultures were grown overnight with continuous shaking at 37°C and then adjusted to an OD600 of 0.6 with LB. Large AIM cultures (250 mL) were inoculated with 2.5 mL of 0.6 OD600 LB starter cultures and grown at room temperature (RT) for ~65 hrs with continuous shaking at 160 rpm. Cultures were pelleted at 10,00xg for 15 minutes and lysed by sonication. First, pellets were frozen at -80°C and thawed at RT twice. Pellets were resuspended in Tris Buffer (50 mM Tris HCl, 300 mM NaCl, 10% v/v glycerol, 15 mM imidazole, pH 8.0) with 0.2 mg/mL lysozyme, 0.1% v/v Triton X, 1 mM PMSF, 1 mM DTT and rotated end-over-end at RT for 20 minutes. Lysate was sonicated (QSonica, LLC model# Q125) on ice for 1 minute (pulse 2 seconds on with 2 seconds off, 80% amplitude) with 2 minutes rest, and sonication was repeated two more times. Lysate was pelleted at 30,000xg for 30 minutes, and the supernatant was filtered through a 0.45 μm low protein-binding Millex syringe filter, Durapore® (Cat# SLHV033NS). Protein was purified in Tris Buffer by nickel affinity chromatography using a GE Healthcare HiTrap™ IMAC HP column (Cat# 45-000-163) loaded

with 100 mM Ni^{2+} and eluted by gradient with 15 - 500 mM imidazole on a GE Healthcare AKTA purifier. Eluted protein was collected and dialyzed in Sodium Phosphate Buffer (25 mM sodium phosphate, 150 mM NaCl, 10% glycerol, pH 7.0). Dialyzed protein was concentrated to 1 mL with an EMD Millipore™ Amicon™ Ultra centrifugal filter with 10,000 MWCO and purified by size exclusion chromatography (SEC) on tandem GE Superdex 200 Increase 10/300 GL columns (product # 28990944, total bed volume = ~48 mL) in Sodium Phosphate Buffer. Concentration of the purified protein was determined by absorbance at 280 nm using an extinction coefficient of 99140 $M^{-1}*cm^{-1}$ calculated using the Northwestern University Peptide Properties Calculator (http://biotools.nubic.northwestern.edu/proteincalc.html#helpexco).

4.3.4 Fluorescence Anisotropy Assay

For direct dose response binding, 100 μL of 1.5 μM dye-labeled bradykinin (SR101-RPPGFSPFR or RPPGFSPFRK-SR101) was added to each well in a 96-well non-binding microplate (VWR, 89089-582). Purified OppA (50 μL) was added to each well at final concentrations varying from 0.01 to 100 μM and incubated at the desired temperature for at least 30 minutes to reach equilibrium. Unless otherwise noted, all anisotropy assays were performed at 30°C in Assay Buffer (25 mM sodium phosphate, 150 mM NaCl, 10% glycerol, 1 mM DTT, 1x SIGMA*FAST* protease inhibitor cocktail, 0.05% v/v TWEEN, pH 6.0). The assay proved robust and adaptable to different assay conditions, and protease inhibitors and detergent did not interfere for example. For all protein assays, at least two separately expressed and purified batches of OppA were used. Fluorescence anisotropy was measured using a BioTek Synergy H4 microplate reader with a Chroma 585 nm single edge dichroic beamsplitter (T585Ipxr), 575/15 nm excitation filter and 620/15 nm emission filter. For assays performed at 18 and 24°C, the microplate reader was moved into a 4°C cold room for constant cooling, while the instrument was set to the desired temperature for heating.

For competition dose response binding, a mixture of 1 μM bradykinin-SR101 and 15 μM OppA was prepared, and 150 μL of the mixture was added to each well in a 96-well non-binding microplate. Unlabeled peptide (50 μL) was added to each well at final concentrations varying from 0.1 to 2500 μM (1 to 10,000 μM for leu-enkephalin) and incubated at the desired temperature for at least 1 hour to reach equilibrium. Fluorescence anisotropy was measured as described above.

Anisotropy (r) was calculated using the intensity of parallel ($I_{\parallel}$) and perpendicular ($I_{\perp}$) light emitted as follows: $r = \frac{I_{\parallel} - I_{\perp}}{I_{\parallel} + 2 \cdot I_{\perp}}$. Anisotropy was plotted against the log concentration of protein for the direct dose response binding and log concentration of unlabeled peptide for competition dose response binding. A dose response curve fit was performed in OriginPro to determine the dissociation constant (K) or the half maximal inhibitory concentration (IC_{50}).

We directly fitted competitor dose response data to a two ligand complete competition binding model because the Cheng-Prusoff equation is not appropriate. The Cheng-Prusoff equation ($IC_{50} = K_i \cdot (1 + [S]/K_M)$) is used in ideal cases in which it is known *a priori* that the competitor is not high affinity. In our competition binding assays, we make no assumption about the binding affinity of the unlabeled competitor. Furthermore, we designed our assay conditions such that the concentration of the OppA protein is in excess of the labeled bradykining-SR101 (BK-SR101) peptide in order to achieve approximately 50% occupancy for good sensitivity and a large dynamic range for fluorescence anisotropy changes. Therefore, we fitted our competition dose-response data directly to the complete competitive binding model described by Wang[39] and Roehrl *et al.*[40]

We define in molar units: P, the concentration of unbound free OppA protein; L, the concentration of unbound free labeled BK-SR101 peptide; U, the concentration of unbound free unlabeled competitor; PL, the concentration of the labeled OppA-(BK-SR101) complex; PU, the concentration of the unlabeled OppA-competitor complex; $P_T = P + PU + PL$, the total OppA protein concentration; $L_T = L + PL$, the total labeled BK-SR101 peptide concentration; $U_T = U + PU$, the total unlabeled competitor concentration; K_L, the dissociation constant for the labeled OppA-(BK-SR101) complex; K_U, the dissociation constant for the unlabeled OppA-competitor complex. As previously described by Wang and Roehrl *et al*[39,40], an analytical solution can be written for the fraction of labeled BK-SR101 peptide that is bound to the OppA protein (F_{PL}):

$$F_{PL} = \frac{PL}{P_T} = \frac{(2\sqrt{(d^2 - 3e)} \cdot \cos(\theta/3) - d)}{3K_L + (2\sqrt{(d^2 - 3e)} \cdot \cos(\theta/3) - d)}$$

$$d = K_L + K_U + L_T + U_T - P_T$$

$$e = (U_T - P_T) \cdot K_L + (L_T - P_T) \cdot K_U + K_L \cdot K_U$$

$$f = -K_L \cdot K_U \cdot P_T$$

$$\theta = \cos^{-1}\left(\frac{-2d^3 + 9de - 27f}{2\sqrt{(d^2 - 3e)^3}}\right)$$

For our assay conditions at each pH and temperature, we experimentally determined the minimum anisotropy, r_{min}, of the labeled BK-SR101 alone. We also determined the maximum anisotropy, r_{max}, of the labeled OppA-(BK-SR101) complex without any competitor present. Therefore, we can write a standard saturation binding equation for the total anisotropy (r):

$$r = r_{min} + (r_{max} - r_{min}) \cdot F_{PL}$$

By rearranging this equation, anisotropy from the competitor dose-response experiments was converted to the fraction bound labeled BK-SR101:

$$F_{PL} = \frac{r - r_{min}}{r_{max} - r_{min}}$$

We used the Matlab non-linear least squares fitting function lsqcurvefit to fit our competition dose-response data and determine the unlabeled competitor dissociation constant (referred to as the "fitted K_U"). We compared the Trust Region Reflective and Levenberg-Marquardt optimization algorithms. Both algorithms produced similar results, but the Trust Region Reflective converged more robustly, and therefore we report results using the default Trust Region Reflective algorithm in Table 4.1 and Table 4.3. Dose response data for each replicate were fitted (Figures 4.8 and 4.11), and then the fitted K_U values were averaged and reported in Table 4.1 and Table 4.3.

We achieve greater accuracy in determining K_U by directly fitting dose-response data to the complete competition binding model, especially when the Cheng-Prusoff equation is not valid. However, we expect that there will still be limitations to this fitting approach determined by experimental assay parameters. In particular, we expect that when the true competitor affinity is

very high beyond a certain threshold, the fitted K_U values will become indistinguishable. In order to determine this threshold (effectively the lower limit of fitted K_U estimation), we simulated anisotropy dose-response data in which we varied the theoretical K_U value for the unlabeled competitor. We then fit the simulated data and determined at what simulated K_U values the fitted K_U values no longer reliably estimate the simulated K_U values. Across different pH and temperature, the OppA-(BK-SR101) binding affinity was approximately K_L = 10 µM, which we set as an experimental constant. We therefore explored K_U values ±3 $\log_{10}$ units around K_L by simulating data for $K_U = 10^{-8}$ M to 10^{-2} M at 0.1 $\log_{10}$ unit increments. We also set experimental assay parameters for total OppA protein concentration P_T = 11.25 µM, total labeled BK-SR101 peptide concentration L_T = 0.75 µM, and the approximate competitor peptide concentration range $U_T = 10^{-8}$ M to 10^{-2} M. The standard deviation for our replicate anisotropy measurements was approximately 2% of the mean, and for a normal distribution, the full width at half maximum (FWHM) is $2\cdot(2\ln2)^{1/2}$ times the standard deviation. Therefore, to achieve an approximate 5% FWHM, we added normally distributed random numbers scaled to a maximum percent error range of -10% to 10% to the simulated data. Using these experimental parameters, for each theoretical K_U value we simulated 1000 dose-response data sets and then fitted the simulated data to determine the fitted K_U value (Figure 4.4). We then analyzed the relationship between the fitted K_U versus the simulated K_U (Figure 4.4) and determined that below a simulated K_U value of 10^{-7} M, fitting became more error prone. We then estimated the probability that the fitted K_U was within an N-fold range of the simulated K_U (Figure 4.4) and found that for a simulated K_U value of 10^{-7} M, there was only a 50% probability that the fitted K_U would be within 2-fold of the simulated K_U value. Therefore, we made the conservative decision that for any experimental data that results in a fitted $K_U \leq 10^{-7}$ M, we consider it a "high affinity" competitor and we report $K_U \leq 10^{-7}$ M (Table 4.3).

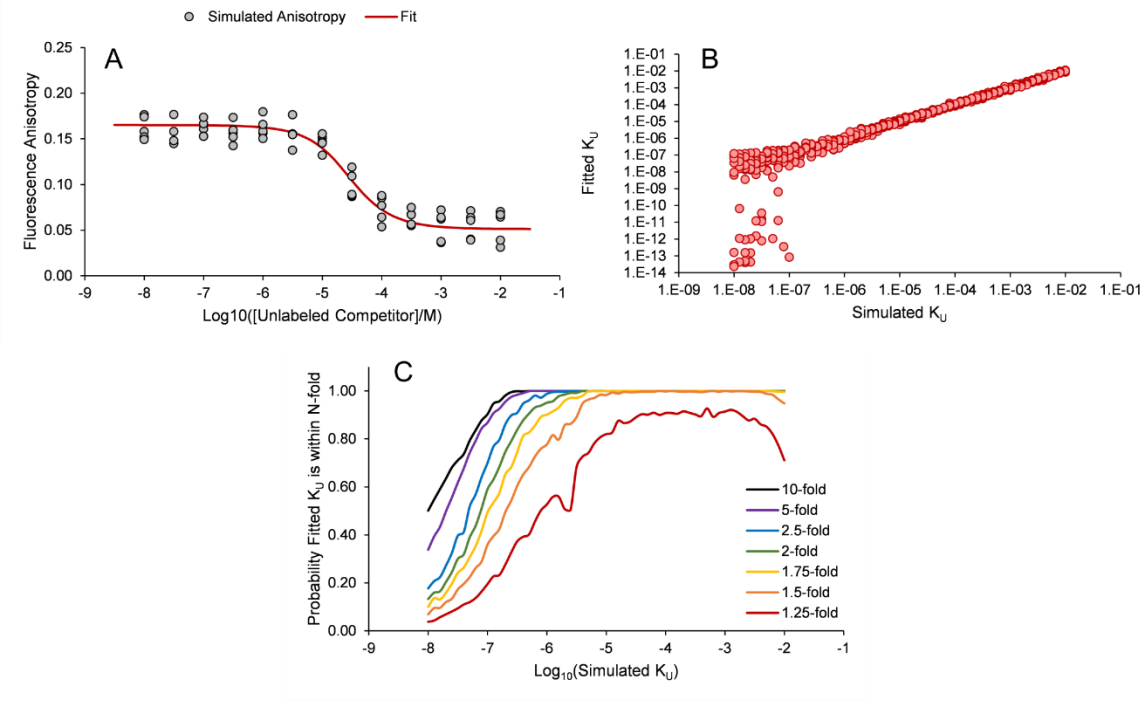

Figure 4.4 Determining the limit of K_U estimation under experimental conditions.

(A) An example of 1 simulated dose-response data set: simulated K_U = 10.0 μM; fitted K_U = 9.6 ± 3.2 μM (mean ± 95% confidence interval). (B) The fitted K_U values from 1000 simulated data sets is plotted against the simulated K_U value. Below a simulated K_U value of 0.1 μM, fitting and estimation cannot distinguish between K_U values for high affinity competitors. (C) The 1000 simulated data sets were analyzed to estimate the probability that the fitted K_U valued would fall within N-fold of the true simulated K_U value.

4.3.5 Circular Dichroism Spectroscopy

Pure OppA was diluted to 2 μM in 25 mM sodium phosphate buffer (no NaCl or glycerol due to CD absorbance) at the desired pH with or without 100 μM bradykinin. 600 μL diluted protein was added to a quartz cuvette with a 2 mm path length (Starna Cells, 18F-Q-10). CD absorbance was measured from 190 – 260 nm on a Jasco J-1500 circular dichroism spectrophotometer using a 50 nm/min scan speed, 1.0 nm data pitch,1.0 nm bandwidth and 1 s digital integration time (D.I.T.).

Mean residue ellipticity ($[\theta]_{mrw}$) was calculated as described in Kelly et al[41]. First, mean residue weight (MRW) of OppA was calculated using the following equation: $MRW = \frac{M}{(N-1)}$, where M is the molar mass of the protein in Da, N is the number of amino acids in the protein, and

the number of peptide bonds is N-1. Here, our *Lactococcus lactis* OppA molar mass is 66419.5 Da and is composed of 601 amino acids (Figure 4.3), which gives an MRW of 110.7 Da. Then, $[\theta]_{mrw}$ was calculated using the following equation: $[\theta]_{mrw,\lambda} = \frac{MRW*\theta_\lambda}{10*l*c}$, where θ_λ is the observed ellipticity in degrees, l is the pathlength in cm and c is the concentration in g/mL.

To measure thermal denaturation, the temperature was ramped from 4 - 74°C (to 79°C for OppA + bradykinin at pH 6), increasing 1 degree/min measuring the full spectrum every 5°C with a 2-minute wait time before measurement for equilibration. Melting temperature (Tm) was determined by plotting the mean residue ellipticity at 222 nm against the temperature and fitting to a Boltzmann Distribution in OriginPro.

4.4 Results

4.4.1 Development of a Fluorescence Anisotropy Assay for OppA Peptide Binding

To quantify relative differences in OppA peptide affinity, we developed fluorescence anisotropy peptide binding assays because they are non-radioactive solution-state assays that offer high signal over background with a good dynamic range and ease of execution[42–44]. We based our assay on the binding of a sulforhodamine 101 (SR101)-labeled peptide to OppA (Figure 4.1). We chose SR101 because it is commercially-available for custom dye-modified peptide synthesis and it is water-soluble, bright, and has a fluorescence lifetime of ~4.2 ns that makes it sensitive to polarization changes upon binding large molecular weight proteins. As described below, SR101 was highly effective as an anisotropy reporter, and therefore we did not test other fluorophores. However, in principle our assay should work with other dyes.

We then chose to conjugate SR101 to peptide bradykinin (RPPGFSPFR) because it has previously been used to characterize peptide binding to OppA. Bradykinin is a peptide hormone that is vital to endocrine signaling throughout mammalian tissues, including the gut. In theory, it is also an example of an endogenous peptide that could be used as a nutrient, though it is not clear that *L. lactis* would encounter high concentrations of bradykinin in the gut lumen. For the purpose of this study, the primary reason we chose to use bradykinin is because bradykinin has been used extensively in other functional assays for the Opp-transport system[23,25,45,46]. Furthermore, we also chose to label the bradykinin because it is the highest affinity ligand reported for *L. lactis* OppA

(K_D = 0.1 μM)[21], which we hypothesized would mitigate any loss of affinity caused by conjugation to SR101. As demonstrated in our results, the SR101-conjugated bradykinin provided excellent anisotropy detection characteristics, and therefore we did not screen other peptides to label.

We initially tested OppA binding using bradykinin that was labeled on either its N or C-terminus (SR101-RPPGFSPFR and RPPGFSPFRK-SR101). The C-terminal configuration included a lysine residue that was necessary for coupling to the dye (Figure 4.1), (Figure 4.5). In order to determine the affinities of the two different dye-labeled peptide configurations, direct-binding dose response curves were performed with varying concentrations of OppA (Figure 4.6). The affinities of OppA for the N and C-terminally labeled bradykinin were determined to be 45 ± 3 μM and 13.1 ± 0.7 μM, respectively (mean ± stdev, n=3). The higher affinity for the C-terminally labeled peptide aligns well with previous studies that showed that OppA tolerates large bulky groups on the C-terminus of a peptide, but not the N-terminus[22]. Additionally, the crystal structure of OppA in complex with bradykinin reveals that the entire peptide can be accommodated within the binding pocket, with the N-terminus buried more deeply within the binding pocket compared to the C-terminus[29]. The additional lysine residue on the C-terminally labeled peptide may also contribute to the higher affinity relative to the N-terminally labeled peptide. The higher affinity C-terminally labeled peptide, referred to as "bradykinin-SR101", was selected for use in subsequent assays because of its greater binding affinity, which provided good sensitivity to binding over a range of sub-micromolar to millimolar concentrations. Using bradykinin-SR101, our assay exhibited a dynamic range with a maximal increase of 0.201 ± 0.002 in fluorescence anisotropy between the free and OppA-bound states, and reproducibility was excellent across independent protein preparations (Figure 4.6).

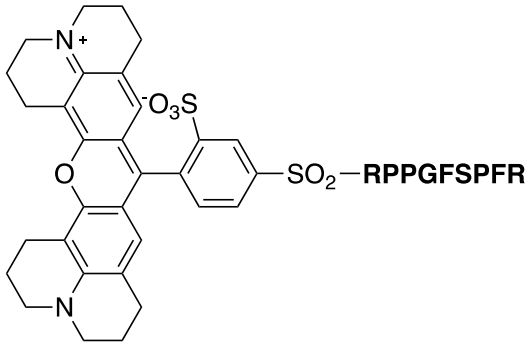

Figure 4.5 N-terminally labeled bradykinin peptide (SR101-bradykinin) structure, where the bradykinin peptide sequence is shown in bold (RPPGFSPFR).

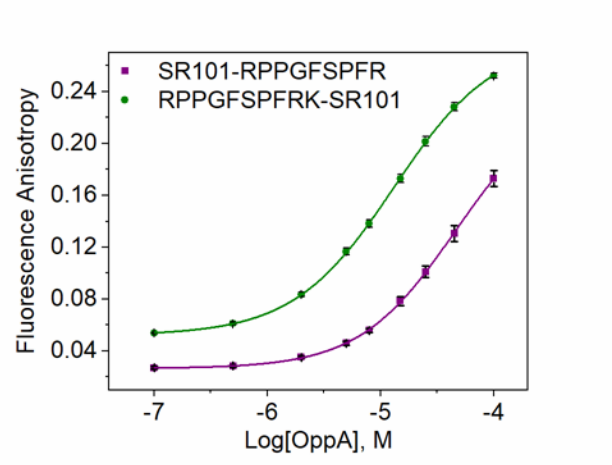

Figure 4.6 Direct binding to *L. lactis* OppA measured by fluorescence anisotropy.

Bradykinin labeled with sulforhodamine 101 on the N-terminus (SR101-RPPGFSPFR) exhibited lower affinity for OppA compared to bradykinin labeled on the C-terminus (RPPGFSPFRK-SR101). Lines show the average fit for n = 3. Error bars are stdev.

We next validated that the fluorescent dye-labeled bradykinin-SR101 binds to the same site as unlabeled peptides using fluorescence anisotropy competition assays (Figure 4.1). After optimizing assay conditions for sensitivity in our system, we used a pre-bound complex of OppA and bradykinin-SR101 at approximately 50% saturation and a half-max anisotropy in the absence of competitor peptide. Typically, 50%-80% saturation provides an excellent signal window because there is sufficient anisotropy to be sensitive to probe displacement while avoiding experimental uncertainty and signal dampening caused by complete saturation[47]. In this competition assay, the addition of unlabeled competitor peptide results in a decrease in the anisotropy when the OppA-bound dye-labeled peptide is displaced. As expected for peptides that bind to the same site, unlabeled bradykinin was able to completely displace pre-bound bradykinin-SR101 (Figure 4.7). We additionally validated that another reported high affinity peptide derived from casein was able to completely displace bradykinin-SR101. Furthermore, the low affinity peptide, neuropeptide S, was able to partially displace bradykinin-SR101 within the tested peptide concentration range, which was limited by peptide solubility (Figure 4.7). Thus, our competition assays show that bradykinin-SR101 exhibits a normal mode of binding to OppA.

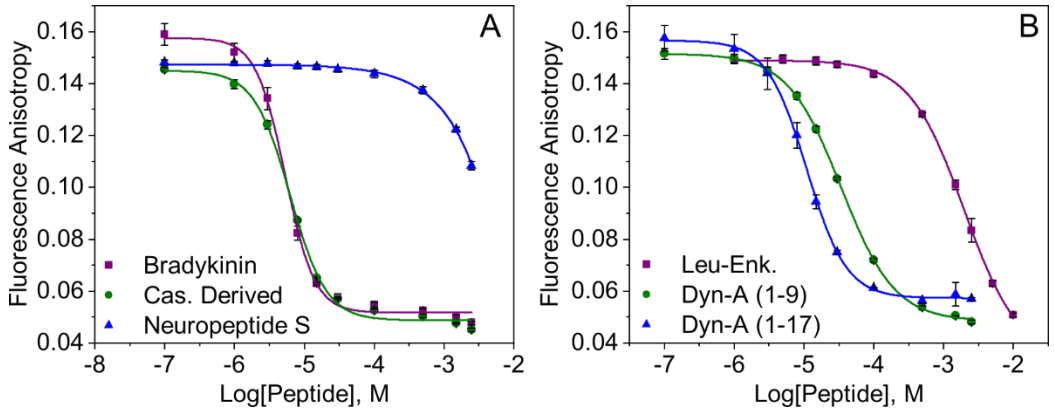

Figure 4.7 Competition dose-response binding to OppA measured by fluorescence anisotropy validates bradykinin-SR101 binds to the canonical substrate binding site.

(A) Unlabeled competitor peptides are able to displace bradykinin-SR101. The previously reported high affinity bradykinin and a casein-derived peptide are able to completely displace bradyknin-SR101. The previously reported low affinity peptide, neuropeptide S, partially displaces bradykinin-SR101 because the dose-response was limited by our peptide concentration range. (B) The related opioid peptides Leu-enkephalin, dynorphin-A (1-9), and dynorphin-A (1-17) exhibit increasing affinity with increasing length, respectively. Lines show the average fit for n = 3. Error bars are stdev.

Table 4.1 Binding characterization of peptides as determined by fluorescence anisotropy-based competitive binding assays at pH 6, 30°C (n = 3, Mean ± SD).

Peptide	**Sequence**	**IC_{50} (μM)**	**K_D (μM)‡**	**Ref. K_D (μM)***
Bradykinin	RPPGFSPFR	5.2 ± 0.2	0.13 ± 0.04	0.1 (pH 6, 15°C)[21] & 0.26 (pH 6, 25°C)[29]
Casein-Derived Peptide	SLSQSKVLPVPQ	6.33 ± 0.07	0.20 ± 0.01	0.77 (pH 6, 15°C)[21]
Neuropeptide S	SFRNGVGSGVKKTS FRRAKQ	No Fit	1800 ± 100	This study
Leu-Enkephalin	YGGFL	2000 ± 400	70 ± 8	50-100 (pH and temp not given)[29]
Dynorphin-A (1-9)	YGGFLRRIR	34.2 ± 0.7	13.3 ± 0.7	This study
Dynorphin-A (1-17)	YGGFLRRIRPKLKW DNQ	11.0 ± 0.5	3.3 ± 0.6	This study

‡ Fitted K_D values obtained by directly fitting competition dose response data to the competition binding model described in the Materials and Methods.
* Previously reported K_D values from the literature.

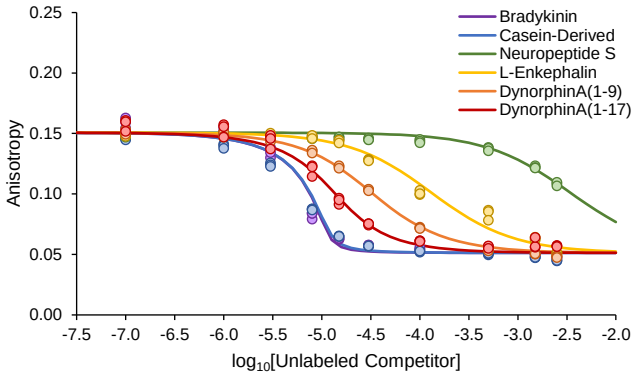

Figure 4.8 Fluorescence anisotropy competition dose-response data fitting.

Data was fitted using a complete competition model to determine the K_D values of the unlabeled competitor peptides (referred to as fitted K_U values in the Materials and Methods). Data from Figure 4.7 is replotted with the average fitted K_D curves.

Interestingly, we were also able to use our competition assay to determine the relative affinities of leu-enkephalin and dynorphin opioid peptides that have not been previously reported. Leu-enkephalin (YGGFL) has been previously reported to bind OppA with low affinity, which could not be quantified with gel shift or intrinsic protein fluorescence assays[18,21,29]. Using our fluorescence anisotropy assay, we found that leu-enkephalin displaced bradykinin-SR101 with an IC_{50} ~ 2 mM (Figure 4.7), (Table 4.1, Figures 4.4, 4.8). Furthermore, dynorphin-A (1-9) (YGGFLRRIR) exhibited an IC_{50} ~ 34 µM, and dynorphin-A (1-17) (YGGFLRRIRPKLKWDNQ) exhibited an IC_{50} ~ 11 µM. The Cheng-Prusoff equation is commonly used to convert the IC_{50} value to the K_D dissociation constant for the unlabeled competitor[48]. However, fluorescence anisotropy competition assays often do not fulfill the assumptions made by the Cheng-Prusoff equation[39,40,47]. Therefore, we directly fitted the competition dose response data to a three-state, two-ligand competition binding model to determine the competitor affinities (Table 4.1, Figures 4.4, 4.8)[39,40,47]. Our measured affinities for unlabeled bradykinin, the casein-derived peptide, and leu-enkephalin showed excellent agreement with previously reported values[21,29], validating our competition assay.

Previously, it was reported that OppA optimally binds to nonapeptides, but additional residues can contribute to increased affinity[21,23]. Using our fluorescence anisotropy assay, we quantified the trend in relative affinities for a series of closely related leu-enkephalin, dynorphin-A (1-9), and dynorphin-A (1-17) peptides. In particular, it is interesting that dynorphin-A (1-17) has a significantly higher affinity for OppA relative to the shorter dynorphin-A (1-9). This seems

to indicate that OppA forms further favorable contacts with the longer peptide sequence, which may be possible due to the particularly voluminous binding cavity of OppA (~4900 $Å^3$) conferred by the third domain of this substrate-binding protein[29].

4.4.2 pH and Temperature Dependence of OppA Peptide-Binding

Having established and validated our fluorescence anisotropy assay, we quantified how pH and temperature affect the peptide binding affinity of OppA. We measured the direct binding of bradykinin-SR101 to OppA at pH 5 to 8 at six different temperatures (18°C, 24°C, 30°C, 37°C, 45°C, and 55°C) (Figure 4.9), (Table 4.2), and we validated that unlabeled bradykinin could still bind and displace bradykinin-SR101 under these conditions (Figure 4.10), (Table 4.3). OppA exhibits its highest peptide affinities for the labeled bradykinin-SR101 under low pH and low temperature conditions. The highest affinities were measured at pH 6 near it optimal growth pH, and no further increase in affinity was observed at pH 5. In solution at pH 6 and pH 7, increasing temperature causes a decrease in bradykning-SR101 affinity. Interestingly, at pH 8 the measured peptide affinity did not vary widely from 18°C to 30°C, and the lowest affinities measured across the pH 5 to 8 range were in a similar concentration range between 20 - 30 µM, suggesting a lower affinity limit within this mesophilic range.

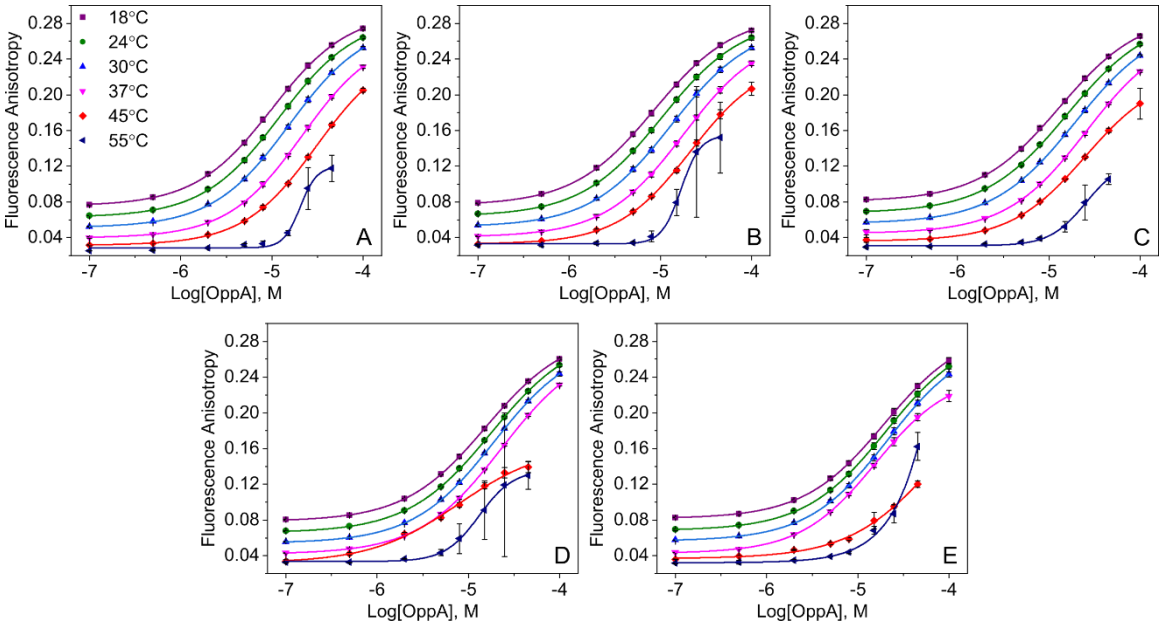

Figure 4.9 pH and temperature dependence of OppA binding affinity for labeled bradykinin-SR101.

Direct binding of bradykinin-SR101 was measured by fluorescence anisotropy at varying temperatures at (A) pH 5, (B) pH 6, (C) pH 6.5, (D) pH 7, and (E) pH 8. Lines show the average fit for n = 3. Error bars are stdev.

Table 4.2 Characterization of OppA binding affinities for labeled bradykinin-SR101 at varying pH and temperature using direct binding assays (n= 3, mean ± stdev).

	Direct Binding Assay K_D (μM)				
Temp (°C)	**pH 5**	**pH 6**	**pH 6.5**	**pH 7**	**pH 8**
18	10.0 ± 0.5	8.5 ± 0.4	13.0 ± 0.5	15.4 ± 0.4	20 ± 1
24	12.3 ± 0.5	10.4 ± 0.4	16 ± 1	17.8 ± 0.7	20 ± 1
30	15.4 ± 0.7	13.1 ± 0.7	19 ± 1	19.3 ± 0.8	22 ± 1
37	21.4 ± 0.5	18.0 ± 0.7	26 ± 1	22.9 ± 0.5	15.9 ± 0.5
45	31 ± 1	24 ± 1	30 ± 10	- *	- *
55	- *	- *	- *	- *	- *

* Not determined because of protein aggregation.

Our anisotropy competition assays measured a similar trend in which low pH and low temperature favored binding of the unlabeled bradykinin to OppA (Figure 4.10), (Table 4.3). As described above, we directly fitted the competition dose response data to a competition binding model in order to determine the K_D values because the Cheng-Prusoff equation is not valid here

(Figures 4.4, 4.11). The measured affinities for unlabeled bradykinin were approximately 10-fold higher relative to the labeled bradykinin-SR101. However, similarities between the behavior of the two peptides indicate that the presence of the SR101 dye itself does not obscure the pH and temperature dependence of the binding equilibrium. We also note that the IC_{50} values are insensitive to the pH-dependence because of the inherent limitations of the IC_{50} parameter, and the comparison of the IC_{50} and K_d values illustrates the importance of our fitting approach. As discussed by Huang[47], the IC_{50} value is a non-linear function of the peptide affinities, protein concentration, and labeled peptide concentration. For any competitor with much higher affinity relative to the labeled peptide affinity, the IC_{50} approaches a lower bound and no longer correlates with the K_d value. As expected, we observed this effect in our system, which matches well with simulations reported by Huang[47]. Thus, our fitting approach for the determination of K_d values is critical

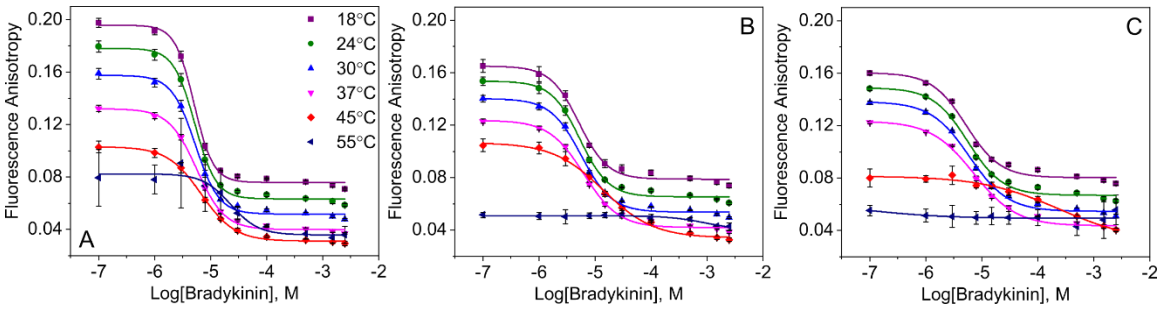

Figure 4.10 pH and temperature dependence of OppA binding affinity for unlabeled bradykinin.

Competitive binding of unlabeled bradykinin was measured by fluorescence anisotropy of displaced, pre-bound bradykinin-SR101 at varying temperatures at (A) pH 6, (B) pH 7, and (C) pH 8. Lines show the average fit for n = 3. Error bars are stdev.

Table 4.3 Characterization of OppA binding affinities for unlabeled bradykinin at varying pH and temperature using competition binding assays (n= 3, mean ± stdev).

	Affinities from Competition Binding Assays (μM)					
	pH 6		pH 7		pH 8	
	IC_{50}	K_D ǂ	IC_{50}	K_D ǂ	IC_{50}	K_D ǂ
18	5.1 ± 0.1	≤ 0.1 **	5.2 ± 0.2	0.2 ± 0.1	5.3 ± 0.4	0.4 ± 0.2
24	5.2 ± 0.3	≤ 0.1 **	5.37 ± 0.03	0.20 ± 0.03	5.6 ± 0.3	0.6 ± 0.3
30	5.3 ± 0.2	0.13 ± 0.04	5.7 ± 0.1	0.36 ± 0.05	6.0 ± 0.5	0.9 ± 0.3
37	5.6 ± 0.1	0.31 ± 0.06	6.3 ± 0.4	0.7 ± 0.1	7.2 ± 0.7	2 ± 1
45	6.8 ± 0.2	0.9 ± 0.1	- *	- *	- *	- *
55	- *	- *	- *	- *	- *	- *

* Not determined because of protein aggregation.

ǂ Fitted K_D values obtained by directly fitting competition dose response data to the competition binding model described in the Materials and Methods.

** The K_D is below the estimation limit for data fitted to the competition binding model.

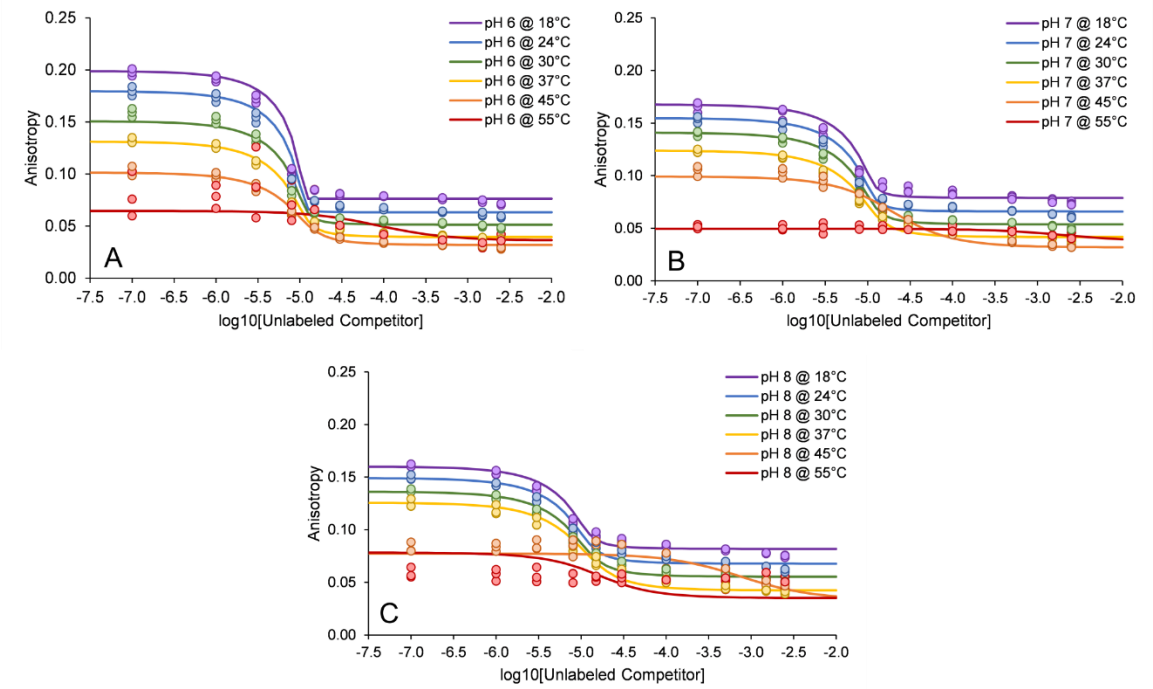

Figure 4.11 Fluorescence anisotropy competition dose-response data fitting.

Data was fitted using a complete competition model to determine the K_D values for unlabeled bradykinin at different pH and temperature (referred to as fitted K_U values in the Materials and Methods). Data from Figure 4.10 is replotted with the average fitted K_D curves.

Additionally, we observed protein aggregation and precipitation at higher temperatures (Figures 4.9, 4.10, 4.12) (Tables 4.2 & 4.3**)**. At pH 6, peptide binding was well behaved at temperatures from 18°C to 45°C, but aggregates were observed at 55°C that precluded

measurement of fluorescence anisotropy. At pH 7 and pH 8, the temperature threshold was lower, and protein aggregation was observed at 45°C and above. It is also possible that aggregation that was not visible by eye caused the affinity measured at pH 8 and 37°C to be an outlier relative to lower temperatures at pH 8 (Table 4.2). These results clearly demonstrate that OppA function is disrupted with increasing temperature, but low pH can increase resistance to loss of binding. These observations match well with the lower pH and temperature optimum for *L. lactis* growth. One possible explanation for the loss of binding at high temperature and high pH is that the OppA protein structure is less stable under these conditions. Therefore, to complement our functional studies using our fluorescence anisotropy assay, we next quantified thermal stability at different pH more precisely.

Figure 4.12 OppA protein aggregation after ramping to 55°C for a bradykinin-SR101 direct dose response assay at pH 6.

Wells in a 96-well plate show LlOppA protein aggregation in triplicate, vertically for each concentration tested. Column 7 = 8 μM, column 8 = 15 μM, column 9 = 25 μM, column 10 = 45 μM, column 11 = 100 μM OppA.

4.4.3 Low pH Increases OppA Thermal Stability as Measured by Circular Dichroism.

To determine if lower pH confers structural stability and facilitates peptide-binding function at high temperatures, we monitored the unfolding transition and quantified the threshold melting temperature (T_m) by circular dichroism (CD) spectroscopy. The CD spectrum for OppA shows an α-helical secondary structure signature with minima at 208 and 222 nm, allowing us to monitor unfolding (Figure 4.13). Melting curves were measured from the CD signal at 222 nm in the absence and presence of saturating unlabeled bradykinin at pH 6, 7 and 8 (Figure 4.13). The melting temperature of OppA is higher at lower pH, confirming our hypothesis that lower pH

stabilizes the structure of OppA. As expected, binding of bradykinin systematically increases the melting temperature at each pH relative to apo-OppA, and lower pH also increases thermal stability of the peptide-protein complex (Figure 4.13), (Table 4.4). These data show that the pH-dependent loss of protein stability could explain the decrease in peptide binding to OppA under alkaline conditions and high temperature. Though this does not explain the pH-dependent change in OppA affinity for peptides within the folded regime. Thus, we next qualitatively investigated this using electrostatic surface calculations.

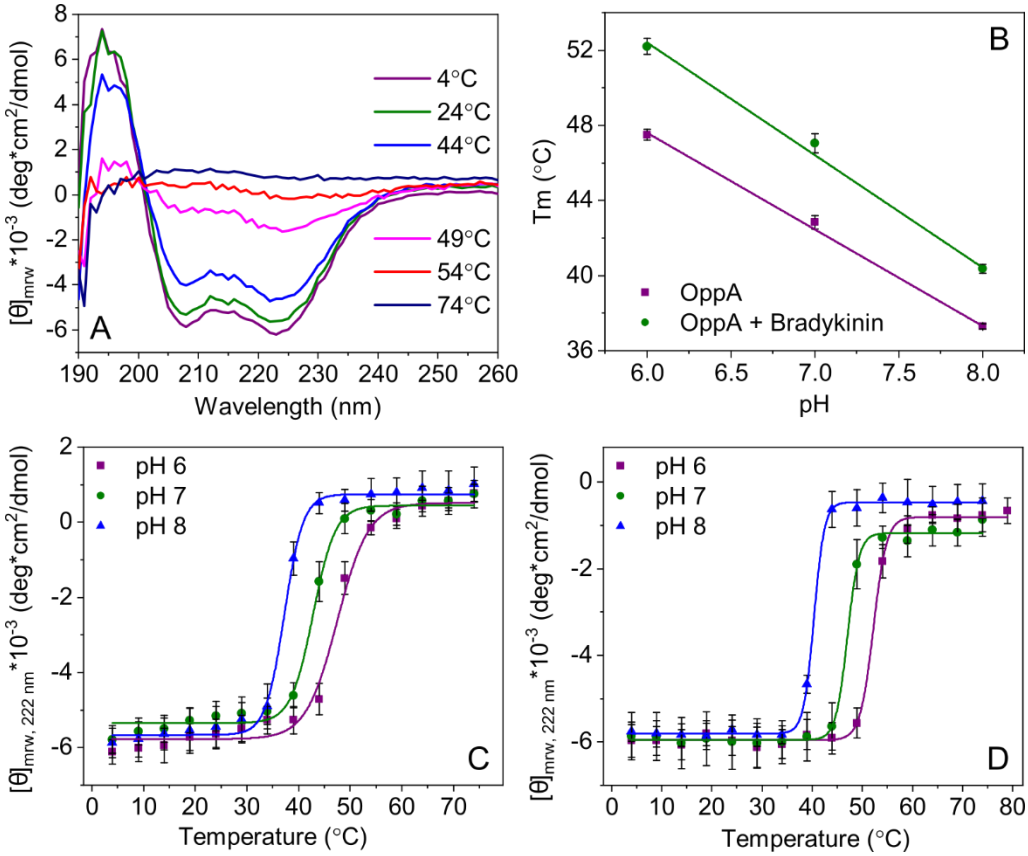

Figure 4.13 Acidic pH increases thermal stability measured by CD.

(A) Example of typical OppA CD spectra during a thermal ramp at pH 6. (B) Summary of the pH dependence of the melting temperature (T_m) of OppA with or without unlabeled bradykinin bound. Melting curves determined by CD at 222 nm in the (C) absence and (D) presence of 100 μM unlabeled bradykinin. Circular dichroism shown as mean residue ellipticity ($[\theta]_{mrw}$)*10^{-3}. Lines show the average fit for n = 4. Error bars are stdev.

Table 4.4 OppA melting temperature measured by CD signal at 222 nm at pH 6, 7 and 8 in the presence and absence of 100 µM bradykinin (n = 4, mean ± stdev).

pH	OppA Tm (°C)	OppA + Bradykinin Tm (°C)	ΔTm (°C)
6	47.5 ± 0.3	52.2 ± 0.4	4.7 ± 0.5
7	42.8 ± 0.4	47.0 ± 0.5	4.2 ± 0.6
8	37.3 ± 0.1	40.4 ± 0.2	3.1 ± 0.2

4.4.4 Electrostatic Surface Potential at the OppA Peptide-Binding Site.

It is possible that a change in the electrostatic environment of the binding site contributes to the pH-dependence of OppA peptide affinity. The electrostatic surface charge of *L. lactis* OppA[49] was calculated using PROPKA and APBS[50–53] at pH 6, 7, and 8 (Figure 1.14). At pH 6, there is a neutralization of the exposed surface area within the peptide-binding site compared to pH 7 and pH 8, which could facilitate binding of hydrophobic and neutral peptides. In contrast, *E. coli* OppA, which prefers positively charged peptides[54], exhibits less charge neutralization at pH 6 compared to pH 7 and pH 8, maintaining significant negative surface charge within the peptide-binding site. These observations provide a qualitative rationalization of the pH-dependent effects on peptide binding. In the future beyond the scope of this technical study, the effects of charge changing mutations of the OppA binding pocket and systematic sequence variation of the peptide ligand could be measured using our fluorescence anisotropy assay.

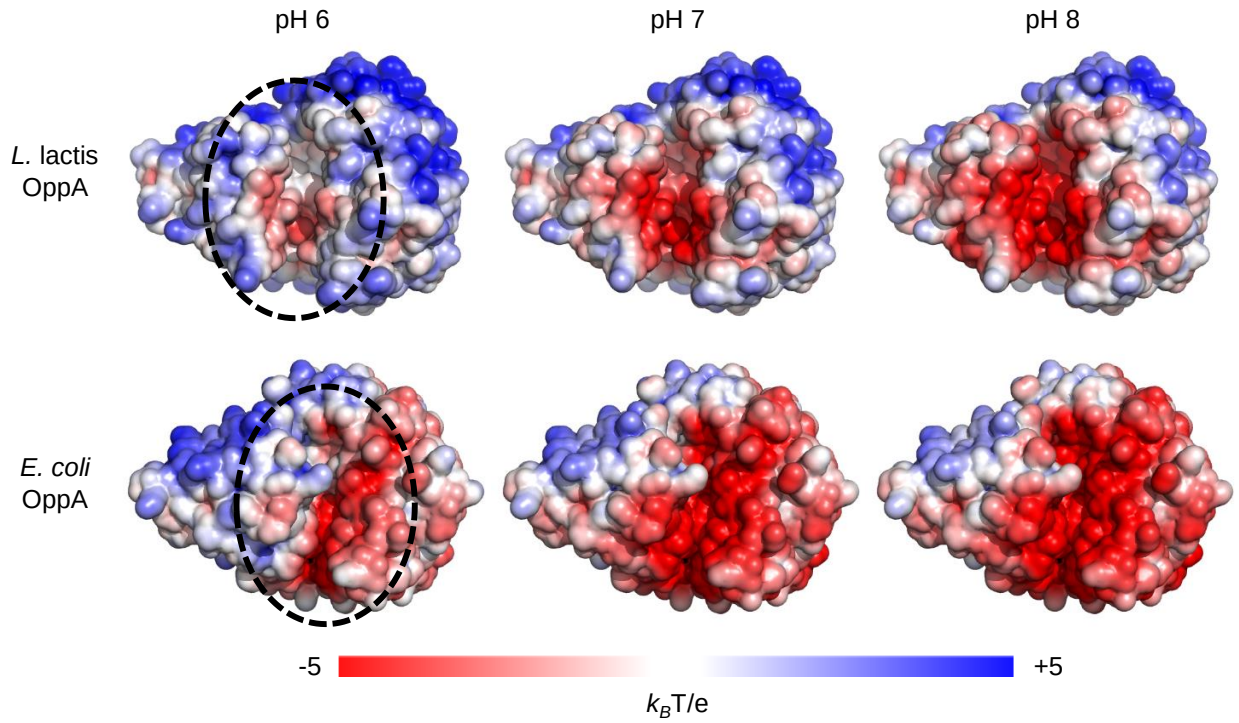

Figure 4.14 Electrostatic surface models for OppA calculated at different pH.

Surface charge was calculated and represented using PROPKA and APBS for (A) the *L. lactis* OppA apo-structure in the open conformation (PDB 3FTO) and (B) the *E. coli* OppA apo-structure in the open conformation (PDB 3TCH). The dashed circle highlights the peptide-binding site.

4.5 Discussion

The lactic acid bacteria *L. lactis* exhibits optimal growth at pH 6 [34,35], and we have discovered that acidic conditions promote the peptide binding function of OppA that is necessary to support the auxotrophic metabolism of this important species.

In this study, we developed and validated a fluorescence anisotropy peptide-binding assay to quantify relative pH-dependent differences in affinity. In previous work, X-ray crystallography and isothermal titration calorimetry have been extensively used to qualitatively and quantitatively characterize binding function for OppA proteins from different species[28,29,54–58]. In addition, radioactivity, gel shift, and intrinsic protein fluorescence methods have been used to measure dissociation constants and relative affinities for a number of peptides[18,21,23,25,45], and solvatochromic dye-labeled peptides have been used to characterize positional effects on OppA binding[22]. Fluorescence anisotropy has a number of practical advantages for measuring protein-

ligand interactions over these other methods[42–44], and for our study it offered excellent signal and dynamic range. For example, we were able to quantify the binding affinity of leu-enkephalin, which could not be quantified by gel shift or intrinsic protein fluorescence because its affinity to OppA is too low. Highlighting the versatility of our assay, in addition to leu-enkephalin we measured binding of two related but not previously reported peptides, dynorphin-A (1-9) and dynorphin-A (1-17). This series of peptides exhibited relative affinities ranging from 2 mM to 11 µM, and our assay was sensitive over at least 4-orders of magnitude in substrate concentrations over which we could quantify interactions.

Next, using our fluorescence anisotropy assay, we discovered that *L. lactis* OppA peptide affinity increases at acidic pH. We measured the highest affinity interaction with the bradykinin-SR101 peptide at pH 6 and 18°C, with affinities ranging from 8.5 µM at 18°C to 18 µM at 37°C. At the optimal growth temperature of 30°C, we measured affinities of 13 µM, 19 µM, and 22 µM at pH 6, 7, and 8, respectively, demonstrating a decrease in binding affinity under neutral and alkaline conditions. We also qualitatively observed a lower temperature threshold for protein aggregation at pH 7 and 8 compared to pH 6. The loss of peptide binding at high temperature and high pH suggested that the OppA protein could be more thermally stable at low pH. In fact, CD spectroscopy clearly showed that the melting temperature for the unfolding transition of OppA was also decreased at pH 7 and 8 relative to pH 6. Both the anisotropy and CD results are consistent with one another. Direct binding of the labeled BK-SR101 peptide and competitive binding of the unlabeled bradykinin peptide exhibit a decrease in affinity at higher temperatures and higher pH. Thus, acidic conditions stabilize OppA structure and promote its ability to bind substrate peptides for import into the bacteria.

The pH-dependence of OppA peptide binding within the folded regime also suggests that acidification could induce a classic change in surface charge near or within the substrate-binding pocket. Supporting this hypothesis, the electrostatic surface[49–52] of the substrate binding pocket showed a clear neutralization of negative surface charge at pH 6 relative to pH 7 and 8. However, we observed a decrease in bradykinin affinity with increasing pH, suggesting that an electrostatic interaction between the negative surface of OppA and the arginine residues of bradykinin is not the main binding determinant. We did observe that at pH 6 there is a small patch of residual negative surface charge from residues D134, D138, D455, E478, and D483. Thus at all pH values studied, there is some negative charge on OppA that could contribute to an electrostatic interaction

with the arginine residues, helping to explain the high affinity for bradykinin. However, other binding factors may contribute to a greater extent, which is consistent with the literature. For example Berntsson *et al.* demonstrated that a hydrophobic pocket in OppA is a major binding determinant, and in fact the phenylalanine residue of bradykinin binds to this hydrophobic pocket[31]. Therefore, another interpretation could be that the neutralization of surface charge at low pH promotes the development of a hydrophobic environment to facilitate binding of bradykinin, such as via interactions with the phenylalanine residue of bradykinin. Alternatively, decreasing pH could promote a conformational change that favors peptide binding, and this may be consistent with our CD results that show an increase in global structural stability at lower pH. In the future, a combination of systematic mutagenesis, structural analysis, and functional analysis with our anisotropy assay can be used to gain further insight into the binding mechanism of OppA.

Overall, this surface charge pattern also correlates well with the previously reported partial preference of *L. lactis* OppA for hydrophobic and basic peptides and decreased use of negatively charged acidic peptide substrates[18–25]. In contrast, Klepsch *et al.*[53] have shown that the *E. coli* OppA prefers positively charged peptide substrates, and they showed that there is an extensive negative surface around the binding site at pH 7. We additionally calculated the surface charge of *E. coli* OppA at pH 6 and 8 and found that substantial negative charge is maintained over the entire pH range unlike *L. lactis* OppA. This observation might suggest that binding to *E. coli* OppA is pH independent, which would be interesting to study in the future along with other OppA proteins of interest such as OppA from the Lyme disease culprit *Borrelia burgdorfei* [58,59].

There continues to be a strong interest in understanding the fundamental determinants of optimal growth and metabolism of *L. lactis* because of its significant industrial and biomedical potential[1,4,6–8,38,61,62]. We focused our efforts studying the purified OppA protein because it is the main determinant for peptide specificity of the Opp transport complex, and in the future it may be possible to adapt our assay to study binding to the whole transport complex reconstituted in liposomes[25]. Our current study suggests that the *L. lactis* OppA protein is well-tuned to solution conditions experienced during optimal growth, such as acidic pH and lowered temperature. It might also suggest that direct molecular manipulation of OppA or other substrate-binding proteins could be employed in strain engineering to adapt *L. lactis* to different metabolic conditions[45]. Furthermore, future studies of the pH-dependent structure and function of OppA from other species could provide similar insights into the sporulation of *Bacillus subtilis* or the virulence of

Borrelia burgdorfei, for example, in which an oligopeptide-binding protein is also a critical aspect of auxotrophy [59,60,63,64]. Overall, the fluorescence anisotropy assay that we developed provides an easy and versatile method to quantify the function of oligopeptide binding proteins in general.

4.6 References

1. Song, A. A. L., In, L. L. A., Lim, S. H. E. & Rahim, R. A. A review on Lactococcus lactis: From food to factory. *Microbial Cell Factories* **16,** 55 (2017).

2. Steidler, L. *et al.* Treatment of murine colitis by Lactococcus lactis secreting interleukin-10. *Science (80-.).* **289,** 1352–1355 (2000).

3. Liu, J., Dantoft, S. H., Würtz, A., Jensen, P. R. & Solem, C. A novel cell factory for efficient production of ethanol from dairy waste. *Biotechnol. Biofuels* **9,** 1–11 (2016).

4. Kandasamy, V., Liu, J., Dantoft, S. H., Solem, C. & Jensen, P. R. Synthesis of (3R)-acetoin and 2,3-butanediol isomers by metabolically engineered Lactococcus lactis. *Sci. Rep.* **6,** 36769 (2016).

5. Behnsen, J., Deriu, E., Sassone-Corsi, M. & Raffatellu, M. Probiotics: Properties, examples, and specific applications. *Cold Spring Harb. Perspect. Med.* **3,** a010074 (2013).

6. Mao, N., Cubillos-Ruiz, A., Cameron, D. E. & Collins, J. J. Probiotic strains detect and suppress cholera in mice. *Sci. Transl. Med.* **10,** eaao2586 (2018).

7. Loh, J. M. S., Lorenz, N., Tsai, C. J.-Y., Khemlani, A. H. J. & Proft, T. Mucosal vaccination with pili from Group A Streptococcus expressed on Lactococcus lactis generates protective immune responses. *Sci. Rep.* **7,** 7174 (2017).

8. Peng, X. *et al.* Production and delivery of Helicobacter pylori NapA in Lactococcus lactis and its protective efficacy and immune modulatory activity. *Sci. Rep.* **8,** 6435 (2018).

9. Smid, E. J., Plapp, R. & Konings, W. N. Peptide uptake is essential for growth of Lactococcus lactis on the milk protein casein. *J. Bacteriol.* **171,** 6135–6140 (1989).

10. Foucaud, C. *et al.* Specificity of peptide transport systems in Lactococcus tactis: Evidence for a third system which transports hydrophobic di- and tripeptides. *J. Bacteriol.* **177,** 4652–4657 (1995).

11. Juillard, V. *et al.* Oligopeptides are the main source of nitrogen for Lactococcus lactis during growth in milk. *Appl. Environ. Microbiol.* **61,** 3024–3030 (1995).

12. Tynkkynen, S. *et al.* Genetic and biochemical characterization of the oligopeptide transport system of Lactococcus lactis. *J. Bacteriol.* **175,** 7523–7532 (1993).

13. Kunji, E. R. S., Smid, E. J., Plapp, R., Poolman, B. & Konings, W. N. Di-tripeptides and oligopeptides are taken up via distinct transport mechanisms in Lactococcus lactis. *J. Bacteriol.* **175,** 2052–2059 (1993).

14. Kunji, E. R. S. *et al.* Transport of β-casein-derived peptides by the oligopeptide transport system is a crucial step in the proteolytic pathway of Lactococcus lactis. *J. Biol. Chem.* **270,** 1569–1574 (1995).

15. Davidson, A. L., Dassa, E., Orelle, C. & Chen, J. Structure, function, and evolution of bacterial ATP-binding cassette systems. *Microbiol. Mol. Biol. Rev.* **72,** 317–64 (2008).

16. Rice, A. J., Park, A. & Pinkett, H. W. Diversity in ABC transporters: Type I, II and III importers. *Critical Reviews in Biochemistry and Molecular Biology* **49,** 426–437 (2014).

17. Scheepers, G. H., Lycklama a Nijeholt, J. A. & Poolman, B. An updated structural classification of substrate-binding proteins. *FEBS Lett.* **590,** 4393–4401 (2016).

18. Detmers, F. J. M., Kunji, E. R. S., Lanfermeijer, F. C., Poolman, B. & Konings, W. N. Kinetics and specificity of peptide uptake by the oligopeptide transport system of Lactococcus lactis. *Biochemistry* **37,** 16671–16679 (1998).

19. Kunji, E. R. S. *et al.* Reconstruction of the proteolytic pathway for use of β-casein by Lactococcus lactis. *Mol. Microbiol.* **27,** 1107–1118 (1998).

20. Juillard, V., Guillot, A., Le Bars, D. & Gripon, J. C. Specificity of milk peptide utilization by Lactococcus lactis. *Appl. Environ. Microbiol.* **64,** 1230–1236 (1998).

21. Lanfermeijer, F. C., Picon, A., Konings, W. N. & Poolman, B. Kinetics and consequences of binding of nona- and dodecapeptides to the oligopeptide binding protein (OppA) of Lactococcus lactis. *Biochemistry* **38,** 14440–14450 (1999).

22. Lanfermeijer, F. C., Detmers, F. J. M., Konings, W. N. & Poolman, B. On the binding mechanism of the peptide receptor of the oligopeptide transport system of Lactococcus lactis. *EMBO J.* **19,** 3649–3656 (2000).

23. Detmers, F. J. M. *et al.* Combinatorial peptide libraries reveal the ligand-binding mechanism of the oligopeptide receptor OppA of Lactococcus lactis. *Proc. Natl. Acad. Sci.* **97,** 12487–12492 (2000).

24. Charbonnel, P. *et al.* Diversity of oligopeptide transport specificity in Lactococcus lactis species: A tool to unravel the role of OppA in uptake specificity. *J. Biol. Chem.* **278,** 14832–14840 (2003).

25. Doeven, M. K., Abele, R., Tampé, R. & Poolman, B. The binding specificity of OppA determines the selectivity of the oligopeptide ATP-binding cassette transporter. *J. Biol. Chem.* **279,** 32301–32307 (2004).

26. Tirado-Lee, L., Lee, A., Rees, D. C. & Pinkett, H. W. Classification of a haemophilus influenzae ABC transporter HI1470/71 through its cognate molybdate periplasmic binding protein, MolA. *Structure* **19,** 1701–1710 (2011).

27. Vyas, N. K., Vyas, M. N. & Quiocho, F. A. Sugar and signal-transducer binding sites of the Escherichia coli galactose chemoreceptor protein. *Science (80-.).* **242,** 1290–1295 (1988).

28. Tame, J. R. H. *et al.* The structural basis of sequence-independent peptide binding by OppA protein. *Science (80-.).* **264,** 1578–1581 (1994).

29. Berntsson, R. P. A. *et al.* The structural basis for peptide selection by the transport receptor OppA. *EMBO J.* **28,** 1332–1340 (2009).

30. Berntsson, R. P.-A., Smits, S. H. J., Schmitt, L., Slotboom, D. J. & Poolman, B. A structural classification of substrate-binding proteins. *FEBS Letters* **584,** 2606–2617 (2010).

31. Berntsson, R. P.-A., Thunnissen, A.-M. M. W. H., Poolman, B. & Slotboom, D. J. Importance of a hydrophobic pocket for peptide binding in Lactococcal OppA. *J. Bacteriol.* **193,** 4254–4256 (2011).

32. Mao, Boryeu; Pear, Michael R.; McCammon, J. Andrew; Quicho, F. A. Hinge-bending in L-Arabinose- binding Protein. *J. Biol. Chem.* **257,** 1131–1133 (1981).

33. Papadimitriou, K. *et al.* Stress Physiology of Lactic Acid Bacteria. *Microbiol. Mol. Biol. Rev.* **80,** 837–890 (2016).

34. Harvey, R. J. Damage to Streptococcus lactis resulting from growth at low pH. *J. Bacteriol.* **90,** 1330–1336 (1965).

35. Bibal, B., Goma, G., Vayssier, Y. & Pareilleux, A. Influence of pH, lactose and lactic acid on the growth of Streptococcus cremoris: a kinetic study. *Appl. Microbiol. Biotechnol.* **28,** 340–344 (1988).

36. Xie, Y., Chou, L., Cutler, A. & Weimer, B. DNA Macroarray Profiling of Lactococcus lactis subsp . lactis IL1403 Gene Expression during Environmental Stresses DNA Macroarray Profiling of Lactococcus lactis subsp . lactis IL1403 Gene Expression during Environmental Stress. *Appl. Environ. Microbiol.* **70,** 6738 (2004).

37. Taïbi, A., Dabour, N., Lamoureux, M., Roy, D. & LaPointe, G. Comparative transcriptome analysis of Lactococcus lactis subsp. cremoris strains under conditions simulating Cheddar cheese manufacture. *Int. J. Food Microbiol.* **146,** 263–275 (2011).

38. Chen, J., Shen, J., Ingvar Hellgren, L., Jensen, P. R. & Solem, C. Adaptation of Lactococcus lactis to high growth temperature leads to a dramatic increase in acidification rate. *Sci. Rep.* **5,** 14199 (2015).

39. Wang, Z. X. An exact mathematical expression for describing competitive binding of two different ligands to a protein molecule. *FEBS Lett.* **360,** 111–4 (1995).

40. Roehrl, M. H. A., Wang, J. Y. & Wagner, G. A General Framework for Development and Data Analysis of Competitive High-Throughput Screens for Small-Molecule Inhibitors of Protein−Protein Interactions by Fluorescence Polarization †. *Biochemistry* **43,** 16056–16066 (2004).

41. Kelly, S. M., Jess, T. J. & Price, N. C. How to study proteins by circular dichroism. *Biochim. Biophys. Acta - Proteins Proteomics* **1751,** 119–139 (2005).

42. Buchli, R. *et al.* Development and validation of a fluorescence polarization-based competitive peptide-binding assay for HLA-A*0201 - A new tool for epitope discovery. *Biochemistry* **44,** 12491–12507 (2005).

43. Moerke, N. J. Fluorescence Polarization (FP) Assays for Monitoring Peptide-Protein or Nucleic Acid-Protein Binding. in *Current Protocols in Chemical Biology* **1,** 1–15 (John Wiley & Sons, Inc., 2009).

44. Rossi, A. M. & Taylor, C. W. Analysis of protein-ligand interactions by fluorescence polarization. *Nat. Protoc.* **6,** 365–387 (2011).

45. Picon, A., Kunji, E. R. S., Lanfermeijer, F. C., Konings, W. N. & Poolman, B. Specificity mutants of the binding protein of the oligopeptide transport system of Lactococcus lactis. *J. Bacteriol.* **182,** 1600–1608 (2000).

46. Doeven, M. K., Van Bogaart, G. Den, Krasnikov, V. & Poolman, B. Probing receptor-translocator interactions in the oligopeptide ABC transporter by fluorescence correlation spectroscopy. *Biophys. J.* **94,** 3956–3965 (2008).

47. Huang, X. Fluorescence polarization competition assay: The range of resolvable inhibitor potency is limited by the affinity of the fluorescent ligand. *J. Biomol. Screen.* **8,** 34–38 (2003).

48. Cheng, Y. & Prusoff, W. H. Relationship between the inhibition constant (K1) and the concentration of inhibitor which causes 50 per cent inhibition (I50) of an enzymatic reaction. *Biochem. Pharmacol.* **22,** 3099–108 (1973).

49. Berntsson, R. P.-A. *et al.* Selenomethionine incorporation in proteins expressed in Lactococcus lactis. *Protein Sci.* **18,** 1121–1127 (2009).

50. Dolinsky, T. J., Nielsen, J. E., McCammon, J. A. & Baker, N. A. PDB2PQR: An automated pipeline for the setup of Poisson-Boltzmann electrostatics calculations. *Nucleic Acids Res.* **32,** W665–W667 (2004).

51. Olsson, M. H. M., Søndergaard, C. R., Rostkowski, M. & Jensen, J. H. PROPKA3: Consistent Treatment of Internal and Surface Residues in Empirical pKa Predictions. *J. Chem. Theory Comput.* **7,** 525–37 (2011).

52. Søndergaard, C. R., Olsson, M. H. M., Rostkowski, M. & Jensen, J. H. Improved treatment of ligands and coupling effects in empirical calculation and rationalization of p Kavalues. *J. Chem. Theory Comput.* **7,** 2284–2295 (2011).

53. Baker, N. A., Sept, D., Joseph, S., Holst, M. J. & McCammon, J. A. Electrostatics of nanosystems: Application to microtubules and the ribosome. *Proc. Natl. Acad. Sci.* **98,** 10037–10041 (2001).

54. Klepsch, M. M. *et al.* Escherichia coli peptide binding protein OppA has a preference for positively charged peptides. *J. Mol. Biol.* **414,** 75–85 (2011).

55. Tame, J. R. H., Sleigh, S. H., Wilkinson, A. J. & Ladbury, J. E. The role of water in sequence-independent ligand binding by an oligopeptide transporter protein. *Nat. Struct. Biol.* **3,** 998–1001 (1996).

56. Sleigh, S. H., Tame, J. R. H., Dodson, E. J. & Wilkinson, A. J. Peptide binding in OppA, the crystal structures of the periplasmic oligopeptide binding protein in the unliganded form and in complex with lysyllysine. *Biochemistry* **36,** 9747–9758 (1997).

57. Davies, T. G., Hubbard, R. E. & Tame, J. R. H. Relating structure to thermodynamics: The crystal structures and binding affinity of eight OppA-peptide complexes. *Protein Sci.* **8,** 1432–1444 (1999).

58. Sleigh, S. H., Seavers, P. R., Wilkinson, A. J., Ladbury, J. E. & Tame, J. R. H. Crystallographic and calorimetric analysis of peptide binding to OppA protein. *J. Mol. Biol.* **291,** 393–415 (1999).

59. Wang, X. G. *et al.* Analysis of Differences in the Functional Properties of the Substrate Binding Proteins of the Borrelia burgdorferi Oligopeptide Permease (opp) Operon. *J. Bacteriol.* **186,** 51–60 (2004).

60. Groshong, A. M., Dey, A., Bezsonova, I., Caimano, M. J. & Radolf, J. D. Peptide uptake is essential for borrelia burgdorferi viability and involves structural and regulatory complexity of its oligopeptide transporter. *MBio* **8,** e02047-17 (2017).

61. Liu, J. *et al.* Improving nitrogen source utilization from defatted soybean meal for nisin production by enhancing proteolytic function of Lactococcus lactis F44. *Sci. Rep.* **7,** 6189 (2017).

62. Cook, D. P., Gysemans, C. & Mathieu, C. Lactococcus lactis as a versatile vehicle for tolerogenic immunotherapy. *Frontiers in Immunology* **8,** 1961 (2018).

63. Koide, A. & Hoch, J. A. Identification of a second oligopeptide transport system in Bacillus subtilis and determination of its role in sporulation. *Mol. Microbiol.* **13,** 417–426 (1994).

64. Lazazzera, B. A., Solomon, J. M. & Grossman, A. D. An exported peptide functions intracellularly to contribute to cell density signaling in B. subtilis. *Cell* **89,** 917–925 (1997).

CHAPTER 5. ENGINEERING SINGLE FLUORESCENT PROTEIN AND FRET-BASED GENETICALLY ENCODED BIOSENSORS FOR BRADYKININ USING AN OLIGOPEPTIDE-BINDING PROTEIN

5.1 Abstract

Bradykinin is a signal peptide involved in several important physiological functions, including inflammation, blood vessel dilation, vascular permeability and pain. Additionally, bradykinin is involved in blood brain barrier permeability and is implicated in neuroinflammation. Thus, studying the role of bradykinin in neuroinflammation and the development of neurological disorders, such as Alzheimer's and Parkinson's disease is of interest. However, bradykinin signaling has been difficult to measure due to its transient nature and currently available methods lack the necessary spatial and temporal resolution needed to accurately measure bradykinin signaling in real-time. To fill this gap, we engineered genetically encoded fluorescent biosensors of bradykinin using an oligopeptide-binding protein from *Lactococcus lactis* as a sensing domain. We describe the development of a family of bradykinin sensors with diverse spectral properties using two engineering strategies. In the first strategy, single fluorescent protein-based sensors were engineered by inserting a cpEGFP near to the hinge-region of our sensing domain, which produced a functional intensiometric peptide sensor (PepI) and a ratiometric sensor (PepR). In the second strategy, FRET-based sensors were engineered by inserting mTurqouise2 and Venus into our sensing domain, which produced a functional ratiometric sensor (PepR-FRET).

5.2 Introduction

Bradykinin is a nine-amino acid (aa)-long signal peptide (RPPGFSPFR) that functions as an inflammatory mediator in the kallikrein-kinin system (KKS). The KKS is a hormonal system that consists of several protein and peptide components. It includes the tissue and plasma serine proteinase kallikrein enzymes, which liberate the kinin peptides, kallidin and bradykinin, respectively.[1,2] Upon liberation, these kinin peptides mediate their effects by acting on the G protein-coupled kinin receptors (B1R & B2R). The B2 receptor is constitutively expressed and rapidly endocytosed upon activation by its main agonist, bradykinin (K_D = 0.5 nM[3]), thus this receptor-activation pathway is thought to be primarily involved with acute inflammation and pain

responses.[4,5] For example, injection of bradykinin in humans causes local heat, redness, swelling and pain, which is mediated by blood vessel dilation, vascular permeability and B2 receptor activation on afferent neurons.[6]

In the brain, the KKS is thought to play an important role in neuroinflammation. In fact, B2 receptors are highly distributed and found on neurons, the endothelial lining, astrocytes and microglia.[7–12] For example, bradykinin is involved in glial-neuron communication in inflammation as it activates B2 receptors on astrocytes leading to an increase in intracellular calcium concentrations and glutamate release.[13–16] Additionally, bradykinin regulates blood-brain barrier permeability, and is implicated in leukocyte entrance and cytokine release leading to neuroinflammation.[17–19] Of interest is the role of bradykinin in the onset and progression of neurological disorders with neuroinflammatory involvement, including Alzheimer's and Parkinson's disease.[5] However, bradykinin signaling has been difficult to accurately measure due to its transient nature, where bradykinin is rapidly hydrolyzed *in vivo* (30 seconds or less) and acts at subnanomolar concentrations.[3,20] Additionally, current methods used to measure bradykinin signaling either lack good temporal or spatial resolution, such as *in situ* hybridization, immunostaining and electrophysiology. Thus, to study the role of bradykinin signaling in neuroinflammation, new tools are needed.

Genetically encoded fluorescent biosensors are tools that permit real-time imaging with high spatiotemporal resolution, and they can be readily expressed in live cells and live animals to span the realm of *in vitr*o and *in vivo* studies.[21] These tools have been successfully implemented in various animal models (e.g. *C. elegans*, zebrafish and mice) and have been used to study a diverse range of brain signaling molecules, including glutamate, calcium, and more recently, dopamine.[21–23] However, no such tools exist to monitor signal peptides such as bradykinin. To this end, we engineered genetically encoded fluorescent biosensors of bradykinin.

We implemented two sensor engineering strategies – single fluorescent protein-based sensors and Förster resonance energy transfer (FRET)-based sensors. Single fluorescent protein-based sensors involve the insertion of a single fluorescent protein into a sensing domain protein that binds the analyte of interest. These sensors are advantageous because they can be engineered as single or dual wavelength sensors. In the single wavelength form, these sensors have a single excitation peak that changes intensity in response to changes in analyte concentration, which makes them intensiometric. In the dual wavelength form, these sensors have two excitation peaks

that correspondingly change intensity in response to changes in analyte concentration, which makes them ratiometric. Intensiometric sensors are useful because they require minimal bandwidth for multiplex imaging, while ratiometric sensors require more bandwidth, but are typically more quantitative because they can normalize for sensor expression levels. Thus, the single fluorescent protein-based sensor engineering strategy can generate intensiometric and ratiometric sensors. However, single fluorescent protein sensors tend to be pH sensitive and often require extensive insertion site and linker composition optimization to produce a functional sensor.

On the other hand, FRET-based sensors involve the insertion of two fluorescent proteins – a FRET donor protein and a FRET acceptor. FRET is a nonradiative energy transfer mechanism that depends on the distance, orientation and spectral overlap between the two fluorescent proteins. Thus, this sensor engineering strategy comprises insertion of two spectrally compatible fluorescent proteins into positions in the sensing domain protein that undergo large rotational or translational changes upon binding analyte. These sensors are ratiometric, typically less pH sensitive and often do not require in depth linker optimization, however, they are bulkier and take up more spectral bandwidth than single fluorescent protein intensiometric sensors. Thus, there are advantages and disadvantages to the single-FP and FRET-based sensors, which is why we took both approaches to engineering our bradykinin sensors.

Here, we report the development and characterization of the first generation of a family of single fluorescent protein and FRET-based bradykinin sensors that were engineered using an oligopeptide-binding protein as the sensing domain. We discuss the selection of our sensing domain from four initial oligopeptide-binding proteins, development of our single fluorescent protein-based sensor variants by inserting a circularly permuted enhanced green fluorescent protein (cpEGFP) into our sensing domain, and development of our FRET-based sensors by inserting mTurqouise2 (mTq2) as our cyan donor fluorescent protein and Venus as our yellow acceptor fluorescent protein. We describe a functional single fluorescent protein-based intensiometric sensor, termed PepI (pronounced peppy) for intensiometric peptide sensor and a ratiometric single-fluorescent protein sensor, termed PepR (pronounced pepper) for ratiometric peptide sensor. Additionally, we describe a FRET-based ratiometric sensor, termed PepR-FRET.

5.3 Materials and Methods

5.3.1 Reagents and Materials

Chemicals and media were purchased from Fisher Scientific, Sigma and Formedium. High-fidelity master mix for Gibson Assembly was from New England Biolabs (Cat# M0492). Bradykinin peptide (RPPGFSPFR) was purchased from and HPLC purified (98% purity) by Bachem.

5.3.2 Plasmid Constructs

The *Lactococcus lactis* oligopeptide-binding protein A (LlOppA) amino acid sequence is from subspecies cremoris MG1363 (GenBank accession AAO63470.1), the *Bacillus subtillis* oligopeptide-binding protein A (BsAppA) amino acid sequence is from subspecies subtillis strain 168 (GenBank accession AAA62358.1), the *Streptomyces clavuligerus* oligopeptide-binding protein A 2 (ScOppA2) amino acid sequence is from strain ATCC 27064 (GenBank accession WP_003961820.1) and the Thermotoga maritima oligopeptide-binding protein A (TmOppA) amino acid sequence is from multispecies (GenBank accession WP_004060066.1), (Figure 5.1). Amino acid sequences for each oligopeptide-binding protein were checked for terminal signal peptides active in eukaryotes, gram-negative and gram-positive bacteria using the SignalP Server.[24] N-terminal signal peptides were identified in LlOppA (MNKLKVTLLASSVVLAATLLSACGSNQSSSTSTK), BsAppA (MKRRKTALMMLSVLMVLAIFLSACSGSKSSNSSA) and TmOppA (MKRFLVVLVLVLALVSVFGQTFE). These peptides were removed to prevent unwanted signals (e.g. palmitoylation and surface tethering) and were replaced by a methionine. Nucleotide sequences were optimized to minimize hairpins for cloning and were synthesized as gBlocks by Integrated DNA Technologies (IDT). gBlocks were cloned into a pRSETB vector by Gibson Assembly for bacterial expression and purification, which added a T7 leader and 6xHis tag before all protein sequences (MRGSHHHHHHGMASMTGGQQMGRDLYDDDDKDPT).

Fluorescent proteins were inserted into LlOppA by Gibson assembly. Our initial cpEGFP variant (S65T, F64L, A206K, H231L) was obtained from QUEEN-2m[25], while our improved cpEGFP variant was obtained from iGluSnFR (S65T, F64L, A206K, H231L, V163A, S175G, D180Y, V93I, K158R, Y145F)[26], which gave the S147 permutation, and Gibson assembly was

used to create the Y145 and N149 permutation variants of the iGluSnFR cpEGFP (Figure 5.7). These cpEGFP variants were inserted into LlOppA with a three amino acid linker on the N-terminus (FPG) and a two amino acid linker on the C-terminus (GT). Venus[27] with the inadvertent H231L mutation[28] was inserted into LlOppA with a three amino acid linker (AAA) at the N-terminus that included a NotI restriction enzyme site (GCGGCCGC), and a two amino acid linker (VD) at the C-terminus that included a SalI restriction enzyme site (GTCGAC). mTurquoise2 (mTq2)[29] was inserted into LlOppA without a linker on the N-terminus and with a two amino acid linker (VD) at the C-terminus that included a SalI restriction enzyme site (GTCGAC).

A

```
  1 MNKLKVTLLA SSVVLAATLL SACGSNQSSS TSTKKLKAGN FDVAYQNPDK
 51 AIKGGNLKVA YQSDSPMKAQ WLSGLSNDAT FATMSGPGGG QDGLFFTDSG
101 FKFIKGGAAD VALDKESKTA TITLRKDLKW SDGSEVTAKD YEFTYETIAN
151 PAYGSDRWTD SLANIVGLSD YHTGKAKTIS GITFPDGENG KVIKVQFKEM
201 KPGMTQSGNG YFLETVAPYQ YLKDVAPKDL ASSPKTTTKP LVTGPFKPEN
251 VVAGESIKYV PNPYYWGEKP KLNSITYEVV STAKSVAALS SSKYDIINGM
301 VSSQYKQVKN LKGYKVLGQQ AMYISLMYYN LGHYDAKNSI NVQDRKTPLQ
351 DQNVRQAIGY ARNVAEVDNK FSNGLSTPAN SLIPPIFKQF TSSSVKGYEK
401 QDLDKANKLL DEDGWKLNKS TGYREKDGKE LSLVYAARVG DANAETIAQN
451 YIQQWKKIGV KVSLYNGKLM EFNSWVDHMT TPPGANDWDI TDGSWSLASE
501 PSQQDLFSAA APYNFGHFND SEITKDLNDI DSAKSENPTY RKAAFVKYQE
551 DMNKKAYVIP TNFMLNYTPV NKRVVGMTLD YGAMNTWSEI GVSSAKLATK
```

Figure 5.1 Amino acid sequences of selected oligopeptide-binding proteins.

Amino acid sequences for (A) LlOppA (AAO63470.1), (B) BsAppA (AAA62358.1), (C) ScOppA2 (WP_003961820.1), and (D) TmOppA (WP_004060066.1).

Figure 5.1 Continued

B

```
  1 MKRRKTALMM LSVLMVLAIF LSACSGSKSS NSSAKKSAGK PQQGGDLVVG
 51 SIGEPTLFNS LYSTDDASTD IENMLYSFLT KTDEKLNVKL SLAESIKELD
101 GGLAYDVKIK KGVKFHDGKE LTADDVVFTY SVPLSKDYKG ERGSTYEMLK
151 SVEKKGDYEV LFKLKYKDGN FYNNALDSTA ILPKHILGNV PIADLEENEF
201 NRKKPIGSGP FKFKEWKQGQ YIKLEANDDY FEGRPYLDTV TYKVIPDANA
251 AEAQLQAGDI NFFNVPATDY KTAEKFNNLK IVTDLALSYV YIGWNEKNEL
301 FKDKKVRQAL TTALDRESIV SQVLDGDGEV AYIPESPLSW NYPKDIDVPK
351 FEYNEKKAKQ MLAEAGWKDT NGDGILDKDG KKFSFTLKTN QGNKVREDIA
401 VVVQEQLKKI GIEVKTQIVE WSALVEQMNP PNWDFDAMVM GWSLSTFPDQ
451 YDIFHSSQIK KGLNYVWYKN AEADKLMKDA KSISDRKQYS KEYEQIYQKI
501 AEDQPYTFLY YPNNHMAMPE NLEGYKYHPK RDLYNIEKWW LAK
```

C

```
  1 MTTAARRPAP TTAGAGWDAG VGALVNPSRR RGGTLRLVSS ADVDSLDPAR
 51 TYYVWVWLLQ RLLNRTLMAY PTDPGPAGLV PAPDLAEGPG EVSDGGRTWT
101 YRLRRGLRYD DGTPITSDDV RHAVQRVFAQ DVLPGGPTYL IPLLDDPERP
151 YPGPYRTDEP LRSVLTPDEH TIVFRLTRPF SDFDHLMAQP CAAPVPRRSD
201 TGADYGRDPR SSGPYRVARH EPDTLLHLER NPHWDRATDP IRPALPDRVE
251 LTIGLDVDVL DARLIAGEFD INLEGRGLQH AAQRRATADE VLRSHTDNPR
301 TSFLHFVAMQ PHIPPFDNVH VRRAVQYAAD KILLQDARGG PVNGGDLTTA
351 LFPPTLPAHQ DLDLYPTGPD LRGDLDAARA ELAAAGLPDG FRAVIGTQRG
401 KFRLVADAVV ESLARVGIEL TVKELDVATY FSLGAGHPET VREHGLGLLV
451 TDWGADFPTE YGFLAPLVDG RQIKRNGGNW NLPELDDPEV NALIDETLHT
501 TDPAARAELW RAVERRVMEH AVLLPLVHDK TLHFRNPWVT NVYVHPAFGL
551 YDIQAMGLAE ED
```

D

```
  1 MKRFLVVLVL VLALVSVFGQ TFERNKTLYW GGALWSPPSN WNPFTPWNAV
 51 AGTIGLVYEP LFLYDPLNDK FEPWLAEKGE WVSNNEYVLT LRKGLRWQDG
101 VPLTADDVVF TFEIAKKYTG ISYSPVWNWL GRIERVDERT LKFVFSDPRY
151 QEWKQMLINT PIVPKHIWEN KTEEEVLQAA NENPVGSGPY YVESWADDRC
201 VFKKNGNWWG IRELGYDPKP ERIVELRVLS NNVAVGMLMK GELDWSNFFL
251 PGVPVLKKAY GIVTWYENAP YMLPANTAGI YINVNKYPLS IPEFRRAMAY
301 AINPEKIVTR AYENMVTAAN PAGILPLPGY MKYYPKEVVD KYGFKYDPEM
351 AKKILDELGF KDVNKDGFRE DPNGKPFKLT IECPYGWTDW MVSIQSIAED
401 LVKVGINVEP KYPDYSKYAD DLYGGKFDLI LNNFTTGVSA TIWSYFNGVF
451 YPDAVESEYS YSGNFGKYAN PEVETLLDEL NRSNDDAKIK EVVAKLSEIL
501 LKDLPFIPLW YNGAWFQASE AVWTNWPTEK NPYAVPIGWN GWWQLTGIKT
551 LFGIEAK
```

5.3.3 Protein Expression and Purification

Polyhistidine-tagged proteins were expressed in BL21(DE3) *E. coli* in Auto Induction Media (AIM). First, single colonies were picked and used to inoculate 4 mL Luria broth (LB) starter cultures. Starter cultures were grown overnight with continuous shaking at 37°C and then adjusted with LB to an OD600 of 0.6 for LlOppA, BsAppA and ScOppA2 and an OD600 of 0.7 for TmOppA. Large AIM cultures (250 mL) were inoculated with 2.5 mL of OD600-adjusted LB starter cultures. Large culture expression conditions were optimized for each protein and were as follows: LlOppA sensor constructs were expressed at room temperature (RT) for ~65 hrs, BsAppA and TmOppA were expressed at 37°C for 16 hrs, and ScOppA2 was expressed at 37°C for 16 hrs and then RT for ~48 hrs all with continuous shaking at 160 rpm. Cultures were pelleted at 10,00xg for 15 minutes and lysed by sonication. Sonication was performed as previously described[30], except pellets were resuspended in Sodium Phosphate Buffer (25 mM sodium phosphate, 150 mM NaCl, 10% v/v glycerol, 15 mM imidazole, pH 7.0) with 0.2 mg/mL lysozyme, 0.1% v/v Triton X, 1 mM PMSF, 1 mM DTT. Purification was also performed as previously described[30], except proteins were purified in Sodium Phosphate Buffer. We recommend that any future work performed with LlOppA or LlOppA sensor constructs also uses this Sodium Phosphate buffer or another similar buffer at pH 7 due to the pH and temperature sensitivity of this protein and risk of denaturing.[30] Concentrations of the purified proteins were determined by absorbance at 280 nm using the Beer-Lambert Law, and the Northwestern University Peptide Properties Calculator to determine extinction coefficients for each protein and sensor construct.

For small scale expression of LlOppA sensor constructs, single BL21(DE3) colonies were picked and used to inoculate 4 mL AIM cultures. Cultures were grown at room temperature with continuous shaking at 300 rpm for ~65 hrs. For small scale lysis, 4 mL cultures were pelleted and resuspended in 700 μL Sodium Phosphate Buffer with 0.2 mg/mL lysozyme, 0.1% v/v Triton X, 1 mM PMSF, 1 mM DTT. Samples were freeze-thawed three times between a dry ice and ethanol bath and room temperature. $MgCl_2$ was added to a final concentration of 10 mM and 40 U of DNase I was added. Samples were incubated at room temperature for 30 minutes and pelleted at 4°C to obtain the clarified lysate. Protein concentration in lysate for steady-state and lifetime spectroscopy was estimated by 280 nm absorbance.

5.3.4 Circular Dichroism Spectroscopy

Pure proteins were diluted to 2 μM in 25 mM sodium phosphate buffer (no NaCl or glycerol due to CD absorbance) at pH 7. Diluted protein (800 μL) was added to a quartz cuvette with a 2 mm path length (Starna Cells, 18F-Q-10). CD absorbance was measured from 190 – 260 nm on a Jasco J-1500 circular dichroism spectrophotometer using a 50 nm/min scan speed, 1.0 nm data pitch, 1.0 nm bandwidth and 1 s digital integration time (D.I.T.).

Mean residue ellipticity ($[\theta]_{mrw}$) was calculated as described in Kelly et al[31] for each protein. First, mean residue weight (MRW) was calculated using the following equation: $MRW = \frac{M}{(N-1)}$, where M is the molar mass of the protein in Da, N is the number of amino acids in the protein, and the number of peptide bonds is N-1. Here, our BsAppA molar mass is 62317.2 Da with 544 amino acids giving an MRW of 114.8, our ScOppA2 molar mass is 65828.9 Da with 596 amino acids giving an MRW of 110.6, and our TmOppA molar mass is 65459.3 Da with 569 amino acids, giving an MRW of 115.2. Then, $[\theta]_{mrw}$ was calculated using the following equation: $[\theta]_{mrw,\lambda} = \frac{MRW*\theta_\lambda}{10*l*c}$, where θ_λ is the observed ellipticity in degrees, l is the pathlength in cm and c is the concentration in g/mL.

To measure thermal denaturation, the temperature was ramped from 4 - 99°C, increasing 1 degree/min measuring the full spectrum every 5°C with a 2-minute wait time before measurement for equilibration. Melting temperature (Tm) was determined by plotting the mean residue ellipticity at 222 nm against the temperature and fitting to a Boltzmann Distribution in OriginPro.

5.3.5 Steady-State Spectroscopy

For initial sensor screening, whole cell lysate containing sensor protein was diluted to 50 μM, while sensor as purified protein was diluted to 2 μM in Assay Buffer (25 mM sodium phosphate, 150 mM NaCl, 10% glycerol, 1 mM DTT, 1x SIGMAFAST protease inhibitor cocktail, 0.05% v/v TWEEN, pH 7.0) with or without 2.5 mM bradykinin peptide. Diluted sample (100 μL) was added to a 96-well non-binding microplate (VWR, 89089-582), and incubated at 24 or 37°C for at least 30 minutes to reach equilibrium. All fluorescence measurements were performed using a BioTek Synergy H4 microplate reader. For the single FP cpEGFP sensor constructs, fluorescence was measured using a Top 50% mirror, 400/30 nm excitation filter paired with a 528/20 nm

emission filter, and a 485/20 nm excitation filter paired with a 528/20 nm emission filter. For the FRET sensor constructs, fluorescence was measured using a 455 DRLP dichroic mirror (BioTek part# 7138455), 420/50 nm excitation filter paired with a 485/20 nm emission filter for donor fluorescence, and a 420/50 nm excitation filter paired with a 528/20 nm emission filter for FRET. Sensor dynamic range was calculated as $\frac{|F-F_o|}{F_o}$, where F_o is the fluorescence intensity or ratio for vehicle addition (0 mM bradykinin) and F is measured in the presence of 2.5 mM bradykinin.

Spectral measurements were as follows: 380 – 510 nm excitation scan at 530 nm emission (cpEGFP), 500 – 700 nm emission scan at 400 nm excitation (cpEGFP), 505 – 700 nm emission scan at 485 nm excitation (cpEGFP), 350 – 460 nm excitation scan at 480 nm emission (mTq2), 470 – 700 nm emission scan at 434 nm excitation (mTq2), 350 – 520 nm excitation scan at 540 nm emission (Venus), 525 – 700 nm emission scan at 505 nm excitation (Venus). Ratiometric cpEGFP sensor spectra were normalized by total fluorescence, while intensiometric cpEGFP sensor spectra were normalized by the peak fluorescence intensity of the vehicle control. Ratiometric FRET sensor spectra were normalized by total fluorescence.

For dose response measurements, sensor constructs were diluted to 1 μM in Assay Buffer with varying concentrations of bradykinin (0.01 – 316 μM for the single fluorescent-protein based sensor constructs and 0.1 – 3500 μM for the FRET-based sensor) or vehicle control, all at a final volume of 150 μL in a 96-well non-binding microplate. Samples were incubated at the desired temperature (24 or 37°C) for at least 30 minutes to reach equilibrium. Fluorescence filter reads and spectra were measured as described above. Dynamic range was calculated as described above, where F was measured in the presence of saturating bradykinin.

5.3.6 Lifetime Spectroscopy

FRET sensor constructs as purified protein were diluted to 3 μM, while pure mTq2 protein was diluted to 1 μM in 25 mM sodium phosphate, 150 mM NaCl, 10% v/v glycerol, pH 7.0. Diluted protein (200 μL) was added to a quartz cuvette with a 10 mm path length (Starna Cells, 16.160F-Q-10/Z15). The mTq2 donor fluorescence lifetimes were measured on an FS5 spectrofluorometer (Edinburgh Instruments, UK) with a 20 MHz white laser in reverse mode. Samples were excited at 434/3 nm with 474/3 nm emission with the emission rate adjusted to ~125,000 counts per second (cps) and ~20 MHz repetition rate. Lifetime histograms were overlayed with an instrument

response function (IRF) measured with LUDOX® colloidal silica the same day with similar instrument settings, and data was analyzed in Fluoracle by a reconvolution fit. The number of components for each fit was determined by fitting until a χ^2 value of < 1.5 was obtained, where the relative contribution of each component was above 5%. FRET efficiency was calculated as $1 - \tau_{FRET\ Sensor}/\tau_{mTq2}$.

5.3.7 Statistics

Statistical comparisons for sensors in the presence of 2.5 mM bradykinin and vehicle (0 mM bradykinin) were performed by two-sample t-tests with a 95% confidence interval.

5.4 Results & Discussion

5.4.1 Sensing Domain Selection

Table 5.1 Ligands and apo melting temperatures (Tm) of selected sensing domain proteins.

Organism	Protein	Ligands	Tm at pH 7 (°C)
Lactococcus lactis	LlOppA	Bradykinin (K_D = 0.1 uM)[30,32], oligopeptides (4-35 aa)[33–41]	43[30]
Bacillus subtilis	BsAppA	Bradykinin (K_D = 50 uM[42]), oligopeptides (9 aa)[43]	48
Streptomyces clavuligerus	ScOppA2	Bradykinin, arginine, oligopeptides (2-9 aa)[44,45]	37
Thermotoga maritima	TmOppA	Oligopeptide (20 aa)[46]	>99

To engineer a bradykinin sensor, we first identified oligopeptide-binding proteins to use as our sensing domains. We selected four oligopeptide-binding proteins, including OppA from *Lactococcus lactis* (LlOppA), AppA from *Bacillus subtilis* (BsAppA), OppA2 from *Streptomyces clavuligerus* (ScOppA2), and OppA from *Thermotoga maritima* (TmOppA), (Table 5.1). These proteins belong to a superfamily of substrate binding proteins, which act as part of a multicomponent transporter system, known as the ATP-binding cassette (ABC) transporters. Specifically, these oligopeptide-binding proteins are part of the cluster C substrate-binding proteins, which show little sequence identity (often < 20%), but are structurally similar, and consist

of three distinct domains (I, II and III).[47] Domains I and II make up lobe 1 of the protein and domain III is equivalent to lobe 2, where lobes 1 and 2 are connected by a hinge region that links domains I and III (Figure 5.2). Notably, these proteins undergo a conformational change known as the 'Venus flytrap' mechanism, which involves a rotation around the hinge region that allows the protein to transit between an open and closed state, where the closed state is favored upon substrate-binding.[47–49] This ligand-dependent conformational change is an important feature of sensing domains for engineering fluorescent biosensors because it can be allosterically linked to a change in the fluorescent signal. In fact, a number of other labs have taken advantage of this relatively large, hinge-rotation-based conformational change to successfully engineer sensors, including sensors of maltose[50,51], glutamate[26] and histidine[52]. Thus, we selected these sensing domains because they undergo a conformational change, which is key to engineering a successful single-FP or FRET-based sensor.

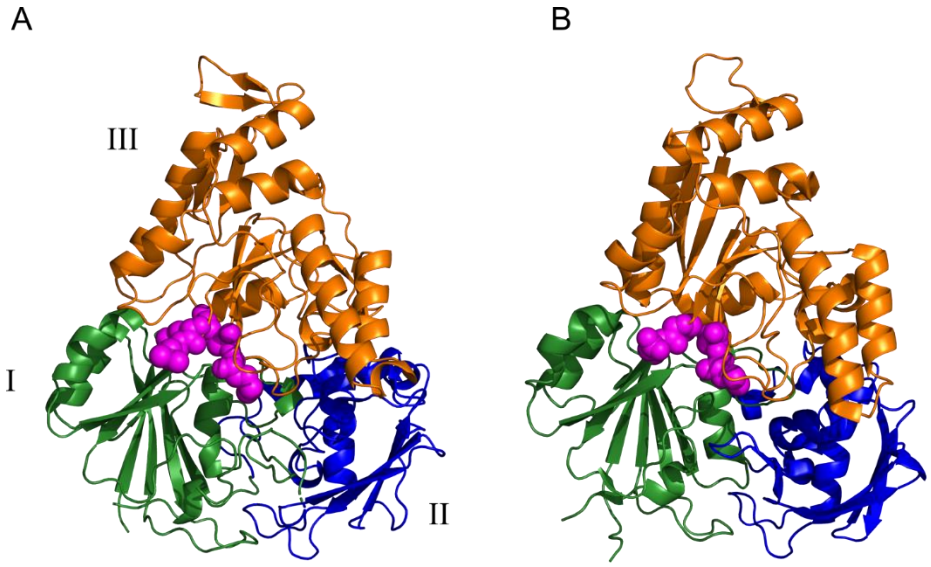

Figure 5.2 Class C Oligopeptide-Binding Proteins are Structurally Similar.

(A) The structure of LlOppA (PDB code 3DRG, closed state) consists of three domains; domain I (residues 54 – 104, 242 – 322, 565 – 592, shown in green), domain II (residues 105 – 241, shown in blue), and domain III (residues 323 – 564, shown in orange), where the hinge region resides between domains I and III (residues 322 – 323 and 564 – 565, shown in magenta). (B) BsAppA (PDB code 1XOC, closed state) also consists of three domains; domain I (residues 39 – 75, 206 – 286, 513 – 542, shown in green), domains II (residues 76 – 205, shown in blue), and domain III (residues 287 – 512), where the hinge region resides between domains I and III (residues 286 – 287 and 512 – 513, shown in magenta). *Residue numbering is according to the original amino acid sequence (Figure 5.1).

We also selected these proteins as our sensing domains because there is at least one crystal structure available for each of them[40,43,45,46], which aids in structure-guided engineering. Lastly, and most importantly, we selected these sensing domains because they bind oligopeptides, including bradykinin (Table 5.1). LlOppA has the highest reported affinity for bradykinin at 0.1 μM, followed by BsAppA at 50 μM, while ScOppA2 has been reported to bind bradykinin, but no affinity has been determined, and TmOppA has not been reported to bind bradykinin. We decided to include TmOppA because it is known to bind longer peptides (e.g. 20 aa) and it comes from a hyperthermophile, which indicates that this protein is likely stable at high temperatures. Temperature stability of sensing domains is often an overlooked aspect of sensor engineering but is especially important if the aim is to use these sensors in live mammalian cells or live animals (e.g. 37°C). These substrate-binding proteins are commonly acquired from mesophilic bacteria,

which optimally grow at temperatures ranging from ~20 - 45°C. We came to this important realization after some initial work with LlOppA, which is from bacteria that optimally grow at pH 6, 30°C[53,54]. In this work, we found that LlOppA is both pH and temperature sensitive, where it unfolds at 43°C at pH 7, and 37°C at pH 8 in the apo form.[30] While LlOppA is likely to be stable at physiological pH and temperature (e.g. pH 7 and 37°C) it may not be stable in more basic environments, such as in cellular mitochondria. It is important to be aware of these types of sensor limitations.

To ensure that our selected sensing domains are thermally stable at pH 7 and 37°C, we first determined their threshold melting temperatures (Tm) at pH 7 in the absence of ligand using circular dichroism (CD) spectroscopy. As shown in Figure 5.3, the CD spectra for all selected oligopeptide-binding proteins show an α-helical secondary structure signature like LlOppA. We next monitored unfolding from the CD signal at 222 nm (Figure 5.3) and calculated the Tm for each protein (Table 5.1). These data show that BsAppA and TmOppA are stably folded at pH 7 & 37°C, Tm = 48°C and >99°C, respectively. In fact, TmOppA is so thermally stable that we were unable to determine a Tm in the temperature range tested due to evaporation above 99°C. On the other hand, ScOppA2 is less thermally stable and is not likely to be properly folded at pH 7, 37°C (Table 5.1). With a Tm of 37°C we expect at least 50% of apo ScOppA2 protein to be unfolded at pH 7 & 37°C. For this reason, we decided that we would not move forward with ScOppA2 as a sensing domain.

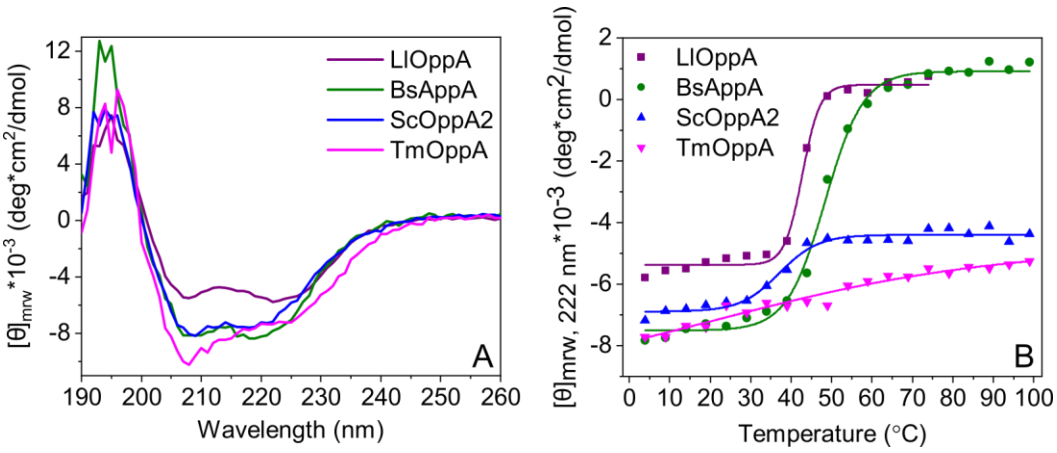

Figure 5.3 Circular Dichroism reveals differential thermal stabilities of selected sensing domains.

Secondary protein structure signatures (A) and melting curves (B) of our selected sensing domains. Lines on the melting curves are the fits used to determine melting temperatures. LlOppA data is from our previous report.[30] n = 1 for BsAppA, ScOppA2 and TmOppA.

After characterizing the thermal stability of our sensing domains, we were left with 3 viable proteins – LlOppA, BsAppA and TmOppA. While TmOppA is valuable because it is especially thermally stable, it has not been reported to bind bradykinin, while LlOppA and BsAppA have (Table 5.1). Additionally, due to the availability of several crystal structures of LlOppA, including a structure in the open conformation and one in the closed conformation with bradykinin bound[40] and our greater familiarity with this protein[30], we settled on using LlOppA as our proof of concept sensing domain. Thus, we next prepared and tested several sensor constructs using LlOppA to show the feasibility of engineering a bradykinin sensor from an oligopeptide-binding protein.

5.4.2 Single Fluorescent Protein Sensor Design & Characterization

Our single fluorescent protein sensor design uses LlOppA as the sensing domain and a cpEGFP inserted into a position in LlOppA to give a change in the fluorescent signal upon binding peptide. Circular permutation involves moving the N and C-termini of the fluorescent protein to new positions within the beta barrel of a fluorescent protein, and it has been shown to make fluorescent proteins more conformationally sensitive and aid in developing genetically encoded fluorescent sensors.[21,55] To identify candidate cpEGFP insertion sites within LlOppA that may result in a functional sensor, we first aligned the open conformation crystal structure of LlOppA (3DRK) to the bradykinin-bound and closed structure (3DRG). Each domain (I, II and III, Figure

5.2) was individually aligned and we scanned through the entire structure to identify surface loops or positions that show movement between the two aligned structures. We identified a number of potential insertion sites throughout the structure of LlOppA (Figure 5.4). We anticipate that a local conformational change in these positions can be translated to the nearby inserted fluorescent protein, and surface loops are preferred because inserting a protein at the surface of LlOppA is less likely to perturb its folding and functionality.

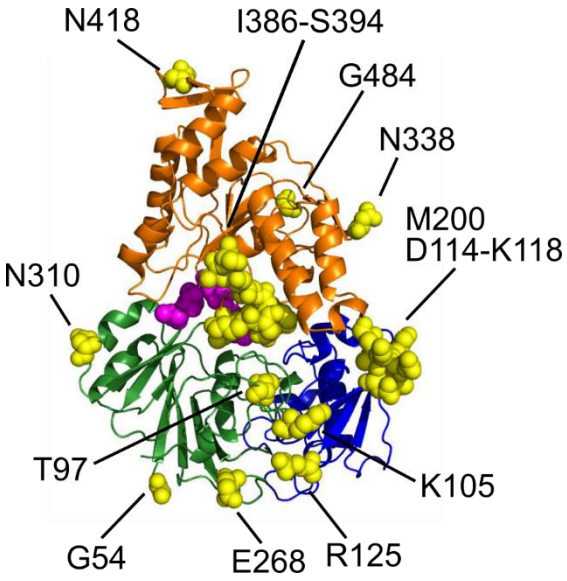

Figure 5.4 Single Fluorescent Protein Insertion Sites Identified for Potential Sensor Constructs.

Insertion sites were identified in LlOppA surface loops by aligning closed state (PDB code 3DRG) and open state (PDB code 3DRK) structures and searching for structural changes or movement between the two aligned structures. Insertion sites are shown as yellow spheres and labeled according to amino acid one letter codes, followed by the position in the protein sequence (Figure 5.1). Fluorescent proteins were inserted after the indicated amino acid. The hinge-region is shown as magenta spheres.

Figure 5.5 Linear diagram for single fluorescent protein-based sensor design.

A circularly permuted enhanced green fluorescent protein (cpEGFP) was inserted into LlOppA (shown in orange) with a three amino acid N-terminal linker (FPG) and a two amino acid C-terminal linker (GT) to generate single-fluorescent protein sensor constructs.

Table 5.2 Fluorescence of selected cpEGFP insertion sites determined by screening in lysate.

Domain I Sites	
G54	Brightly fluorescent
T97	Dimly fluorescent
E268	Brightly fluorescent
N310	Dimly fluorescent
Domain II Sites	
K105	Dimly fluorescent
D114 - K118	Not determined
R125	Not fluorescent
M200	Not fluorescent
Domain III Sites	
N338	Dimly fluorescent
I386	Not determined
F387	Brightly fluorescent
K388	Brightly fluorescent
Q389	Brightly fluorescent
F390	Brightly fluorescent
T391	Brightly fluorescent
S392	Not determined
S393	Brightly fluorescent
S394	Brightly fluorescent
N418	Dimly fluorescent
G484	Brightly fluorescent

Next, we prepared sensor constructs by inserting a cpEGFP acquired from a ratiometric ATP sensor, QUEEN-2m.[25] For these sensor constructs, we included a three amino acid linker at the N-terminus of the cpEGFP (FPG) and a two amino acid linker at the C-terminus of the cpEGFP (GT), (Figure 5.5). As an initial screen, we measured fluorescence of these sensor variants (Table 5.2). These data show that most of insertion sites tested were fluorescent, though domain II appears to be the least amenable to cpEGFP insertion as these insertion constructs showed low fluorescence and poor expression. Domain III appears to be the most amenable to cpEGFP insertions and the I386 – S394 loop shows good potential because these constructs were consistently bright, expressed well, and show diversity in the fluorescence excitation spectra, where both double and

single excitation peaks were observed. For example, the K388 insertion construct shows a single excitation peak at 495 nm, while the Q389 insertion construct shows a second blue-shifted excitation peak at 400 nm (Figure 5.6). The presence of two excitation peaks is advantageous because it gives a ratiometric readout, which can be used to normalize for differences in protein levels. Additionally, this I386 – S394 loop is near to the hinge-region of LlOppA (Figure 5.4), and previous sensors have successfully been engineered by inserting cpEGFP into a loop near to the hinge-region of a substrate-binding protein.[26,51] For these reasons, we selected the Q389 position in the I386 – S394 loop as our primary insertion site for sensor development.

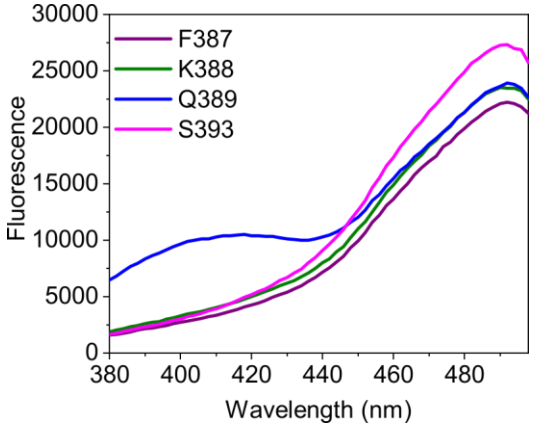

Figure 5.6 Fluorescence spectra of initial cpEGFP insertion constructs in the I386 – S394 loop.

Insertion of cpEGFP into the I386 – S394 loop, near to the hinge-region in LlOppA produces sensor variants that are brightly fluorescent and express well, and the Q389 insertion construct shows an additional excitation peak at 400 nm.

Following selection of our initial sensor candidate with a cpEGFP insertion at Q389, we attempted to express this sensor construct in mammalian cells at 37°C. However, we were unable to detect any green fluorescence from the cpEGFP, while we saw high red fluorescence from LlOppA fused to the red fluorescent protein, mCherry (LlOppA-mCherry), (data not shown). This indicates that LlOppA expresses well in mammalian cells, but the Q389 insertion construct is either not expressing well or the fluorescent protein is not maturing. After further investigation in the literature we discovered that the cpEGFP variant that we were using and acquired from QUEEN-2m lacks several of the mutations that have been shown to result in better temperature stability and brightness (Table 5.3). Additionally, our selected cpEGFP has previously been reported to express poorly at 37°C.[55] Thus, we decided to further optimize this LlOppA3-Q389-cpEGFP sensor by

swapping out our original cpEGFP for the cpEGFP from iGluSnFR[26], which contains mutations for improved temperature stability and brightness (Table 5.3). Additionally, the cpEGFP from iGluSnFR has a different permutation than the cpEGFP from QUEEN-2m, where the N-terminus begins at amino acid position S147 instead of Y145. These permutations also differ from GCaMP1 and 2, which begins at N149 and was selected after screening permutations and linkers to identify functional sensor constructs.[56] In addition to swapping out our cpEGFP for a variant with improved temperature stability and brightness, we included three different permutations of the cpEGFP from iGluSnFR (Figure 5.7). The Y145 permutation is like the permutation in our original cpEGFP from QUEEN-2m, the S147 permutation is comparable to the permutation in iGluSnFR and the N149 permutation is comparable to the cpEGFP from GCaMP. From here on, these cpEGFP's will be termed Y145, S147 and N149 to distinguish the different permutation versions.

Table 5.3 Mutations found in cpEGFP variants used to develop single FP sensors and their corresponding effects on fluorescence and stability.

Mutation	Effect	Sensor
S65T	Phenolate anion (favors 489-490 nm peak)[28]	QUEEN-2m[25], iGluSnFR[26], GCaMP2[57]
F64L	Improved folding at 37°C[28]	QUEEN-2m, iGluSnFR, GCaMP2
A206K	Prevents GFP dimerization[58]	QUEEN-2m, iGluSnFR, GCaMP2
H231L	Inadvertent/neutral[28]	QUEEN-2m, iGluSnFR, GCaMP2
V163A	Improved temperature stability[59]	iGluSnFR, GCaMP2
S175G	Improved temperature stability[59]	iGluSnFR, GCaMP2
D180Y	Improved brightness[57]	iGluSnFR, GCaMP2
V93I	Improved brightness[57]	iGluSnFR, GCaMP2
K158R	Unknown, likely inadvertent[51]	iGluSnFR
Y145F	Unknown[51]	iGluSnFR

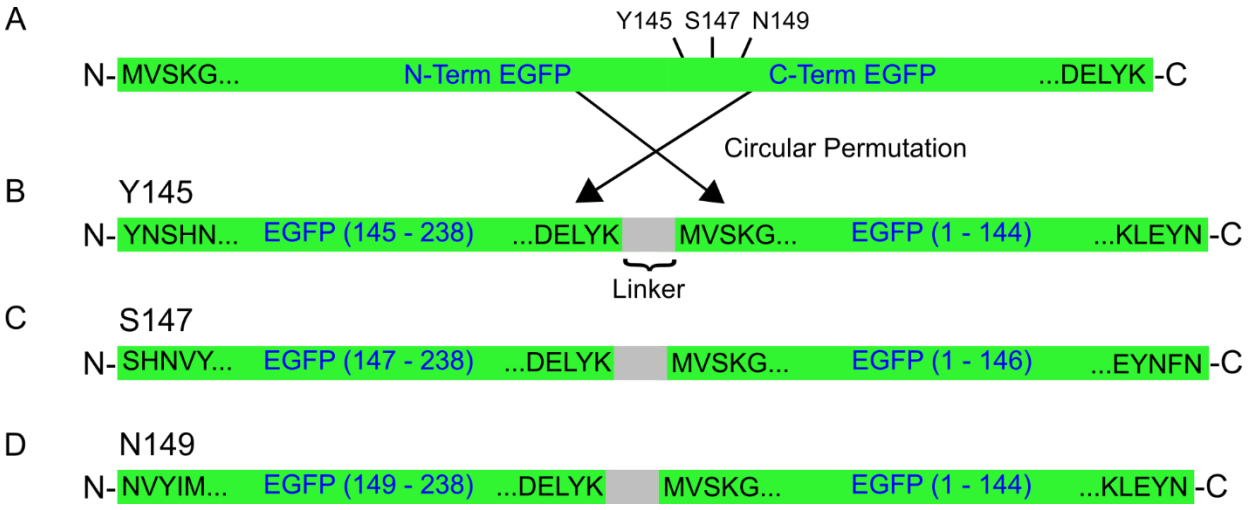

Figure 5.7 EGFP circular permutation and cpEGFP variants selected for insertion at the Q389 position of LlOppA.

(A) EGFP is circularly permuted by moving the N and C-termini to new positions within the protein sequence. Linear diagrams are shown for the three cpEGFP permutation variants inserted into LlOppA, including the (B) Y145, (C) S147, and (D) N149 permutations. Permutation variants are named according to the N-terminal start position in the amino acid sequence. A GGTGGS linker (shown in gray) was used to connect the N and C-termini from the original EGFP (A) in the permutation variants (B – D).

Once we had narrowed down our cpEGFP variants, these proteins were cloned into LlOppA at the Q389 position to give three sensor variants. Insertion of these three different permutations of cpEGFP produced three sensor variants that were bright and expressed well. We think it is worthwhile to mention that in performing this cloning we initially removed part of the T7 leader sequence from the pRSETB plasmid for the LlOppA-Q389-Y145 sensor so that it was shortened to MRGSHHHHHHGMASM. However, protein from this plasmid did not express well or show any fluorescence. Upon adding the complete T7 leader sequence back in we were able to recover fluorescence and expression. This seemed to indicate that the T7 leader sequence is important for the expression and stability of our sensor construct. This has similarly been reported for GCaMP2, where the authors found that including the N-terminal polyHis RSET sequence was crucial for thermal stability, so they included it in their mammalian expression vectors, and it is included in the mammalian expression vector of GCaMP5.[57,60] Thus, future studies should consider including the His tag and T7 leader sequence to circumvent expression issues with cpEGFP-based sensors.

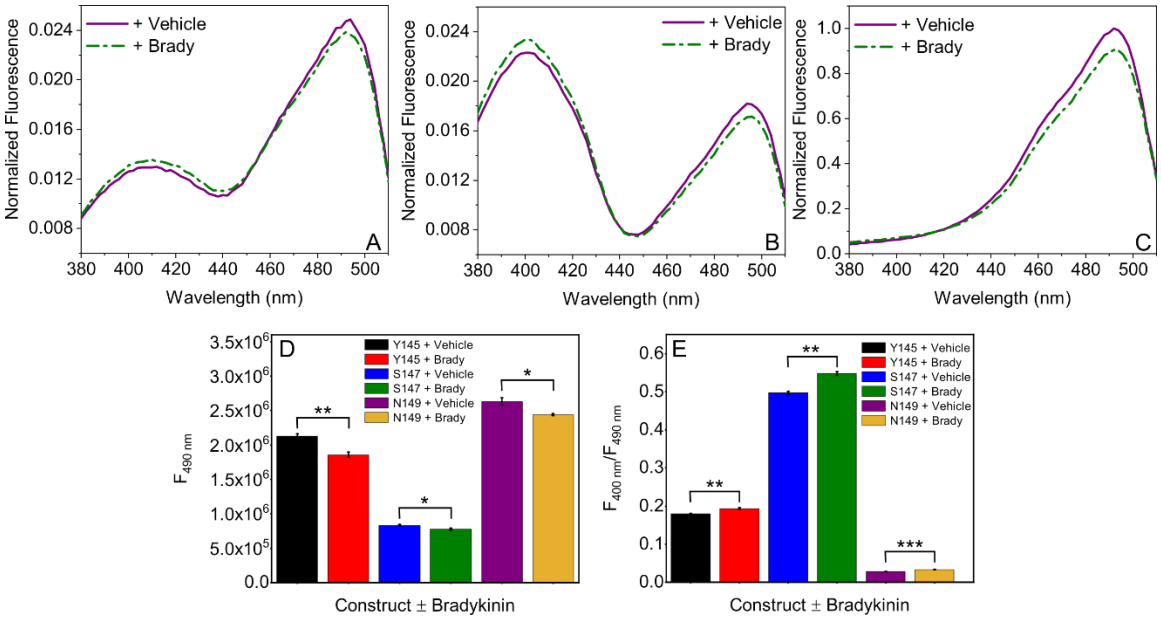

Figure 5.8 LlOppA-Q389 sensor constructs at 24°C show diverse spectral properties and are responsive to bradykinin additions.

Fluorescence excitation spectra were measured for the three LlOppA-Q389 sensors, including (A) the ratiometric LlOppA-Q389-Y145 and (B) LlOppA-Q389-S147 sensors and the intensiometric (C) LlOppA-Q389-N149 sensor. Sensor constructs in the presence of vehicle vs saturating bradykinin show significant changes in fluorescence measured at (D) 490 nm (Y145 0 mM vs 2.5 mM, $p = 0.001$; S147 0 mM vs 316 µM, $p = 0.0033$; N149 0 mM vs 316 µM, $p = 0.0037$) and (E) the ratio of 400 nm to 490 nm (Y145 0 mM vs 2.5 mM, $p = 0.0002$; S147 0 mM vs 316 µM, $p = 0.0002$; N149 0 mM vs 316 µM, $p = < 0.0001$). The Y145 and S147 spectra are normalized by total fluorescence, while the N149 spectra are normalized by peak fluorescence intensity of the vehicle condition. Spectra (A – C) represented as mean for n = 3 and bar graph data (D & E) represented as mean ± stdev for n = 3. Significance set at $p \leq 0.05$, *p-value ≤ 0.05, **p-value ≤ 0.001, ***p-value ≤ 0.0001.

We next measured fluorescence spectra of these Q389 sensor variants in the presence of saturating concentrations of bradykinin or vehicle at 24°C. Fortuitously, we found that all three sensors are responsive to bradykinin and show distinct spectral properties (Figure 5.8). The Y145 and S147 sensors are ratiometric with peaks at 400 nm and 495 nm, while the N149 sensor is intensiometric with the anionic peak (495 nm) dominating. As shown in Table 5.4, these sensors display 7 – 10% changes in signal, where the S147 sensor is the most responsive with a dynamic range of 10.3%.

Table 5.4 Fluorescence ratios and dynamic range of the Q389 sensor constructs as purified protein at 24°C and 37°C (mean ± stdev, n = 3).

Sensor Variant	Temp (°C)	F_{400}/F_{490}	Dynamic Range
Y145	24	0.179 ± 0.001	8.0 ± 0.4
S147	24	0.497 ± 0.005	10.3 ± 0.3
N149	24	2.63E+06 ± 5.E+04*	7.2 ± 1.3
Y145	37	0.1224 ± 0.0001	14.5 ± 0.4
S147	37	0.331 ± 0.004	25.3 ± 0.2
N149	37	1.4E+06 ± 1.E+05*	50 ± 10

*Values given as F_{490} because of the intensiometric nature of the N149 sensor construct.

Due to the known temperature sensitivity of LlOppA (apo Tm at pH 7 = 43°C)[30], there is some concern that this sensing domain may become even more thermally unstable with insertion of a fluorescent protein. To test this and confirm the functionality of these single FP sensors at physiologically relevant temperatures, we measured the fluorescence of these sensors in the presence and absence of saturating bradykinin at 37°C (Figure 5.9). These data reveal that our single FP sensors remain responsive to bradykinin at 37°C and even show extended dynamic ranges of 14.5 – 50% (Table 5.4), where the S147 and N149 sensors are the most responsive with dynamic ranges of 25.3 and 50%, respectively. Due to the high sensitivity of the S147 and N149 sensors to bradykinin and their function as a ratiometric and intensiometric sensors, respectively, we selected these sensors for further characterization.

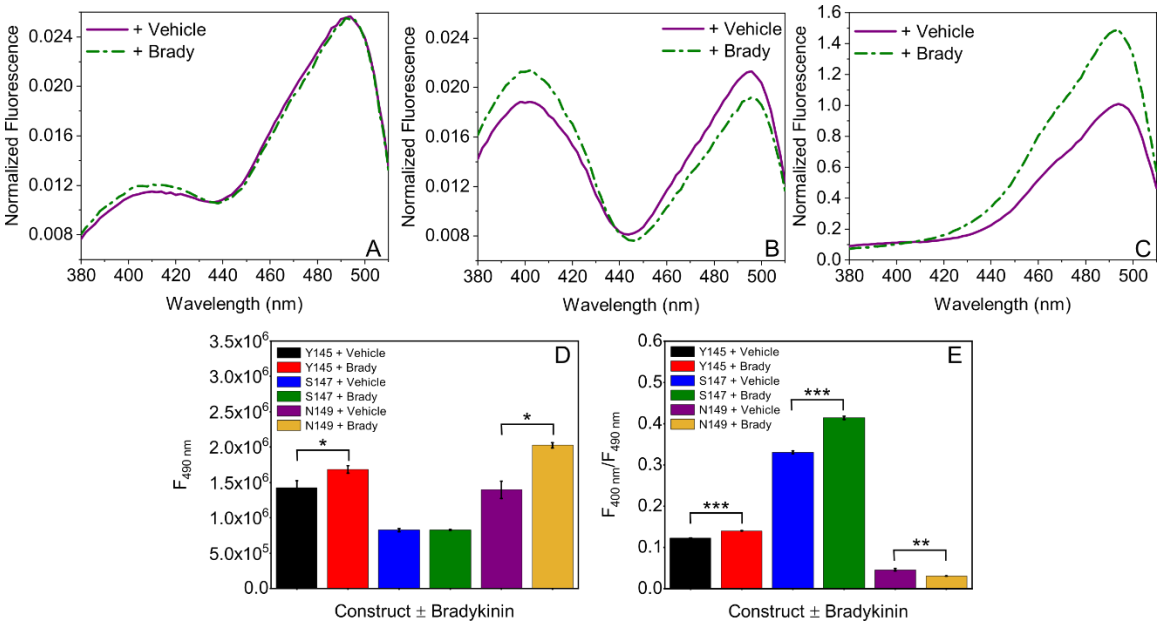

Figure 5.9 LlOppA-Q389 sensor constructs maintain response to bradykinin at 37°C.

Fluorescence excitation spectra were measured for the three LlOppA-Q389 sensors at 37°C, including (A) the ratiometric LlOppA-Q389-Y145 and (B) LlOppA-Q389-S147 sensors and the intensiometric (C) LlOppA-Q389-N149 sensor. Sensor constructs in the presence of vehicle vs saturating bradykinin show significant changes in fluorescence measured at (D) 490 nm (Y145 0 mM vs 2.5 mM, p = 0.0172; N149 0 mM vs 316 µM, p = 0.0011) and (E) the ratio of 400 nm to 490 nm (Y145 0 mM vs 2.5 mM, p = < 0.0001; S147 0 mM vs 316 µM, p = < 0.0001; N149 0 mM vs 316 µM, p = 0.001). The Y145 and S147 spectra are normalized by total fluorescence, while the N149 spectra are normalized by peak fluorescence intensity of the vehicle condition. Spectra (A – C) represented as mean for n = 3 and bar graph data (D & E) represented as mean ± stdev for n = 3. Significance set at p ≤ 0.05, *p-value ≤ 0.05, **p-value ≤ 0.001, ***p-value ≤ 0.0001.

To determine the affinity of the S147 and N149 sensors for bradykinin we next measured dose response curves at 24 and 37°C. Interestingly, the N149 sensor affinity at 24°C (K_D = 1.5 µM) is an order of magnitude lower than the S147 sensor affinity for bradykinin at 24°C (K_D = 0.27 µM), (Figure 5.10, Table 5.5). Additionally, increased temperature differently affects the affinities of these sensors, where the S147 sensor affinity for bradykinin decreases at 37°C (K_D = 1.6 µM) and the N149 sensor affinity increases at 37°C (K_D = 0.4 µM), (Figure 5.10, Table 5.5). Of note, the N149 sensor functions as a "turn off" sensor at 24°C, where the fluorescence at 490 nm decreases at higher concentrations of bradykinin. On the other hand, the N149 sensor functions as a "turn on" sensor at 37°C, where the fluorescence at 490 nm increases at higher concentrations of bradykinin (Figure 5.10). These results show that insertion of two cpEGFP permutation variants (S147 and N149) at the Q389 position in LlOppA produced a functional intensiometric and

ratiometric sensor that sense bradykinin with K_D's ranging from 0.27 – 1.6 μM, and these sensors retain function at a physiologically relevant temperature of 37°C.

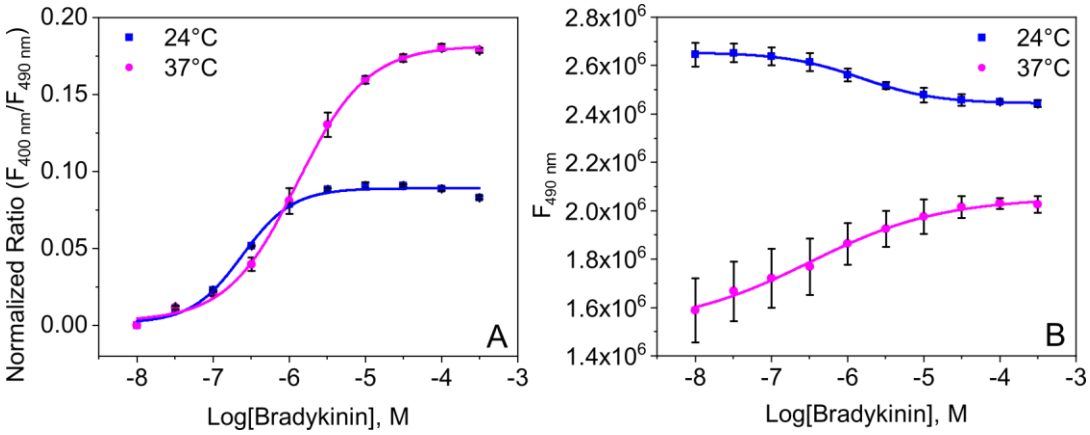

Figure 5.10 S147 and N149 sensors measure bradykinin in a dose-dependent manner at 24°C and 37°C.

Dose response curves were measured at 24°C and 37°C for the (A) S147 ratiometric sensor as the excitation ratio of fluorescence at 400 nm and 490 nm and the (B) N149 intensiometric sensor at the dominant 490 nm excitation peak. Lines show the average fit for n = 3. Error bars are stdev.

Table 5.5 S147 and N149 sensor affinities for bradykinin peptide (RPPGFSPFR) at 24°C and 37°C (mean ± stdev, n = 3).

Sensor Variant	Temp (°C)	K_D (μM)
S147	24	0.268 ± 0.007
N149	24	1.5 ± 0.2
S147	37	1.6 ± 0.4
N149	37	0.4 ± 0.2

5.4.3 FRET Sensor Design & Characterization

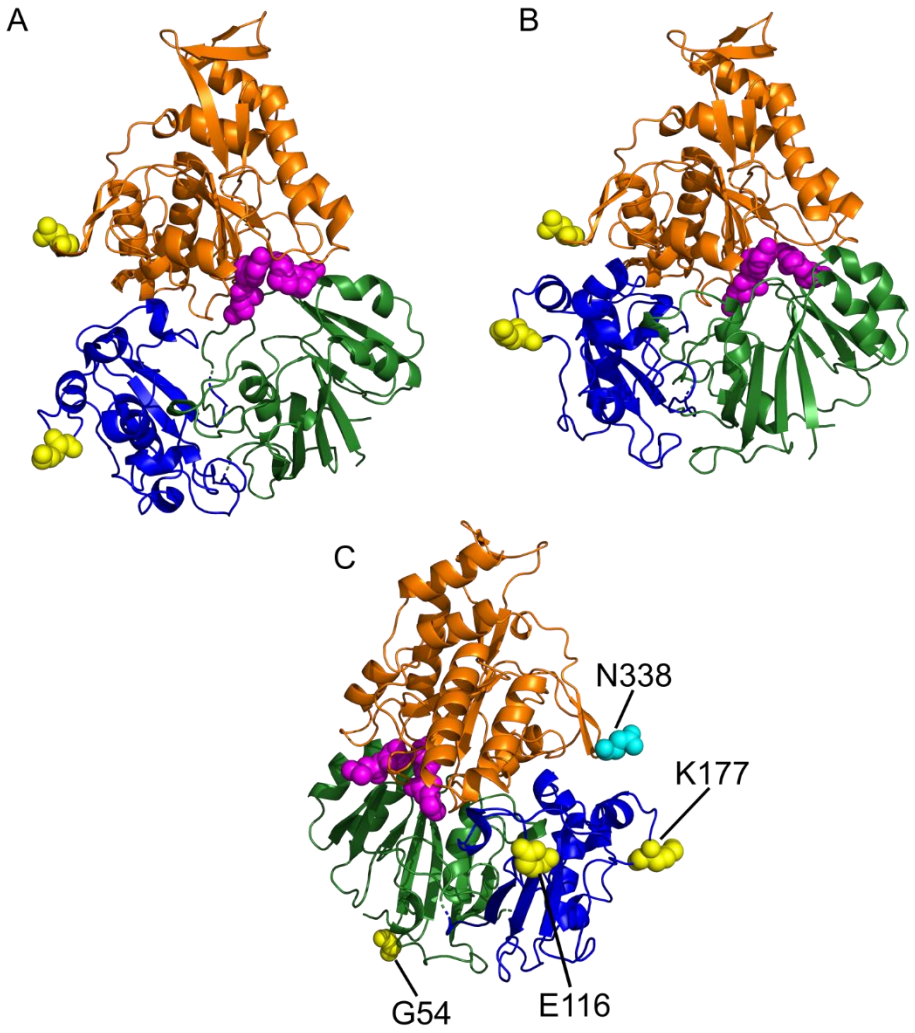

Figure 5.11 Fluorescent protein insertion sites for FRET sensor development.

Two loops were identified on the surface of LlOppA that undergo a significant change in proximity between the (A) open (PDB code 3DRK) and (B) closed conformation (PDB code 3DRG). Fluorescent protein insertion sites were selected in these two loops and are indicated by yellow spheres. (C) mTq2 was inserted into the N338 position of the domain III loop as a FRET donor (insertion position indicated by cyan spheres), while Venus was inserted in the opposing loop at position K177 as a FRET acceptor in addition to G54, and E116 as two other Venus insertion sites (all indicated by yellow spheres). These insertions gave a total of three FRET sensor constructs. The hinge-region is shown as magenta spheres.

Our FRET sensor design employs the LlOppA sensing domain and two fluorescent proteins inserted into positions to give a change in FRET upon binding bradykinin. FRET largely depends on distance and orientation between the donor and acceptor fluorescent proteins.[61] Thus, we compared the open and closed conformation structures of LlOppA to identify surface loops in close proximity in one conformation and significantly far apart in the other in order to get high FRET efficiency and a large dynamic range. We found two loops, each on opposing lobes of LlOppA and most distant from the hinge region that fit this criterion, where these loops go from ~19 Å apart in the closed conformation to ~35 Å apart in the open conformation (Figure 5.11). We selected a fluorescent protein insertion site in each of these loops – N338 in domain III and K177 in domain II (Figure 5.11). N338 is an insertion site we previously tested in LlOppA, but we did not test K177, though our previous results indicate that LlOppA is less tolerant to fluorescent protein insertions in domain II (Figure 5.4, Table 5.2). For this reason, we decided to include two alternative sites for K177, including a position in a nearby loop in domain II (E116) and a position in domain I (G54), which previously showed high fluorescence and expression for a single FP sensor construct (Figure 5.4, Table 5.2).

Figure 5.12 Linear diagram for our FRET-based sensor design.

A linear diagram for the LlOppA-K177-Venus-N338-mTq FRET-based sensor is shown as an example. Here, the yellow acceptor fluorescent protein, Venus (shown in yellow) was inserted at the K177 position, while the cyan donor fluorescent protein, mTq2 (shown in cyan) was inserted at the N338 position in surface loops of LlOppA (shown in orange).

Our FRET sensor variants incorporate mTq2 as the donor fluorescent protein and Venus as the acceptor (Figure 5.11, Figure 5.12). mTq2 was selected because it shows great photostability, high quantum yield (93%), pairs well with a number of FRET acceptors and we have had good success with mTq2 expression (especially in comparison to mTFP1).[29,62,63] Venus was selected because it is relatively photostable with good folding at 37°C and has good spectral overlap with the emission spectrum of mTq2.[27,64] Thus, we are screening three sensor variants – LlOppA-G54-Venus-N338-mTq2, LlOppA-E116-Venus-N338-mTq2, and LlOppA-K177-Venus-N338-mTq2. For simplicity, these sensors will be termed G54, E116 and K177, respectively.

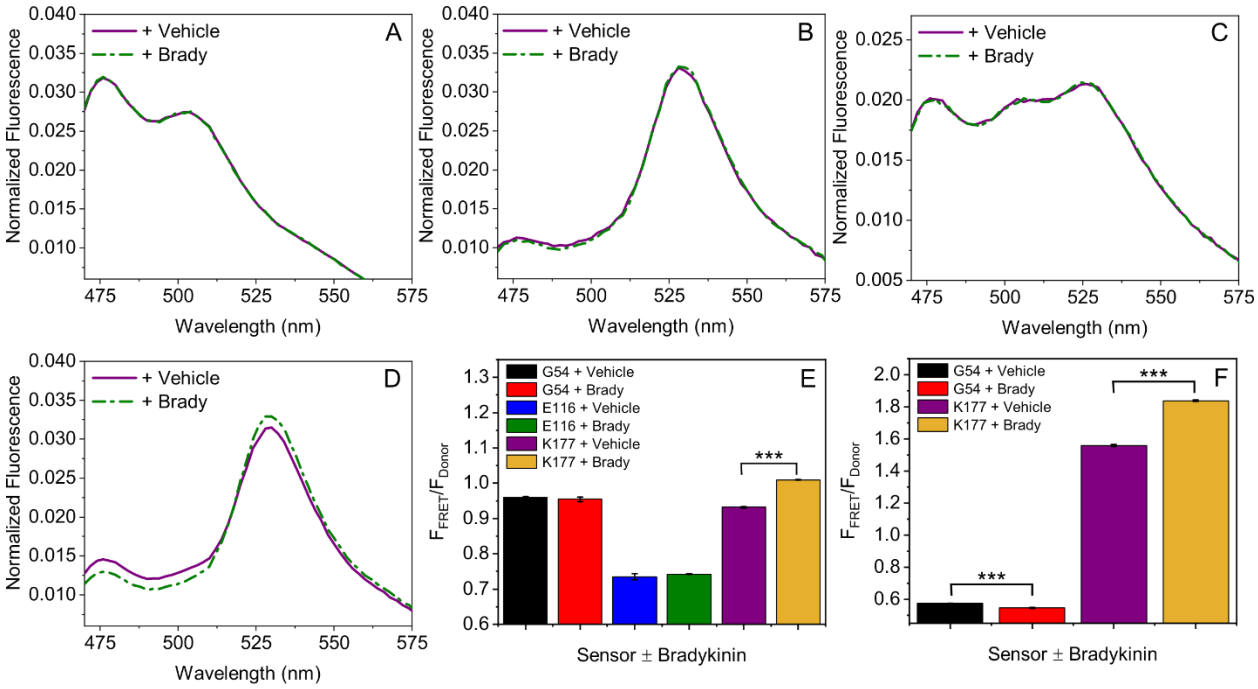

Figure 5.13 Characterization of LlOppA FRET sensor constructs at 24°C.

Emission spectra were measured for (A) mTq2 protein as a zero FRET control, and the (B) G54 (C) E116 and (D) K177 sensors. Spectra for mTq2, G54 and K177 are from purified protein, while the E116 spectra are from lysate. (E) As lysate, only the K177 sensor shows a significant change in fluorescence in the presence of vehicle vs 2.5 mM bradykinin (K177 0 mM vs 2.5 mM, p = < 0.0001), while (F) As protein, the G54 and K177 sensors show a significant change in fluorescence in the presence of vehicle vs saturating bradykinin (G54 0 mM vs 2.5 mM, p = 0.0001; K177 0 mM vs 1.5 mM, p = < 0.0001). E116 was not tested as protein. Spectra (A – D) represented as mean for n = 3 and bar graph data (E & F) represented as mean ± stdev for n = 3. Significance set at $p \leq 0.05$, *p-value ≤ 0.05, **p-value ≤ 0.001, ***p-value ≤ 0.0001.

We next screened our sensors in whole cell *E. coli* lysate for response to bradykinin by measuring fluorescence of each sensor in the presence of bradykinin and vehicle control (Figure 5.13). All sensors showed both an mTq2 emission peak at 474 nm and a Venus emission peak at 528 nm in the emission spectra for mTq2 excitation (434 nm excitation), which confirmed the expression and maturation of both fluorescent proteins (Figure 5.13). However, the G54 and K177 sensors show a weaker mTq2 emission peak, which may be an indication of poor maturation of mTq2 or higher FRET efficiency in comparison to the E116 sensor (Figure 5.13). Additionally, these results revealed that K177 is a functional sensor and shows a change in F_{FRET}/F_{Donor} with bradykinin addition (Figure 5.13 and Table 5.6). To further confirm this result, we next purified the K177 and E116 sensors and tested them for response to bradykinin addition as purified protein

(Figure 5.13, Table 5.6). We determined that the K177 sensor remained responsive to bradykinin with a further increased dynamic range of 18% vs the previous 8.3% (Table 5.6). We also determined that the G54 sensor appears to be functional, though with a small dynamic range of 4.9%. These results indicate that some functional sensors with a small dynamic range may be missed when screening in *E. coli* lysate because of attenuation of the dynamic range. This dynamic range attenuation is likely due to LlOppA nonspecifically binding to peptides in lysate, thus resulting in a population of bound and closed conformation-favoring sensor even in vehicle control conditions. However, functional sensors can still be successfully identified in lysate and further confirmed as purified protein, as exemplified by the K177 sensor, and furthermore this may be advantageous because it biases the screen towards higher dynamic range candidates. Screening in bacterial lysate should prove useful for future studies that may be performed to optimize the specificity of this sensor.

Table 5.6 Fluorescence ratios (F_{FRET}/F_{Donor}) and dynamic range of our FRET sensor constructs in lysate and as protein at 24°C and 37°C (mean ± stdev, n = 3).

Sensor Variant	Temp (°C)	Protein or Lysate	F_{Donor}/F_{FRET}	Dynamic Range
G54	24	Lysate	0.959 ± 0.003	0.5 ± 0.3
K177	24	Lysate	0.932 ± 0.002	8.3 ± 0.3
E116	24	Lysate	0.735 ± 0.008	1 ± 1
mTq2 Control	24	Protein	0.3472 ± 0.0005	0.07 ± 0.02
G54	24	Protein	0.575 ± 0.002	4.9 ± 0.5
K177	24	Protein	1.559 ± 0.007	18.0 ± 0.4
mTq2 Control	37	Protein	0.3545 ± 0.0002	0.04 ± 0.06
K177	37	Protein	1.24 ± 0.02	64 ± 0.2

To further test the K177 sensor and determine its applicability at physiological temperatures we next measured its response to bradykinin at 37°C (Table 5.6, Figure 5.14). Similar to the single fluorescent protein-based sensors (S147 and N149), the K177 sensor showed an even further increased dynamic range of 64%, while the dynamic range of the mTq2 control protein remained relatively unchanged (0.07 vs 0.04%), (Table 5.6). These data show that the K177 sensor is a functional bradykinin sensor and should prove useful at temperatures ranging from 24°C to 37°C.

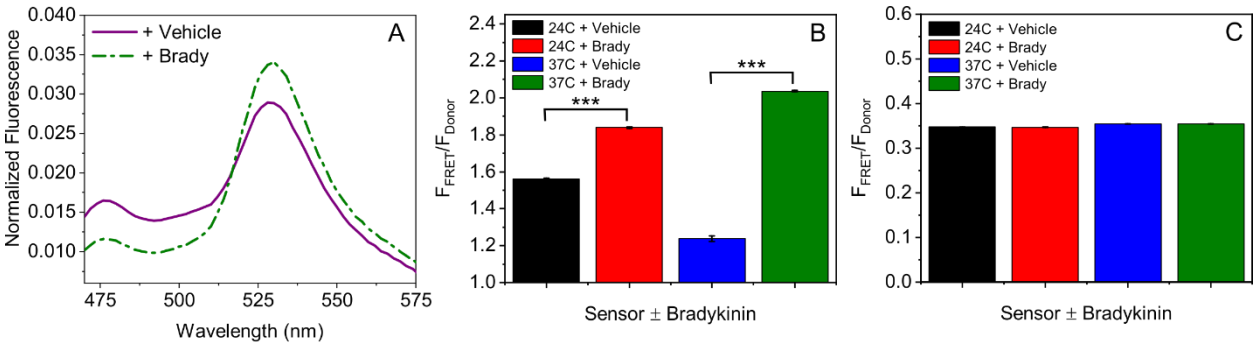

Figure 5.14 Characterization of the K177 FRET sensor construct at 37°C.

(A) Emission spectra were measured for the K177 sensor with vehicle or saturating bradykinin added at 37°C. (B) The K177 sensor shows a significant change in fluorescence in the presence of vehicle vs saturating bradykinin at 37°C (K177 0 mM vs 9.4 mM, p = < 0.0001), while the (C) mTq2 control protein does not show a significant response to bradykinin addition at 24 or 37°C.

Next, we quantitatively determined FRET efficiency of our two functional sensor constructs by measuring donor fluorescence lifetimes. Here, donor lifetime decreases with increasing FRET efficiency and FRET efficiency is calculated by comparing to the mTq2 donor in the absence of the acceptor (Venus). As shown in Table 5.7, our G54 and K177 sensors show relatively high FRET efficiencies of 25 and 29%, respectively. Additionally, the G54 sensor lifetime does not appear to significantly change with bradykinin addition (p = 0.5856), while the K177 sensor shows a significant change in lifetime (p = 0.0001), (Table 5.7). From these data we can state that while the G54 sensor shows high FRET efficiency the response to bradykinin is not robust and thus this sensor should not be considered for further use in sensing bradykinin. On the other hand, our K177 sensor shows high FRET efficiency and a robust response to bradykinin, where FRET efficiency increases as the concentration of bradykinin increases.

Table 5.7 Fluorescence lifetimes and FRET efficiency of the G54 and K177 FRET sensors (mean ± stdev, n = 3).

Sensor Variant	[Bradykinin] (mM)	Donor Lifetime (ns)	Change in Lifetime	FRET Efficiency
mTq2 Control	0	4.395 ± 0.005	N/A	N/A
mTq2 Control	2.5	4.41 ± 0.01	0.018 ± 0.007	N/A
G54	0	3.29 ± 0.02	N/A	0.251 ± 0.005
G54	2.5	3.31 ± 0.06	0.02 ± 0.06	0.249 ± 0.013
K177	0	3.126 ± 0.002	N/A	0.2887 ± 0.0004
K177	2.5	2.99 ± 0.02	-0.14 ± 0.02	0.323 ± 0.004

Lastly, we further characterized the functionality of our K177 sensor by measuring bradykinin dose response curves at 24 and 37°C. Surprisingly, the K177 sensor shows a significantly reduced affinity for bradykinin of 87 µM at 24°C (Figure 5.15, Table 5.7) in comparison to the single fluorescent protein-based sensors (Figure 5.10, Table 5.5). The affinity of the K177 sensor is even further decreased at 37°C (K_D = 2.8 mM), (Figure 5.15, Table 5.7). These results reveal the K177 is a functional FRET-based biosensor for bradykinin with an affinity in the sub-millimolar to millimolar regime.

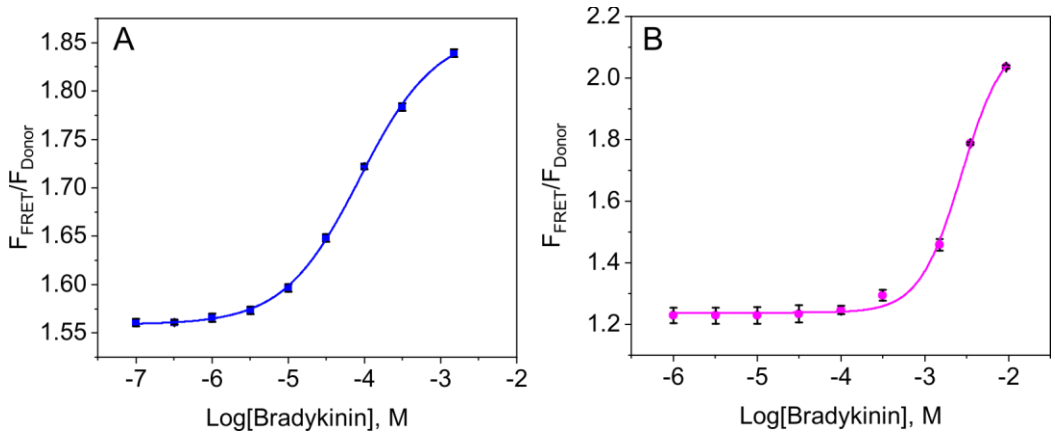

Figure 5.15 The K177 sensor measures bradykinin in a dose-dependent manner at 24°C and 37°C.

Dose response curves were measured for the N149 FRET sensor at (A) 24°C and (B) 37°C. Lines show the average fit for n = 3. Error bars are stdev.

Table 5.8 K177 sensor affinity for bradykinin peptide (RPPGFSPFR) at 24°C and 37°C (mean ± stdev, n = 3).

Sensor Variant	Temp (°C)	K_D (μM)
K177	24	87 ± 3
K177	37	2800 ± 200

Conclusion

In this work, we engineered a family of first-generation bradykinin sensors using the *Lactococcus lactis* oligopeptide-binding protein as a sensing domain. We demonstrated that functional and spectrally diverse sensors could be developed using two different sensor engineering strategies. In the first strategy, we initially inserted a cpEGFP from QUEEN2m into surface loops of LlOppA and found that LlOppA is most amenable to insertions in domain III, and insertions at position Q389 in a loop near to the hinge-region of LlOppA (I386 – S394) resulted in a sensor construct with two excitation peaks. We then found that this cpEGFP does not express well at 37°C, which led us to swap it out for three different permutation variants of the cpEGFP from iGluSnFR. These results demonstrate the importance of careful selection of the sensing domain protein in addition to the fluorescent protein variants when engineering genetically encoded sensors.

Upon testing sensor constructs with the Y145, S147 and N149 cpEGFP permutation variants inserted into the Q389 position, we found that the S147 sensor construct has a ratiometric response to bradykinin and the N149 sensor has an intensiometric response. The S147 sensor has a bradykinin affinity of 0.3 μM at 24°C and 1.6 μM at 37°C with an increased dynamic range of 25% at 37°C, while the N149 sensor has a bradykinin affinity of 1.5 μM at 24°C and 0.4 μM at 37°C with an increased dynamic range of 50% at 37°C. Thus, these sensors have spectrally distinct properties, maintain functionality at the physiologically relevant temperature of 37°C, and sense bradykinin at affinities ranging from 0.3 – 1.6 μM. The LlOppA-Q389-S147-cpEGFP ratiometric sensor is termed PepR, while the LlOppA-Q389-N149-cpEGFP intensiometric sensor is termed PepI.

In our second engineering strategy, we inserted mTq2 into a surface loop, opposite of the hinge-region in domain III at position N338, we then inserted Venus into one of three selected positions (G54, E116 or K177) to produce three FRET sensor constructs. We found that only the

LlOppA-K177-Venus-N338-mTq2 sensor construct is a functional sensor, which is in line with our predictions based on the distinct positional changes between the open and closed state crystal structures of LlOppA. This K177 sensor measures bradykinin with an affinity of 87 μM at 24°C and 2.8 mM at 37°C. This lower affinity sensor is termed PepR-FRET and has a dynamic range of 18% at 24°C and an increased dynamic range of 64% at 37°C with relatively high basal FRET efficiency of 29%.

In summary, this work demonstrates the feasibility of engineering genetically encoded peptide sensors from an oligopeptide-binding protein. We successfully engineered a set of diverse sensors with distinct spectral properties and affinities for bradykinin, including an intensiometric single fluorescent protein-based sensor (PepI), ratiometric single fluorescent protein-based sensor (PepR) and a low affinity ratiometric FRET-based sensor (PepR-FRET). These sensors should prove useful for dissecting bradykinin signaling with high spatial and temporal resolution and should help to further our understanding of the involvement of bradykinin in inflammation, neuroinflammation, and associated disorders. Additionally, this work may help inform on the generation of other peptide sensors, such as sensors for the neuropeptide dynorphin-A, which LlOppA has been shown to bind.[30] Future studies should focus on mutating the binding cleft of LlOppA to further increase specificity of these sensors for bradykinin or other peptides of interest. Given the significant structural homology of these oligopeptide-binding proteins, the fluorescent protein insertion sites reported here may prove fruitful for developing peptide sensors using other oligopeptide-binding proteins, such as BsAppA. It is our hope that this work and our new family of genetically encoded peptide sensors (PepI, PepR, PepR-FRET) open the door for development of many more peptide sensors, ranging in ligand specificity, affinity and spectral properties.

5.5 References

1. Leeb-lundberg, F., Marceau, F., Pettibone, D. J. & Zuraw, B. L. International Union of Pharmacology. XLV. Classification of the Kinin Receptor Family: from Molecular Mechanisms to Pathophysiological Consequences. *Mol. Pharmacol.* **57,** 27–77 (2005).

2. Yarovaya, G. A. & Neshkova, A. E. Past and Present Research on the Kallikrein Kinin System (On the 90th Anniversary of the Discovery of the System). *Russ. J. Bioorganic Chem.* **41,** 245–259 (2015).

3. Hess, J. F. *et al.* Differential pharmacology of cloned human and mouse B2 bradykinin receptors. *Mol. Pharmacol.* **45,** 1–8 (1994).

4. Enquist, J., Skröder, C., Whistler, J. L. & Leeb-Lundberg, L. M. F. Kinins Promote B2 Receptor Endocytosis and Delay Constitutive B1 Receptor Endocytosis. *Mol. Pharmacol.* **71,** 494–507 (2007).

5. Guevara-Lora, I. Kinin-mediated inflammation in neurodegenerative disorders. *Neurochem. Int.* **61,** 72–78 (2012).

6. Marceau, F. & Regoli, D. Bradykinin receptor ligands: Therapeutic perspectives. *Nat. Rev. Drug Discov.* **3,** 845–852 (2004).

7. Raidoo, D. M. & Bhoola, K. D. Kinin receptors on human neurones. *J. Neuroimmunol.* **77,** 39–44 (1997).

8. Raidoo, D. M. *et al.* Visualization of bradykinin B2 receptors on human brain neurons. *Immunopharmacology* **33,** 104–107 (1996).

9. Gimpl, G., Walz, W., Ohlemeyer, C. & Kettenmann, H. Bradykinin receptors in cultured astrocytes from neonatal rat brain are linked to physiological responses. *Neurosci. Lett.* **144,** 139–142 (1992).

10. Raidoo, D. M. & Bhoola, K. D. Pathophysiology of the kallikrein-kinin system in mammalian nervous tissue. *Pharmacol. Ther.* **79,** 105–127 (1998).

11. Noda, M. *et al.* Expression and function of bradykinin receptors in microglia. *Life Sci.* **72,** 1573–1581 (2003).

12. Noda, M. *et al.* Kinin receptors in cultured rat microglia. *Neurochem. Int.* **45,** 437–442 (2004).

13. Stephens, G. J., Cholewinski, A. J., Wilkin, G. P. & Djamgoz, M. B. A. Calcium-mobilizing and electrophysiological effects of bradykinin on cortical astrocyte subtypes in culture. *Glia* **9,** 269–279 (1993).

14. parpura, V; Basarsky, T. A.; Liu, F.; Jeftinija, K.; Jeftinija, S.; Haydon, P. G. Glutamate-mediated astrocyte-neuron signalling. *Nature* **369,** 744–747 (1994).

15. Rydh-Rinder, M., Kerekes, N., Svensson, M. & Hökfelt, T. Glutamate release from adult primary sensory neurons in culture is modulated by growth factors. *Regul. Pept.* **102,** 69–79 (2001).

16. Liu, H. T., Akita, T., Shimizu, T., Sabirov, R. Z. & Okada, Y. Bradykinin-induced astrocyte-neuron signalling: Glutamate release is mediated by ROS-activated volume-sensitive outwardly rectifying anion channels. *J. Physiol.* **587,** 2197–2209 (2009).

17. Wahl, M. *et al.* Vasomotor and permeability effects of bradykinin in the cerebral microcirculation. *Immunopharmacology* **33,** 257–263 (1996).

18. Sarker, M. H., Hu, D. E. & Fraser, P. A. Acute effects of bradykinin on cerebral microvascular permeability in the anaesthetized rat. *J. Physiol.* **528,** 177–187 (2000).

19. Su, J. *et al.* Blockade of bradykinin B2 receptor more effectively reduces postischemic blood–brain barrier disruption and cytokines release than B1 receptor inhibition. *Biochem. Biophys. Res. Commun.* **388,** 205–211 (2009).

20. Bhoola, K. D. & Overview, I. Bioregulation of Kinins: kallikreins, kininogens, and kininases. *Phamacological Rev.* **44,** 1–80 (1992).

21. Greenwald, E. C., Mehta, S. & Zhang, J. Genetically Encoded Fluorescent Biosensors Illuminate the Spatiotemporal Regulation of Signaling Networks. *Chem. Rev.* **118,** acs.chemrev.8b00333 (2018).

22. Marvin, J. S. *et al.* Stability , affinity , and chromatic variants of the glutamate sensor iGluSnFR. *Nat. Methods* **15,** (2018).

23. Sun, F. *et al.* A Genetically Encoded Fluorescent Sensor Enables Rapid and Specific Detection of Dopamine in Flies, Fish, and Mice. *Cell* **174,** 481–496.e19 (2018).

24. Petersen, T. N., Brunak, S., von Heijne, G. & Nielsen, H. SignalP 4.0: discriminating signal peptides from transmembrane regions. *Nat. Methods* **8,** 785–786 (2011).

25. Yaginuma, H. *et al.* Diversity in ATP concentrations in a single bacterial cell population revealed by quantitative single-cell imaging. *Sci Rep* **4,** 6522 (2014).

26. Marvin, J. S. *et al.* An optimized fluorescent probe for visualizing glutamate neurotransmission. *Nat. Methods* **10,** (2013).

27. Rekas, A., Alattia, J. R., Nagai, T., Miyawaki, A. & Ikura, M. Crystal structure of venus, a yellow fluorescent protein with improved maturation and reduced environmental sensitivity. *J. Biol. Chem.* **277,** 50573–50578 (2002).

28. Tsien, R. Y. The green fluorescent protein. *Annu. Rev. Biochem.* **67,** 509–544 (1998).

29. Goedhart, J. *et al.* Structure-guided evolution of cyan fluorescent proteins towards a quantum yield of 93%. *Nat. Commun.* **3,** (2012).

30. Norcross, S., Sunderraj, A., Tantama, M. pH- and Temperature-Dependent Peptide Binding to the *Lactococcus lactis* Oligopeptide-Binding Protein A Measured with a Fluorescence Anisotropy Assay. *ACS Omega* **4,** 2812–2822 (2019).

31. Kelly, S. M., Jess, T. J. & Price, N. C. How to study proteins by circular dichroism. *Biochim. Biophys. Acta - Proteins Proteomics* **1751,** 119–139 (2005).

32. Lanfermeijer, F. C., Picon, A., Konings, W. N. & Poolman, B. Kinetics and consequences of binding of nona- and dodecapeptides to the oligopeptide binding protein (OppA) of Lactococcus lactis. *Biochemistry* **38,** 14440–14450 (1999).

33. Detmers, F. J. M., Kunji, E. R. S., Lanfermeijer, F. C., Poolman, B. & Konings, W. N. Kinetics and specificity of peptide uptake by the oligopeptide transport system of Lactococcus lactis. *Biochemistry* **37,** 16671–16679 (1998).

34. Kunji, E. R. S. *et al.* Reconstruction of the proteolytic pathway for use of β-casein by Lactococcus lactis. *Mol. Microbiol.* **27,** 1107–1118 (1998).

35. Juillard, V., Guillot, A., Le Bars, D. & Gripon, J. C. Specificity of milk peptide utilization by Lactococcus lactis. *Appl. Environ. Microbiol.* **64,** 1230–1236 (1998).

36. Lanfermeijer, F. C., Detmers, F. J. M., Konings, W. N. & Poolman, B. On the binding mechanism of the peptide receptor of the oligopeptide transport system of Lactococcus lactis. *EMBO J.* **19,** 3649–3656 (2000).

37. Detmers, F. J. M. *et al.* Combinatorial peptide libraries reveal the ligand-binding mechanism of the oligopeptide receptor OppA of Lactococcus lactis. *Proc. Natl. Acad. Sci.* **97,** 12487–12492 (2000).

38. Charbonnel, P. *et al.* Diversity of oligopeptide transport specificity in Lactococcus lactis species: A tool to unravel the role of OppA in uptake specificity. *J. Biol. Chem.* **278,** 14832–14840 (2003).

39. Doeven, M. K., Abele, R., Tampé, R. & Poolman, B. The binding specificity of OppA determines the selectivity of the oligopeptide ATP-binding cassette transporter. *J. Biol. Chem.* **279,** 32301–32307 (2004).

40. Berntsson, R. P. A. *et al.* The structural basis for peptide selection by the transport receptor OppA. *EMBO J.* **28,** 1332–1340 (2009).

41. Berntsson, R. P.-A., Thunnissen, A.-M. M. W. H., Poolman, B. & Slotboom, D. J. Importance of a hydrophobic pocket for peptide binding in Lactococcal OppA. *J. Bacteriol.* **193,** 4254–4256 (2011).

42. Picon, A. & Van Wely, K. H. M. Peptide Binding to the Bacillus subtilis Oligopeptide-Binding Proteins OppA and AppA. *Mol. Biol. Today* **2,** 21–25 (2001).

43. Levdikov, V. M. *et al.* The structure of the oligopeptide-binding protein, AppA, from Bacillus subtilis in complex with a nonapeptide. *J. Mol. Biol.* **345,** 879–892 (2005).

44. Lorenzana, L. M., Pérez-Redondo, R., Santamarta, I., Martín, J. F. & Liras, P. Two oligopeptide-permease-encoding genes in the clavulanic acid cluster of Streptomyces clavuligerus are essential for production of the β-lactamase inhibitor. *J. Bacteriol.* **186,** 3431–3438 (2004).

45. Mackenzie, A. K. *et al.* Crystal structures of an oligopeptide-binding protein from the biosynthetic pathway of the Beta-lactamase inhibitor clavulanic acid. *J. Mol. Biol.* **396,** 332–344 (2010).

46. Yoon, H. J., Kim, H. J., Mikami, B., Yu, Y. G. & Lee, H. H. Crystal structure of a putative oligopeptide-binding periplasmic protein from a hyperthermophile. *Extremophiles* **20,** 723–731 (2016).

47. Berntsson, R. P.-A., Smits, S. H. J., Schmitt, L., Slotboom, D. J. & Poolman, B. A structural classification of substrate-binding proteins. *FEBS Letters* **584,** 2606–2617 (2010).

48. Mao, Boryeu; Pear, Michael R.; McCammon, J. Andrew; Quicho, F. A. Hinge-bending in L-Arabinose- binding Protein. *J. Biol. Chem.* **257,** 1131–1133 (1981).

49. Gouridis, G. *et al.* Conformational dynamics in substrate-binding domains influences transport in the ABC importer GlnPQ. *Nat. Publ. Gr.* **22,** 57–64 (2014).

50. Fehr, M., Frommer, W. B. & Lalonde, S. Visualization of maltose uptake in living yeast cells by fluorescent nanosensors. *PNAS* **99,** 9846–9851 (2002).

51. Marvin, J. S., Schreiter, E. R. & Echevarrı, I. M. A genetically encoded, high-signal-to-noise maltose sensor. *Proteins Struct. Funct. Bioinforma.* 3025–3036 (2011). doi:10.1002/prot.23118

52. Hu, H. *et al.* A genetically encoded toolkit for tracking live-cell histidine dynamics in space and time. *Nat. Publ. Gr.* 1–9 (2017). doi:10.1038/srep43479

53. Harvey, R. J. Damage to Streptococcus lactis resulting from growth at low pH. *J. Bacteriol.* **90,** 1330–1336 (1965).

54. Bibal, B., Goma, G., Vayssier, Y. & Pareilleux, A. Influence of pH, lactose and lactic acid on the growth of Streptococcus cremoris: a kinetic study. *Appl. Environ. Microbiol.* **28,** 340–344 (1988).

55. Baird, G. S., Zacharias, D. A. & Tsien, R. Y. Circular permutation and receptor insertion within green fluorescent proteins. *Proc. Natl. Acad. Sci. U. S. A.* **96,** 11241–11246 (1999).

56. Nakai, J., Ohkura, M. & Imoto, K. A high signal-to-noise Ca(2+) probe composed of a single green fluorescent protein. *Nat. Biotechnol.* **19,** 137–41 (2001).

57. Tallini, Y. N. *et al.* Imaging cellular signals in the heart in vivo: Cardiac expression of the high-signal Ca2+ indicator GCaMP2. *Proc. Natl. Acad. Sci.* **103,** 4753–4758 (2006).

58. Zacharias, D. A., Violin, J. D., Newton, A. C. & Tsien, R. Y. Partitioning of lipid-modified monomeric GFPs into membrane microdomains of live cells. *Science* **296,** 913–6 (2002).

59. Siemering, K. R., Golbik, R., Sever, R. & Haseloff, J. Mutations that suppress the thermosensitivity of green fluorescent protein. *Curr. Biol.* **6,** 1653–1663 (1996).

60. Akerboom, J. *et al.* Optimization of a GCaMP Calcium Indicator for Neural Activity Imaging. *J. Neurosci.* **32,** 13819–13840 (2012).

61. Pietraszewska-Bogiel, A. & Gadella, T. W. J. FRET microscopy: From principle to routine technology in cell biology. *J. Microsc.* **241,** 111–118 (2011).

62. Cranfill, Paula J.; Sell, Brittney R.; Baird, Michelle A.; Allen, John R.; Lavagnino, Zeno; de Gruiter, H Martijn; Kremers, Gert-Jan; Davidson, Michael W.; Ustione, Alessandro; Piston, D. W. Quantitative assessment of fluorescent proteins. *Nat. Methods* **13,** 557–563 (2016).

63. Mastop, M. *et al.* Characterization of a spectrally diverse set of fluorescent proteins as FRET acceptors for mTurquoise2. *Sci. Rep.* **7,** 1–18 (2017).

64. Bajar, B., Wang, E., Zhang, S., Lin, M. & Chu, J. A Guide to Fluorescent Protein FRET Pairs. *Sensors* **16,** 1488 (2016).